

Nanoparticle shape, thermodynamics and kinetics

This content has been downloaded from IOPscience. Please scroll down to see the full text.

2016 J. Phys.: Condens. Matter 28 053001

(<http://iopscience.iop.org/0953-8984/28/5/053001>)

View [the table of contents for this issue](#), or go to the [journal homepage](#) for more

Download details:

IP Address: 129.105.122.139

This content was downloaded on 28/06/2016 at 21:45

Please note that [terms and conditions apply](#).

Topical Review

Nanoparticle shape, thermodynamics and kinetics

L D Marks and L Peng

Department of Materials Science and Engineering, Northwestern University, Evanston, IL 60208, USA

E-mail: l-marks@northwestern.edu

Received 19 October 2015, revised 9 December 2015

Accepted for publication 15 December 2015

Published 20 January 2016



Abstract

Nanoparticles can be beautiful, as in stained glass windows, or they can be ugly as in wear and corrosion debris from implants. We estimate that there will be about 70 000 papers in 2015 with nanoparticles as a keyword, but only one in thirteen uses the nanoparticle shape as an additional keyword and research focus, and only one in two hundred has thermodynamics. Methods for synthesizing nanoparticles have exploded over the last decade, but our understanding of how and why they take their forms has not progressed as fast. This topical review attempts to take a critical snapshot of the current understanding, focusing more on methods to predict than a purely synthetic or descriptive approach. We look at models and themes which are largely independent of the exact synthetic method whether it is deposition, gas-phase condensation, solution based or hydrothermal synthesis. Elements are old dating back to the beginning of the 20th century—some of the pioneering models developed then are still relevant today. Others are newer, a merging of older concepts such as kinetic-Wulff constructions with methods to understand minimum energy shapes for particles with twins. Overall we find that while there are still many unknowns, the broad framework of understanding and predicting the structure of nanoparticles via diverse Wulff constructions, either thermodynamic, local minima or kinetic has been exceedingly successful. However, the field is still developing and there remain many unknowns and new avenues for research, a few of these being suggested towards the end of the review.

Keywords: nanoparticles, thermodynamics, electron microscopy, shape, kinetics, Wulff construction

(Some figures may appear in colour only in the online journal)

1. Introduction

Small is beautiful. The stained glass windows in medieval churches with different nanoparticles for different colors have awed worshippers for centuries.

Small is ugly. Nanoparticulate debris from wear and corrosion of implants can lead to severe illness and pain, and is one of the most important unsolved health issues of the 21st century.

Nanoparticles are everywhere. They play a critical role in modern society in areas as diverse of heterogeneous catalysis

to produce chemicals to controlling the properties of advanced metals used in the aerospace industry. Sometimes their size, shape and structure is exceedingly well controlled, sometimes it is the luck of the draw. They will continue to play a critical role into the future, and there are large efforts around the world to exploit them for numerous applications from controlled drug delivery in nanomedicine to controlling light for information in nanoplasmonics.

However, there is an issue. To quote from William Whewell [1] *It is a test of true theories not only to account for but to predict phenomena.*

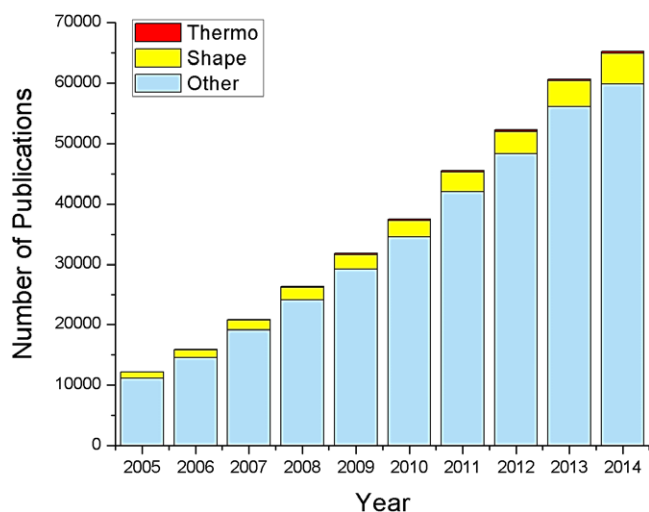


Figure 1. Publications per year which contain only ‘nanoparticles’ as a keyword (blue), also have ‘shape’ (yellow) or ‘thermodynamics’ (red). One in thirteen have shape, one in two hundred thermodynamics.

Methods of producing nanoparticles have far outstripped our ability to predict how they are generated and their shape and structure. As shown in figure 1, the number of scientific papers with ‘nanoparticle’ as a keyword is increasing approximately linearly with time and we predict that there will be more than 70 000 in 2015. In the existing literature, only about one in thirteen includes ‘shape’ as a keyword, and one in two hundred ‘thermodynamics’. The term ‘nanoparticle synthesis’ has become common, implying that nanoparticles are produced with the same degree of control as in industrial production of chemicals. Unfortunately one rarely has this amount of control. While sometimes it does not matter exactly what the nanoparticles are, in an ideal world we want to have ‘six sigma control’, i.e. control the shape so that only 3.4 per million nanoparticles are not the target. This is an industrial and engineering standard, but we are current far from achieving this level of control.

Given the size of the literature a complete review is not possible, rather the intent is to overview where we are in terms of being able to predict the nanoparticle shape by understanding the thermodynamic and kinetic driving forces independent of whether they are produced by evaporation onto substrates, gas-phase condensation, solution synthesis or hydrothermal methods. Some other reviews discussing different aspects can be found in [2–32]. It is important to recognize that the question of thermodynamic versus kinetic control of shapes has been a source of almost endless confusion in the literature. For instance, the seminal paper by Wulff [33] is often cited as the origin of the thermodynamic Wulff construction, but the actual title is ‘*On the question of speed of growth and dissolution of crystal surfaces*’, with most of the analysis based upon growth experiments, i.e. kinetic control of the shape, although Wulff assumed a direct relationship between the surface energy and growth rate (which is not necessarily correct).

In many cases nanoparticles are simple, single crystals with well-defined faces and simple platonic shapes such as octahedra or cubes. A different class of nanoparticles is ones

which are have more complex shapes and internal structure. The most common ones contain twins, either parallel in ‘lamellar twinned particles’ (LTPs) or either five or twenty different single crystal units separated by twin boundaries, and are called ‘Multiply-Twinned Particles’ or MTPs. As discussed by Hofmeister [15, 34], there are reports of MTPs in the 19th Century, what were called ‘fivelings’, and a number of reports in the 50’s and 60’s of five-fold particles in whiskers (e.g. [35–38]). The first definitive work was performed by Ino and Ogawa [39–41]. By using relatively primitive (by current standards) electron microscopes, they were able to piece together the two main types of MTPs, the icosahedral (Ic) as well as the decahedral (Dh) MTPs. We will use herein these abbreviations for these particles which have become common in the literature, and correlate to the point group symmetries Ic and D_{5h} respectively [42]. Almost immediately the structure of these particles was confirmed essentially independently by Allpress and Sanders [43]. In the early work MTPs were described as assemblies of tetrahedral subunits with an angular gap equivalent to one or more Volterra disclinations [44], elastically strained by ~2% for the Dh and ~6% for the Ic to form space-filling structures. This interpretation of elastic strain was confirmed at the atomic scale first using lattice imaging [45] then later by atomic resolution imaging [46, 47]. For completeness, there are many more complicated shapes such as what were called ‘polyparticles’ [47] which are either polyicosahedral structures similar to those first analyzed by Hoare and Pal [48], or due to incomplete coalescence.

The focus of this review is the fundamentals that control the shape of nanoparticles, with a little more attention paid to the more complicated case of these multiply twinned particles; the better we understand complex nanoparticle, the better we understand everything. A schematic illustrating many of the shapes of interest is given in figure 2, split into cases where thermodynamic control determines the final shape and those where kinetics control. Several shapes appear on both sides, both single crystals as well as multiply-twinned particles. Every structure that is thermodynamically stable can also occur under kinetic control, but the converse is not true. Several structures appear in different locations to where they are often placed in the literature, for instance the pentagonal biprism five-fold particles which is often incorrectly described as a thermodynamic shape.

Parts of this review depend upon older work dating back to the first half of the 20th century, where much of the formative science was established. Some issues were first brought up then, and remain unsolved to this day—for instance what happens when nanoparticles are too small to have the high index faces which are present on mesoscale particles. A fair amount of the review describes work which was done in the second half of the 20th century when transmission electron microscopy reached resolutions where it could start to reveal details on the atomic structure. Much of the early work on MTPs has been reviewed [2] with earlier work on more diverse nanoparticles of almost every elemental solid and several compounds (called at that time ‘small particles’ or ‘ultrafine particles’) available in the inert gas evaporation

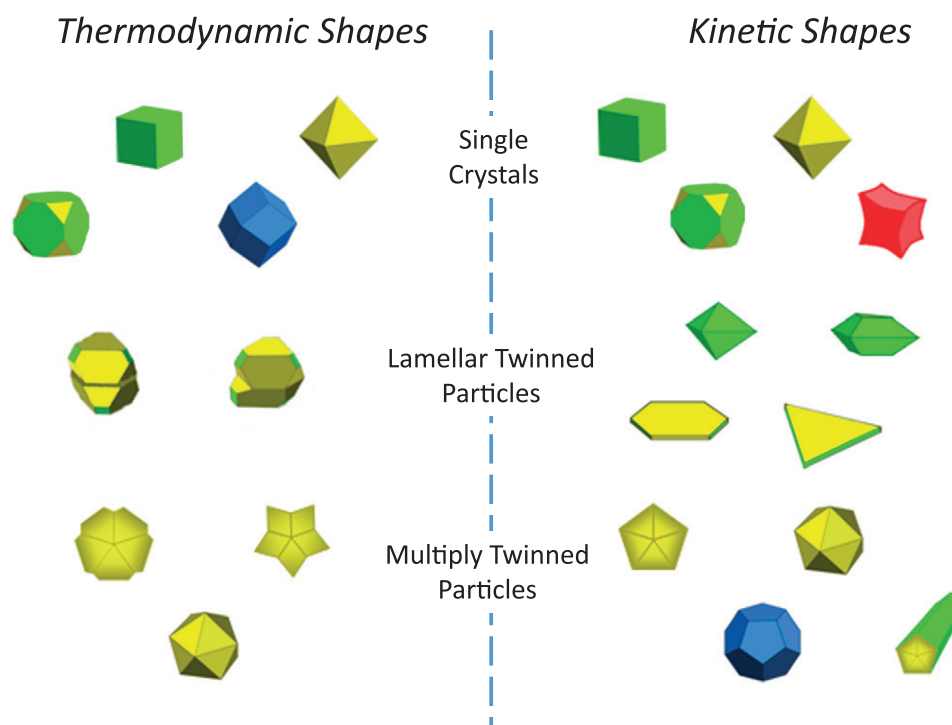


Figure 2. Some of the shapes discussed in the paper split into ones which can occur from thermodynamic control and ones which are only from kinetic control, split into the three broad categories of Single Crystals, Lamellar Twinned particles and Multiply Twinned Particles. Every thermodynamic shape can also arise from kinetics, but the converse is not true. The facets are color coded, yellow for $\{111\}$, green for $\{100\}$ blue for $\{110\}$ and red for higher index.

literature [49–55] as well as earlier structural studies on colloidal growth [56, 57].

Of the more recent literature only parts can be included, some of the recent progress in kinetic models as well as tests of the older models using new experimental methods. The field is progressing rapidly, and with new instrumentation, particularly higher precision transmission electron microscopes, new details are being unraveled almost daily. Modeling advances have accompanied experimental progress, for example better elasticity models and atomistic methods.

The structure of this review is as follows. First, some aspects of the thermodynamic fundamentals are described, particularly how one transitions from an atomistic approach to a continuum one, since this contains some subtle traps for the unwary. This is followed by a description of the large family of thermodynamic Wulff construction shapes for both supported and unsupported nanoparticles, as well as other variants such as when there is another degree of freedom in alloys at the nanoscale (nanoalloys). We then turn from thermodynamic control to the kinetic Wulff constructions with the addition of enhancement terms for growth at twin boundaries. In a few cases some logical extensions of the existing literature will be described, for instance the Wulff shape with a fixed excess of some species and the possibility of concave kinetic shapes via a second class of kinetic Wulff solutions as an alternative to the Berg effect. We next discuss some of the extended possibilities of kinetic shapes including why corners should be round and also symmetry breaking. We then discuss strain in MTPs for which there is extensive evidence and good qualitative agreement between stress relaxation mechanisms from theory and experimental data. Finally we turn to a brief

discussion of the thermodynamic energy balance of MTPs versus size, pointing out the important ambiguities due to the role of chemisorbants in changing the surface stress, and provide a brief analysis of how structures of nanoparticle populations may evolve during growth, either *Survival of the Fittest*; *Survival of the Fastest* or *Survival of a Population*. In a short discussion some future possibilities are described as well as some of the unanswered questions.

In a number of cases scientific urban myths about nanoparticles will be pointed out, hopefully tactfully. Just like society as a whole, scientific myths can develop about what is true and what is not based upon misunderstandings (e.g. [58], for an informative analysis). This area has a number of these myths, the most obvious being that perfect decahedral particles with only $\{111\}$ facets as well as single crystal tetrahedra are thermodynamically stable.

2. Thermodynamic fundamentals

Fundamental to understanding nanoparticles is the energy as a function of size, shape, stress and the external environment. This is not completely simple, and there are a number of ways to construct this. What is most important is to pay attention to what reference states are used and follow a specific set of conventions—different references yield wildly different results for some of the key parameters, particularly the surface stress tensor.

In a purely atomistic description, the total energy of an ordered, crystalline nanoparticle can be written as the infinite series:

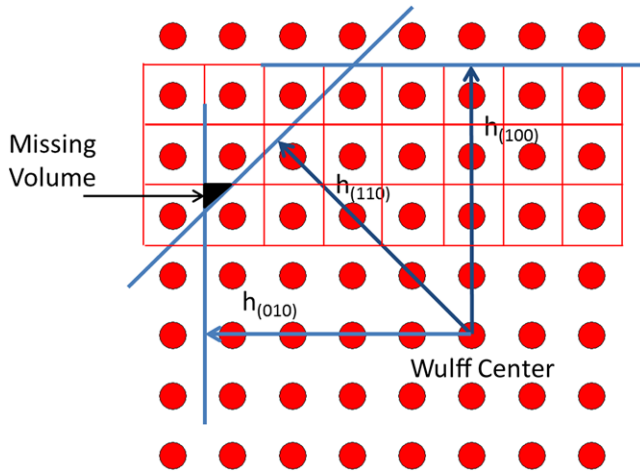


Figure 3. Illustration of the equimolar cut for surfaces in terms of the Wigner-Seitz unit cells. There may be a small discrepancy in the total volume as indication, but this can generally be neglected.

$$E = \sum_{i,j,k} a_{ijk} n_i n_j n_k + \sum_{i,j} b_{ij} n_i n_j + \sum_i c_i n_i + d + \sum_i e_i / n_i + \sum_{ij} f_{ij} / n_i n_j \dots \quad (1)$$

where the n_i are positive integers indicating the number of atoms along particular directions. To converge for an infinitely large crystal the series cannot contain any terms higher than third-order in n_i , and inverse powers may be needed to achieve the proper limits for a single atom.

Assuming convex shapes for all single crystal regions and replacing equation (1) with a vector of normal distances for each face from a common origin $\underline{h} = (h_1, h_2 \dots h_k)$ for k facets, with all h_i real but not necessarily positive numbers leads to:

$$E = \sum_{i,j,k} A_{ijk} h_i h_j h_k + \sum_{i,j} B_{ij} h_i h_j + \sum_i C_i h_i + D + \sum_j F_j / h_j \dots \quad (2)$$

As illustrated in figure 3 each h_i is a combination of a geometric distance from the origin to the outermost plane of atoms plus a ‘Gibbs distance’ outside the surface, the latter being needed to properly achieve the transition from atomistic to continuum models [59, 60]. This is the Gibbs equimolar partition for the surface. For a bulk surface the relevant distance is half that to the first atomic plane removed to create the surface, effectively using a Wigner-Seitz unit cell around each atom or basis of atoms in the unit cell. For very large sizes the first term on the right is then proportional to the volume and the number of atoms. When the size of the cluster is relatively small there will in general be a non-linear relationship between the h_i and the number of atoms along specific directions as discussed by Hamilton [60], shown in figure 4, a plot of the difference between the total energy and multiple of the number of atoms and the cohesive energy, as well as the effective edge energy term, with s the edge length of a cuboctahedron, d the interatomic spacing and n the number

of atoms. With the equimolar definition ($s = (n - 0.5)d$) the effective edge energy terms are small, whereas with other definitions they are rather large. With an appropriate non-linear relationship the edge energy terms will be very small and can be safely ignored.

The continuum shape is then defined by the set of planes normal to all h_i , and all continuum quantities are defined via the appropriate partial derivatives or integrals taking care to include non-linearity. For instance, the ‘Gibbs Volume’ (V_G) would be the volume within this shape, whereas the ‘Gibbs Surface Area’ (A_G) would be the external area, both in conventional units.

With this formulation energy terms $O(h^3)$ are the bulk cohesive energy and strain energy terms, those of $O(h^2)$, the total surface free energy and surface stress terms, those of $O(h)$, edge terms as well as counting corrections, and those of $O(h^0)$, corner as well as additional counting corrections (e.g. to ensure the correct limit for a single atom). As a general guide the relative importance of the different terms when comparing nanoparticles with the same number of atoms is:

Δ surface energy $\approx \Delta$ strain energy $> \Delta$ surface stress energy $> \Delta$ twin boundary energy $\approx \Delta$ lattice parameter $\approx \Delta$ counting corrections

To convert to a continuum model we switch to the volume V_G (proportional to the number of atoms due to the definition) as the descriptor, i.e. write

$$\sum_{i,j,k} A_{ijk} h_i h_j h_k = V_G \left(\frac{\mu^B}{\nu_0} + W_D \right) \quad (3)$$

where μ^B is the bulk chemical potential per atom in the absence of any strain, ν_0 the volume per atom and W_D the strain energy density. In principle the total strain energy of the nanoparticle can be size dependent. While energy models excluding the strain energy have been suggested [61, 62], these go to a physically incorrect limit at large sizes and are therefore necessarily incorrect. Additional terms can be added for pressure contributions, but these are small and cancel when different structures are compared. Including the temperature dependence will include entropy contributions, which can be important particularly for multicomponent nanoparticles as discussed later.

In a similar fashion the second term on the right of equation (2) can be written as

$$\sum_{i,j} B_{ij} h_i h_j = V^{\frac{2}{3}} (\gamma_{111} \epsilon_W + \langle g_{ij} e_{ij} \rangle \epsilon_g) \quad (4)$$

which contains the surface free energy (γ) per unit area as well as that of any twin boundaries in $V^{\frac{2}{3}} \gamma_{111} \epsilon_W$ and the coupling of strains and the surface free energy in $V^{\frac{2}{3}} \langle g_{ij} e_{ij} \rangle \epsilon_g$ [63–65] where g_{ij} is the surface stress tensor and e_{ij} strains which will be discussed a little later in equations (7) and (8). The constant ϵ_W is definable as

$$\epsilon_W = \left(\frac{1}{\gamma_{111}} \right) \int \gamma dS / V^{2/3} \quad (5)$$

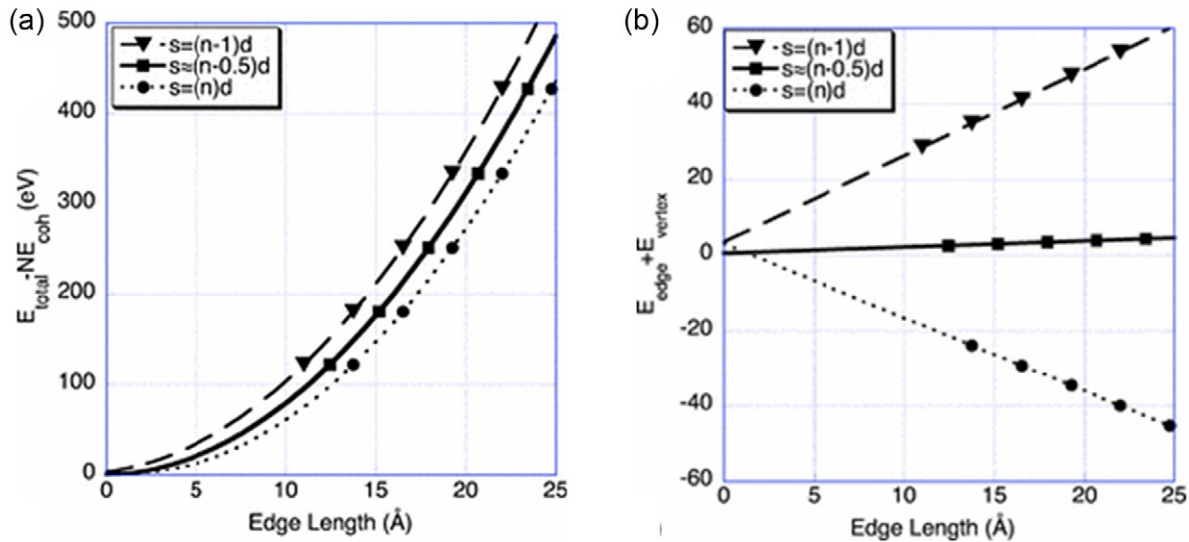


Figure 4. Example of the importance of the equimolar surface partition. In (a) the difference in the total energy and the number of atoms multiplied by the cohesive energy is plotted with three different definitions of the length. In (b) the effective edge and vertex energy is similarly plotted. With the Gibbs definition they are both small, but not with the others. Reproduced with permission from [60]. Copyright 2006 The American Physical Society.

and is a size independent constant which only depends upon the external surface of the nanoparticle and (weakly) upon the twin boundaries as discussed later.

To obtain the total energy, the volume and surface terms (equations (3) and (4)) are substituted into equation (2):

$$E = V \left(\frac{\mu^B}{v_0} + W_D \right) + V^{2/3} (\gamma_{111} \varepsilon_W + \langle g_{ij} e_{ij} \rangle \varepsilon_g) + O(h) \quad (6)$$

where the rightmost term includes any remaining corrections due to counting effects as well as edge and corner energies, and the inverse terms in equations (1) and (2) have been ignored. For very small clusters (for instance less than 2 nm) these may be important; otherwise they can be neglected if the correct equimolar partition is used.

How a full conversion to a classical formulation where the *final volume and area* (not the initial Gibbsian values) would be performed is worth indicating. The Gibbs volume and surface area are proportional to the number of atoms involved in each at some reference condition for which a natural definition is standard temperature and pressure (STP) and no strain. The classical volume and surface area are referenced to the *final* state of the nanoparticle, and as such vary with temperature, pressure and strain, and are not proportional to the number of atoms.

This distinction is important when it comes to how to describe the surface free energy in the presence of strain. Most liquids cannot be strained, so there is only one energy term of importance, typically called the surface tension. However, solids can be strained so there are two terms, the free energy per surface unit and the change in the total energy of the surface with strain. Because there are two terms, it is preferable to avoid use of the term ‘surface tension’ for solids. The question is what ‘unit’ to use, an atomistic Gibbsian unit dependent upon the number of atoms in the surface, or the classical one based upon the surface area. If we write everything referenced

to the free energy E_S of a flat surface per surface atom (N_S) or the Gibbsian area A_G , we can define the total energy, surface free energy γ , and the surface stress tensor as g_{ij} .

$$E_S = A_G \gamma ; \gamma = \partial E_S / \partial A_G ; g_{ij} = \partial \gamma / \partial e_{ij}. \quad (7)$$

with the surface free energy proportional to the surface chemical potential per atom, the surface stress the change with respect to some strain component e_{ij} . The alternative approach is to define the energy of the flat surface referenced to its final area A , where the later changes with the strain, in which case

$$E_S = A \gamma ; \gamma = \partial E_S / \partial A ; g_{ij} = \gamma \delta_{ij} + \partial \gamma / \partial e_{ij}. \quad (8)$$

since the final area changes with strain, with δ_{ij} the Kronecker delta function. The two are different, and the sign and magnitude of the surface stress tensor depends upon the definition used. This second definition is problematic for analyses of the elastic strain contributions, since this is normally considered in terms of a nominal strain-free volume. We find the first, atomistic or Gibbsian definition more convenient when dealing with nanoparticles since it is also consistent with how the volume was defined earlier, and it will be used throughout this review.

To complicate some of the issues slightly further, even in the classical limit there is an issue with the meaning of surface area, size and volume of a nanoparticle. In many cases these are measured experimentally by some technique, and the value is dependent upon the technique used. As illustrated in figure 5 most scattering experiments such as x-ray diffraction and electron microscopy involve measuring the shape bounded by the center of the atoms which is smaller than the Gibbsian values, whereas adsorption measurements will correlate with how close gas can approach the surface and will tend to be larger.

The minimum energy shape (discussed further in the next section) is then obtained by minimizing equation (6) at constant volume. If the strain and surface stress terms are ignored this is equivalent to minimizing the dimensionless parameter ε_W .

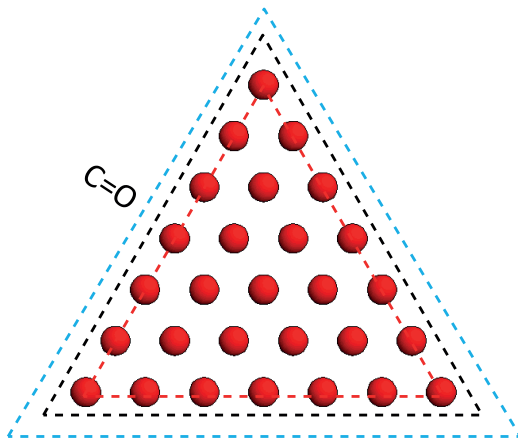


Figure 5. Illustration in the ambiguity in the size of a nanoparticle. The crystallographic size measured by scattering experiments such as x-ray diffraction would be the red line, that from chemisorption the blue line whereas the thermodynamic size (equimolar partition) is between these in black.

As an alternative, we can also consider a Lagrangian approach where we minimize

$$L = \int \gamma dS - \lambda \int dV \quad (9)$$

Setting the variation to zero for any and all facets (or curved regions) leads naturally to an additional term called the ‘weighted mean curvature’, the ratio of the change in surface energy (E_S) for a given facet (including surface stress contributions) and the change in volume V [66]:

$$wmc(h_i) = \lim_{\delta \rightarrow 0} \Delta E_s(h_i + \delta h_i) / \Delta V(h_i + \delta h_i) = \mu^s(h_i) / v_0 \quad (10)$$

where $\mu^s(h_i)$ is the chemical potential for facet i as a function of h_i and v_0 is the atomic volume. Similar to other terms, the variables in equation (10) can be either Gibbsian or fully classical. Note that if four or more facets meet at a corner some care is needed to distinguish limits for $+/-\delta$ due to the derivative discontinuity. Where the weighted mean curvature differs from the surface free energy is that it can be used for shapes which are not flat, for instance rounded corners and edges. For instance, for faceted nanoparticles the weighted mean-curvature is piecewise continuous and from solid geometry will scale with h_i as shown in figure 6 as

$$wmc(h_i) = \bar{\gamma}_i / (L_i - h_i) \quad (11)$$

where the facet disappears for $h_i \geq L_i$ and equations (10) and (11) define a weighted mean surface energy $\bar{\gamma}_i$. The chemical potential goes towards infinity as the facet gets smaller, which is not an artifact of a continuum model as verified by density function calculations [67] shown in figure 6. This implicit singularity in the chemical potential for corners has been known for a long time, and is frequently handled in numerical models by adding a curvature regularization term (e.g. [68–76]. and references therein). Note that this indicates that sharp corners are energetically unreasonable in most cases, rationalizing the fact that most experimental particles show at least some rounding [67], a topic we will return to later.

Since many nanoparticles also contain strains with the strain energy density implicitly a functional of the shape, in principle a fully rigorous description would include a term

$$w(h_i) = \lim_{\delta \rightarrow 0} \Delta W_D(h_i + \delta h_i) / \Delta V(h_i + \delta h_i) = \mu^W(h_i) / v_0 \quad (12)$$

To date there is no evidence that this shape-dependent strain energy contribution to the chemical potential matters for solution growth, although it is known to be important in epitaxial growth (e.g. [77–79].), and there are special cases where minima of the strain energy for certain sizes is believed to be important in favoring specific sizes of precipitates [80]. The role of this term for the energetics of very large Dh will be mentioned briefly later in section 5.1.

The bulk chemical potential will vary with temperature, pressure etc., but when comparing different shapes this cancels out. There will be a weak dependence of the strain energy upon temperature, but this can almost certainly be neglected. Both the surface free energy and the surface stress will depend upon temperature, and in particular the environment. While there is now relatively good data on the surface free energy of most metals and they can be calculated fairly accurately with more recent functional via density functional methods, less is known about the variation with chemisorption. When the surface is clean surface free energies are of the order of one to few $J m^{-2}$, but can be reduced by a factor of 2–3 when other species are adsorbed onto the surface. For most metals the surface stress tensor is positive, i.e. the surface free energy is lower when the atoms are closer together. However, with chemisorption this need not be true and the sign of the surface stress tensor will change depending upon whether there are attractive or repulsive interactions between molecules on the surface as illustrated in figure 7; that this can occur for small molecules on metals is very well established (e.g. [81, 82].), less well known but shown to exist for larger molecules [83].

For other materials such as oxides how the terms vary with chemisorption is much less clear, with relatively few measurements and only a few calculations. Complicating matters further, there may well be rearrangements of the surface atoms to yield reconstructed surfaces. These are well known for many of the simple metals, and have been observed in a number of cases for nanoparticles in vacuum. It is only rather recently that they have also been observed on oxide nanoparticles as shown in figure 8 [84, 85], where the exact structure formed depended upon the synthesis conditions. For strontium titanate nanocuboids synthesized by a hydrothermal route involving oleic acid, strong chemisorption of the acid on the surface favored a strontium oxide termination—strontium is the more electropositive atom. For synthesis using acetic acid which is highly water soluble, a titanium dioxide double-layer surface forms similar to what occurs for mesoscale (100) surfaces [86–101] due to dissolution of strontium from the near surface region. How general this is for other materials, and what the size of the energy changes and their consequences needs more research.

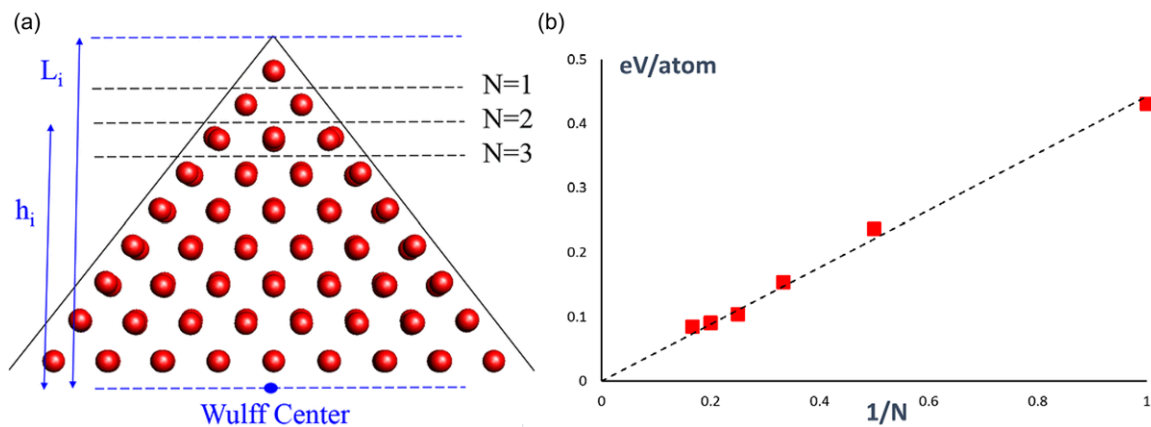


Figure 6. Density functional theory results for the chemical potential (weighted mean curvature) in the limit of small sizes. In (a) the model used indicating truncations for $N = 1, 2, 3$ with the corresponding equimolar surfaces and facet length, and (b) the chemical potential as a function of truncation. Within numerical accuracy the scaling matches very well to the continuum expectation.

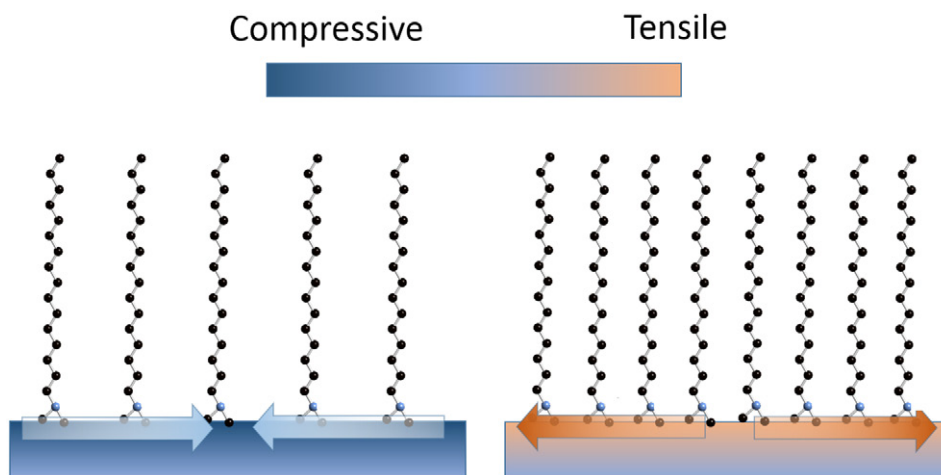


Figure 7. Illustration of how chemisorption can affect the surface stress. On the left when chemisorbed molecules are far apart attraction between them and the intrinsic changes of a metal surface will lead to a compressive stress; on the right when they are too close the surface stress will be tensile. Changes in the surface stress with coverage will occur for large ligands, as drawn, or for smaller chemisorbed species such as water, oxygen or carbon monoxide.

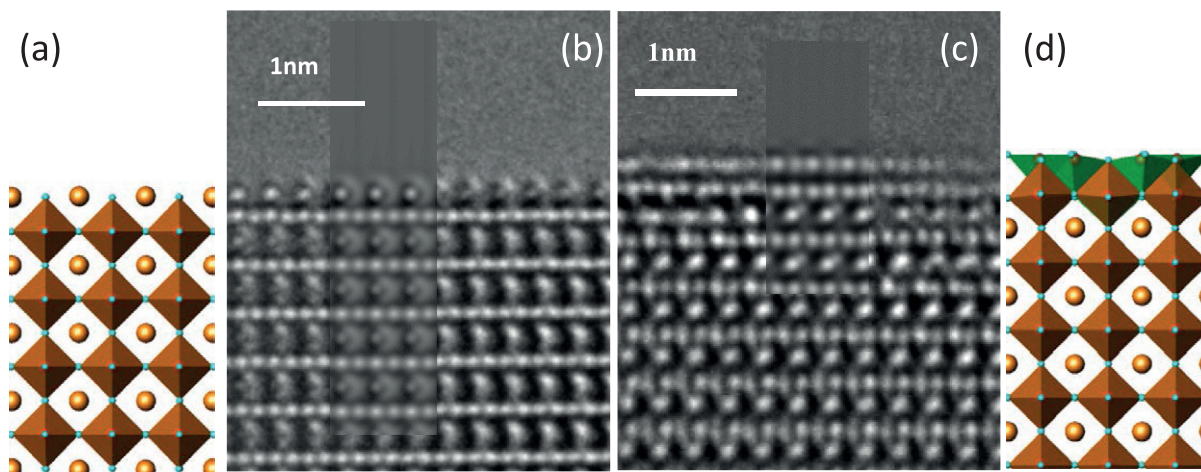


Figure 8. Images of the surface of SrTiO_3 nanocuboids prepared in different conditions. On the left in (a) and (b) with oleic acid, which leads to a SrO termination and on the right in (c) and (d) in acetic acid which leads to a TiO_2 double layer. The surface are shown with brown tetrahedral for TiO_6 units, green for TiO_5 and the Sr are gold.

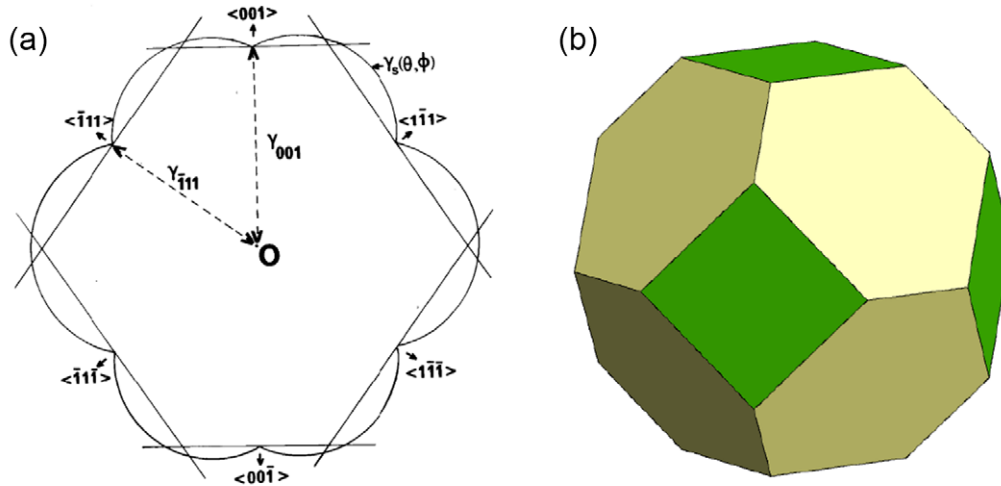


Figure 9. Illustration of the Wulff construction for a fcc material where $\{111\}$ and $\{100\}$ surfaces dominate, drawn for a $[110]$ projection on the left in (a), and the corresponding 3D shape on the right in (b), with green for $\{100\}$ and yellow for $\{111\}$.

3. Minimum energy solutions

We next turn to discuss the thermodynamic equilibrium shape of nanoparticles ranging from single crystals to those on supports or ones with twin boundaries. As will be seen there are common elements to the solutions, for which the general term of Wulff constructions will be used. Overall there is excellent agreement between the models and experimental results at the semiquantitative level or better, and the models have strong predictive power.

3.1. Wulff construction for single crystals

In the absence of any strain terms the minimum energy shape at constant volume is the variational minimum of ε_w , equivalently, the total energy at constant volume, and also equivalent to a constant weighted mean curvature (chemical potential) for all facets. For a single crystal this is the thermodynamic Wulff construction, the shape (set of points) S_w given by [68, 102]:

$$S_w = x : x \cdot \hat{n} \leq \lambda \gamma(\hat{n}) \text{ for all unit vectors } \hat{n} \quad (13)$$

This shape is all the points x within $\hat{n} \leq \lambda \gamma(\hat{n})$, where \hat{n} is a unit vector defined by the crystallographic orientation of a face (hkl) , $\gamma(\hat{n})$ is the orientation-dependent surface free energy, and λ is a constant that accounts for volume. Another common way to express this relationship is through the definition of the envelope planes of the particle, as first proved by Von Laue [103] and Dinghas [104],

$$\gamma_i = h_i / \lambda, \quad (14)$$

where h_i is the normal distance from the center of the particle to a crystallographic facet i as defined earlier and γ_i is the orientation-dependent surface free energy of the facet.

The standard method to generate the Wulff shape is to plot the surface energy as a function of angle and take the inner envelope of points, as shown in figure 9 for the simplified case when only $\{111\}$ and $\{100\}$ facets are relevant. In general

nanoparticles are more complex than this with small additional regions of higher index facets. An alternative method which has some mathematical advantages is to use a vector definition instead of the scalar surface free energy [68, 102]. The Wulff shape is relatively easy to determine experimentally from electron microscopes images (either or both scanning electron microscope or transmission), and one example for strontium titanate is shown in figure 10 [105] where there is good agreement between experimental results on the left and the Wulff shape on the right, here constructed using the Wulff Maker software [106]. Depending upon exactly which facets dominate even a single crystal can have a complex shape, and figure 11 from [107] shows some examples for different single types of facets within the stereographic triangle for a cubic material. A point that will come up later is that the Wulff shape is always convex, but there are cases where nanoparticles do not have convex shapes.

3.2. Winterbottom and summertop for supported nanoparticles

The Wulff construction applies to a free-floating particle in vacuum, a gas or a liquid; changing the external medium will change the values of the surface free energies but nothing else. A second type of shape occurs when the particle is supported on a flat substrate when the substrate is assumed to remain flat. If the surface free energy of the metal particle is γ_i , there is an additional free energy term γ_A for the adhesion (per nanoparticle atom at the interface) when the exposed surface of the nanoparticle is replaced by an interface, which leads to an effective interfacial term of $\gamma_{\text{int}} = \gamma_i + \gamma_A$. This should be used instead of γ_i when calculating the total surface energy. The total interfacial free energy term can be either positive or negative depending upon the chemical bonding between the nanoparticle and the substrate. This will depend upon the chemical species, the misfit between the nanoparticle and the substrate as well as details of the interfacial structure. The equilibrium shape, called the Winterbottom shape [108],

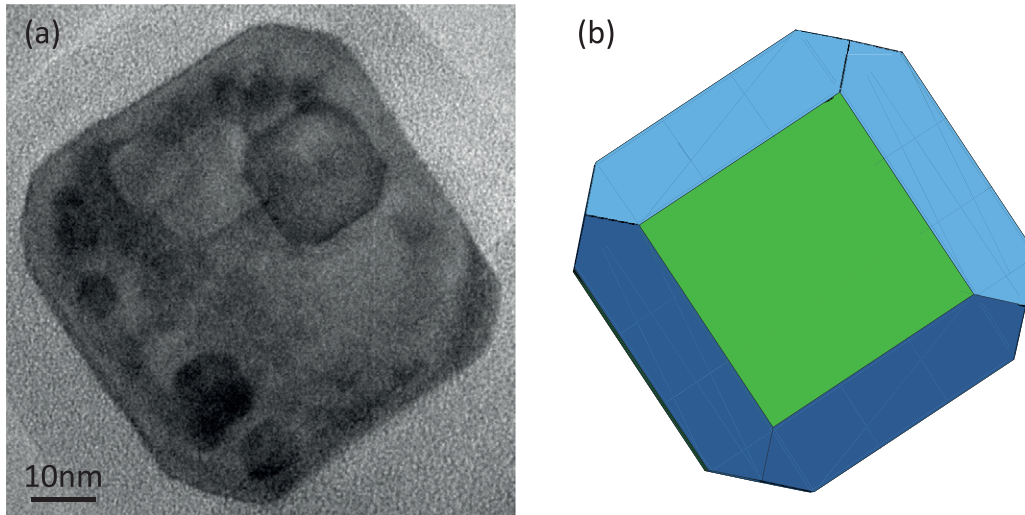


Figure 10. Experimental results for the Wulff shape of annealed strontium titanate nanocuboids based upon both the external shape and that of internal Kirkendall voids, an image on the left in (a) and the 3D Wulff shape on the right in (b) with $\{100\}$ green and $\{110\}$ blue. The ratio of the surface energies was $\gamma_{110}/\gamma_{100} = 1.139(55)$ from twenty nine measurements.

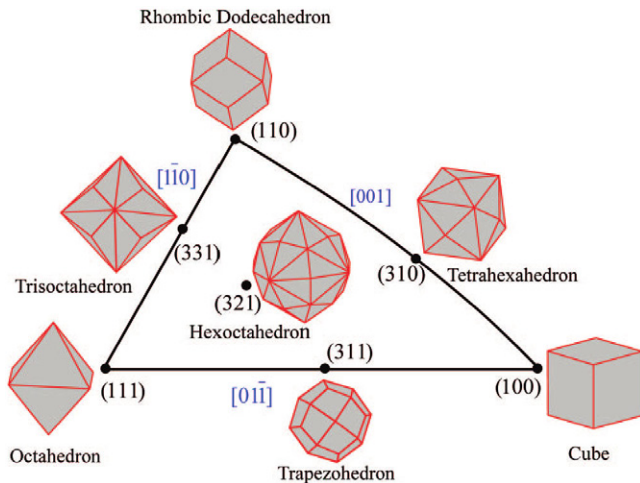


Figure 11. Illustration of some of the polyhedral within the stereographic triangle for an fcc material, Reproduced with permission from [107], copyright (2008) American Chemical Society. More complex shapes will occur from combinations of faces.

includes a facet to represent this interfacial energy in an otherwise standard Wulff construction. As illustrated in figure 12, if γ_A is greater than zero we have the equivalent of dewetting; if it is the negative of the surface free energy we have the equivalent of wetting with a full range in between. This can also be extended for two interfaces which yields the SummerTop construction [109], although this is rather rare in real physical systems.

Figure 13 shows experimental electron microscope images of the Winterbottom case, in (a) and (b) showing how the interface can depend upon the chemical character of the substrate [110], where in (b) the ceria has been slightly reduced due to testing for the water-gas shift reaction. As a caveat, as shown in figure 13(c) for gold on magnesium oxide, the substrate does not have to be flat and in this case the particle is

partially embedded in the support [111, 112]. Partial embedding of the particles may be quite common particularly with heterogeneous catalysts, and to date does not have any simple model although shapes can easily be predicted by numerical minimization of the total energy.

3.3. Modified wulff construction for MTPs

Instead of a boundary to an external support, there can be internal boundaries, most frequently in nanoparticles twin boundaries. The general approach is to find the minimum energy shape for each single crystal subunits with the twin boundaries taken into account, and then assemble the composite particle from these units, see figure 14. Similar to the Winterbottom construction we associate an additional free energy γ_T with each twin boundary, but different from it then partition this to the two sides and generate a variant of the Wulff construction for each single crystal subunit. Finally the subunits are assembled to create the full twinned nanoparticle. This approach was called the ‘modified Wulff construction’ [63, 65]. Each individual single crystal subunit will be convex, but the overall composite particle does not have to be.

In a set notation the modified Wulff construction can be written as the superset of Wulff shapes S_m for all the individual single-crystal subunits where

$$S_m = x : (x - o_m) \cdot \hat{n} \leq \lambda_m \gamma_m(\hat{n}) \text{ for all unit vectors } \hat{n} \quad (15)$$

where the O_m are the origins for each single-crystal unit, $\gamma_m(\hat{n})$ the surface free-energy appropriately oriented in space which includes a ‘twin facet’ energy for each segment ‘ m ’ adjacent to a segment ‘ n ’ of $\alpha_{mn}\gamma_n$, with the additional conditions

$$S_{mn}^t = S_{nm}^t \text{ and } \alpha_{mn} + \alpha_{nm} = 1 \quad (16)$$

with S_{mn}^t is the bounding twin surface of segment ‘ m ’ where it joins to segment ‘ n ’.

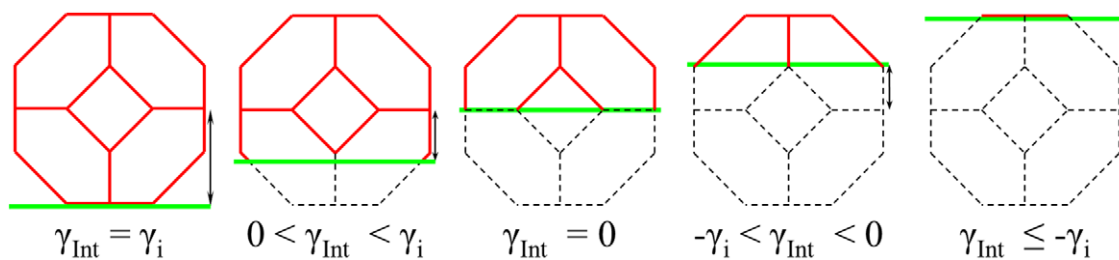


Figure 12. Schematic of the variation in shape of a nanoparticle, here with a (100) epitaxy on the substrate, as a function of the net interfacial free energy. From left to right is the solid analogue of dewetting to wetting.

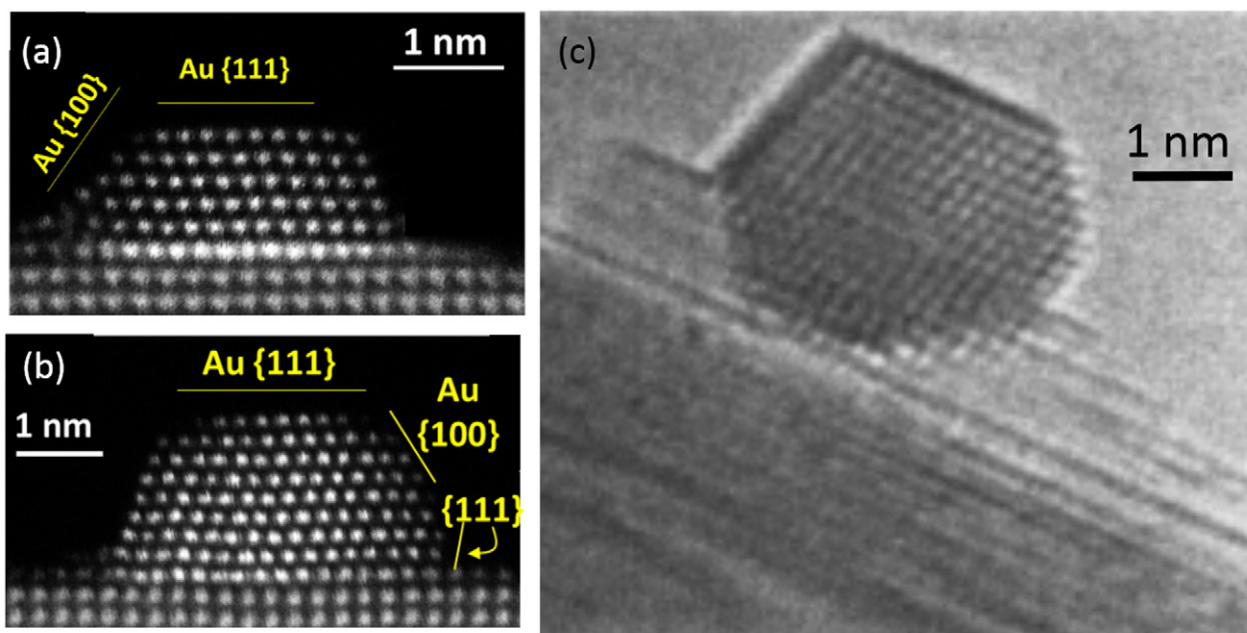


Figure 13. Experimental images in (a) and (b) for gold on ceria supports where the sample in (b) has been catalytically tested. Due to reduction of the ceria the interface and Winterbottom shape changes. Shown in (c) is an example for gold on magnesium oxide (where the interface is not flat).

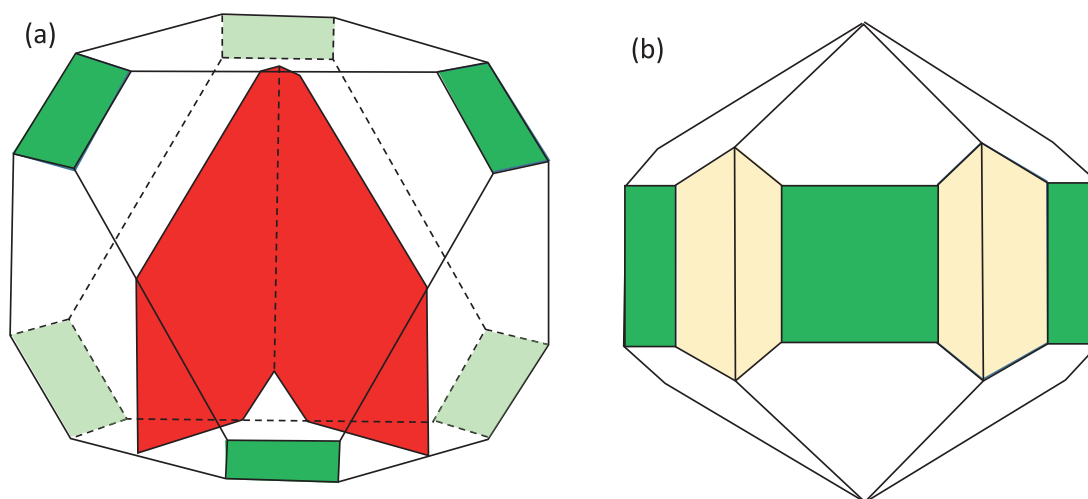


Figure 14. Illustration of the modified Wulff construction. For the 3D Wulff shape shown on the left in (a) the region between two twin planes (red) is extracted. Five of these joined at the twin boundaries leads to the Dh shape shown on the right in (b), with the re-entrant {111} surfaces in yellow. In both diagrams {100} faces are green.

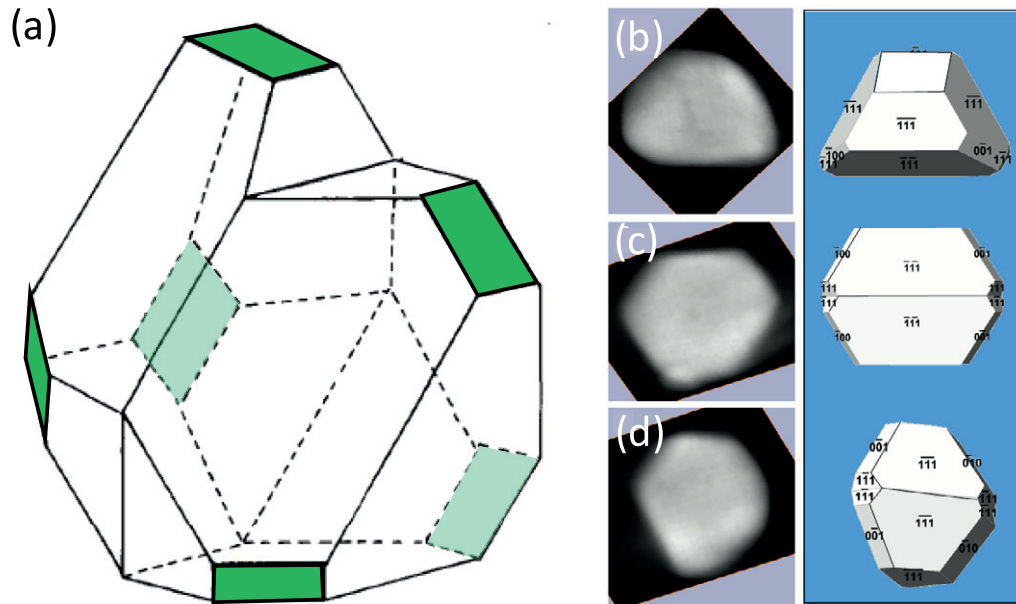


Figure 15. Shape of a LTP on the left with one twin boundary for only $\{111\}$ and $\{100\}$ facets, the later green with an experimental example of 3D tomographic analysis projected onto three directions, in (b)–(d) which are in good agreement with the theoretical prediction. Parts (b)–(d) are reprinted with permission from [113] after a slight modification, with thanks to R Dunin-Borkowski for supplying an original. Copyright 2009 Oxford University Press.

The simplest case is with $\alpha_{mn} = 1/2$ and all λ_m the same, the symmetric solution. One twin plane gives a singly twinned particle, while a sequence of parallel twin boundaries gives a family of lamellar-twin particles or LTPs, first observed in the inert gas evaporation literature [49–55]. Figure 15 shows the 3D shape of the a single-twin LTP from the construction [63] together with experimental results based upon an electron tomography experiment projected in three directions [113]. Using five segments each bounded by two non-parallel planes gives a Dh (see figures 14 and 16, the later from [114–116]), slightly different forms depending upon the surface free energies; twenty segments bounded by three non-parallel boundaries, an Ic (see figure 17 from [115–117]) with again a number of variants depending upon which facets have the lowest surface free energy.

From the properties of the Wulff construction, for specified values of α_{mn} and λ_m this is the global minimum total surface energy shape. With respect to variation in α_{mn} and λ_m it may be a constrained local minimum in order to satisfy $S_{mn}^t = S_{nm}^t$ or alternatively a saddle point. Numerical calculations for a Dh yield a minimum for only $\{111\}$ and $\{100\}$ faceting [118] although it is a saddle-point for an isotropic surface free energy [63, 65]. There is currently no analytical theory describing what values of the surface-free energy anisotropy the construction are minima versus a saddle points, a topic that merits further attention. Asymmetric partitioning of the twin boundary is also possible ($\alpha_{mn} \neq 1/2$), in which case the scaling term λ_m for each segment is different. This leads to some of the asymmetric nanoparticle structures observed experimentally [63] and described further below.

Since the construction can be a saddle point with respect to breaking of the overall twin symmetry we need to include an

addition clarification. If a particular structure can be (at certain sizes) the lowest possible energy configuration, we will refer to it as a *globally thermodynamic* structure. If, however, it is only a local minimum when all the twin segments are the same, we will use the term *constrained thermodynamic* structure.

The most common example of the modified Wulff construction for face-centered cubic (fcc) materials occurs when only the $\{111\}$ and $\{100\}$ surfaces are low energy, in which case one obtains the shape shown in figures 14 and 16(a). One feature which makes this different from most shapes is the presence of a re-entrant surface at the twin boundaries, different from single crystals which are always convex. In their early atomistic work Cleveland and Landman coined the term ‘Marks Decahedron’ for this, which has now become a generic term frequently appearing without citation.

The term Marks decahedra has become common in the literature, but is only one example and the construction is more general than commonly used in the literature. If the free energy of the $\{100\}$ facets is decreased such that $\gamma_{111}/\gamma_{100} > 2/\sqrt{3}$, these notches disappear and the particle elongates to a rod-like shape similar to that first investigated by Ino [39–41] (see figure 16(b)). This is a constrained thermodynamic structure, not a global minimum. If instead the $\{100\}$ energy is increased and is much larger than the $\{111\}$ energy ($\gamma_{111}/\gamma_{100} \ll 1$) the $\{100\}$ faces no longer appear in the minimal energy shape, and the result is a star decahedron (figure 16(c)), similar to those found in several cases [119]. This is a plausible global thermodynamic structure. Addition of $\{110\}$ facets will lead to more rounded structures, as will inclusion of other higher-index surface facets if these are of low

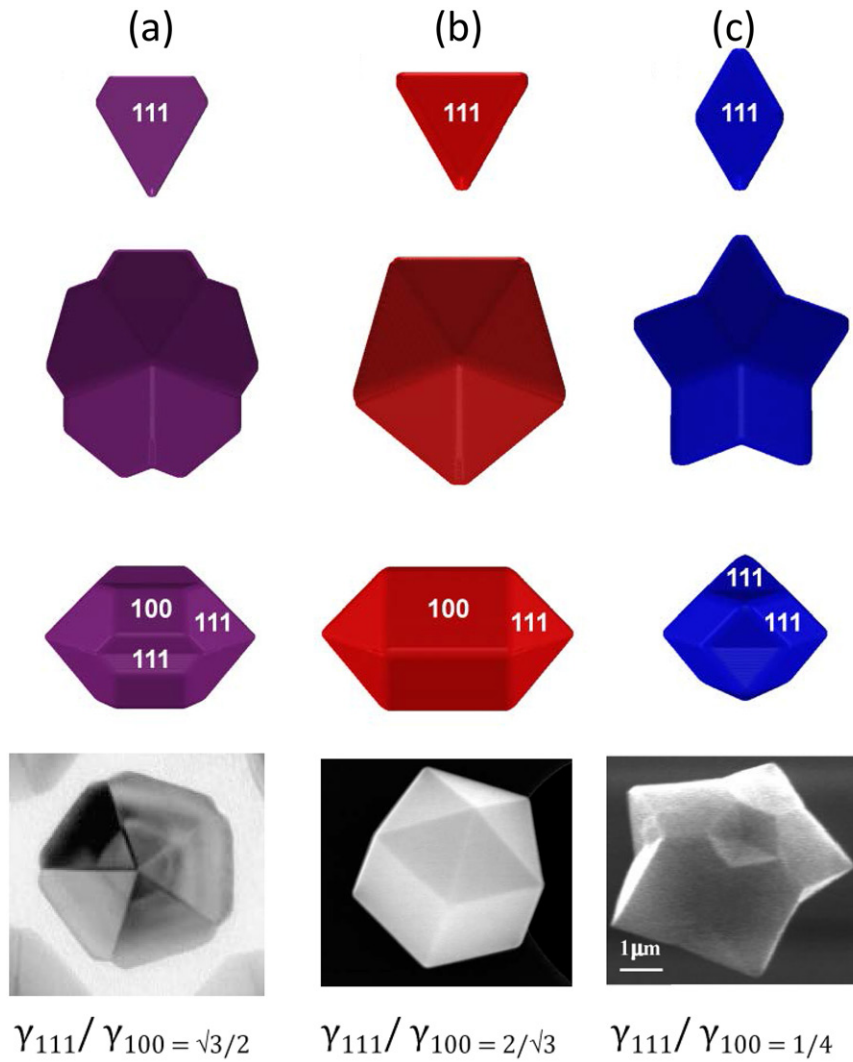


Figure 16. Different cases for Dh in three columns (a)–(c) with different ratios of the $\{111\}$ and $\{100\}$ surface energies. Shown at the top is the single segment, below the particle down the common $[011]$ direction and below from the side. Experimental images are shown below, on the left reproduced with permission from [114], copyright 2014 J Wiley and Sons, in the middle reproduced with permission from [115], copyright 2012 Royal Society of Chemistry, and on the right [116], courtesy of M J Yacaman.

enough surface free energy although these are always higher in energy than single crystals. In general a combination of $\{110\}$ and $\{111\}$ is a global thermodynamic structure.

For the icosahedral particles the possibilities are more limited. If $\{111\}$ surfaces dominate one has the conventional icosahedron as shown in figure 17(a). There will be marginal stability if $\{110\}$ surfaces dominate which yields a regular dodecahedron as shown in figure 17(b), and there can be intermediate cases as also shown in figure 17(c).

With clean surfaces the twin-boundary energy is small compared to the surface free-energies and can be taken as zero to first order, in which case the origins O_m are common. This approximation, i.e. ignoring the changes in shape due to the twin but still including the energy contribution, is accurate to second-order in the energy [63, 65], and the difference in the shape will be below experimental error for vacuum or inert gas evaporation experiments. For solvent-based growth the surface free energies may be substantially lower and this leads to re-entrant surfaces at the disclination line for both Dh and Ic, as sometimes observed experimentally [116] and outlined

in previous publications [63, 65]; for experimental examples see figures 16(c) and 17(d).

Values of ϵ_w for a few different particles with only $\{111\}$ and $\{100\}$ facets are given in table 1 [42, 63, 65] with the term β parameterizing the relative surface free energies given by

$$\beta = 1 - \gamma_{100} / \sqrt{3} \gamma_{111} \quad (17)$$

For clean fcc metals the surface free energy of $\{100\}$ is larger than that of $\{111\}$, so based just upon the surface energies, the Ic is lowest followed by the Marks decahedron then single crystals. The difference between single crystals and LTPs is so small that they can coexist and it is unlikely that LTPs will transform to the (lower energy) single crystals in most experimental conditions. Some other shapes such as a Dh with just a single (100) truncation (Ino Dh) as well as a pentagonal bipyramid with only $\{111\}$ facets ($\{111\}$ only Dh) are included in the table—these are always energetically unfavorable for typical values of the $\{100\}$ and $\{111\}$ surface free energies.

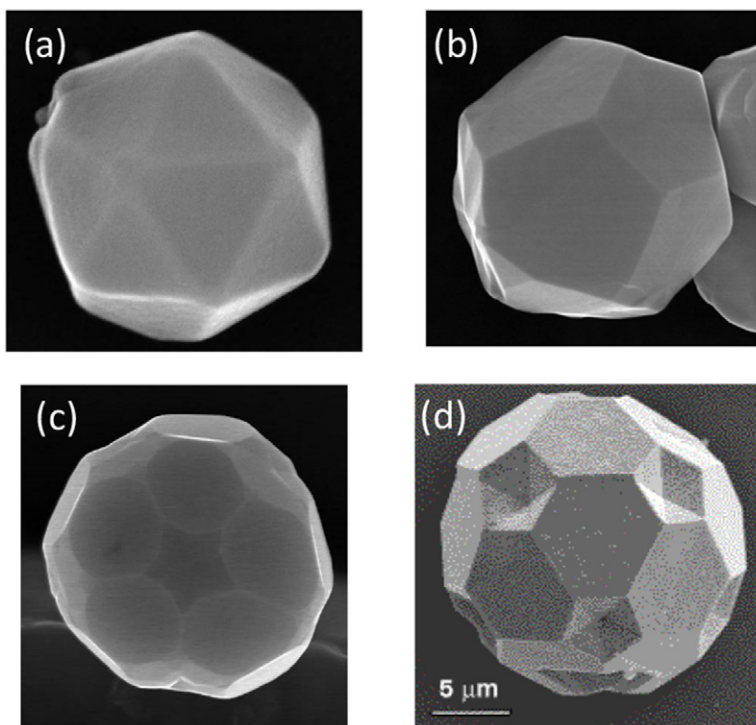


Figure 17. SEM images, in (a)–(c) and (d) in B_6O , showing different types of Ic, a regular icosahedron with $\{111\}$ facets in (a), a dodecahedron with $\{110\}$ in (b) and a combination of $\{111\}$ and $\{110\}$ in (c). In (d) the re-entrant surfaces at the twins are evident, indicating that the twin boundary energy is relatively large. Figures (a)–(b) [116], courtesy of M J Yacaman, (c) is reproduced with permission from [115], copyright 2012 Royal Society of Chemistry, and (d) from [117], copyright 1998 Nature Publishing Group.

Table 1. Values of ϵ_W for a few different particles with only $\{111\}$ and $\{100\}$ facets in terms of the parameterization of the $\{100\}$ and $\{111\}$ surface energies.

Particle		$\beta = 1/3$	$\beta = 5/12$
(111) Tetrahedron		7.206	7.206
(111) Octahedron		5.719	5.719
(100) Cube		6.928	6.062
Single Crystal		5.499	5.271
LTP with m twins	$m = 1$	5.500	5.272
	$m = 2$	5.500	5.273
	$m = 3$	5.501	5.274
	$m = 4$	5.502	5.275
Marks Dh		5.436	5.243
Ino Dh		5.593	5.281
(111) only Dh		6.192	6.192
Ic		4.899	4.899
Bi-Ic		5.051	5.051
Asymmetric Twin		N/A	5.272
Asymmetric Dh		N/A	5.256

If the $\{100\}$ surface energy is low a rod shaped Dh will be a constrained thermodynamic shape, never a global minimum. These shapes as well as the Ino Dh and tetrahedra are always higher in energy, explaining them by global thermodynamics is a scientific urban myth.

A few more complex shapes are included in the table with are sometimes observed experimentally. One set of structures included are asymmetric particles as illustrated in figure 18; the portioning of the twin boundary energy does not have to be equal. There are relatively few reports of these particles

in the literature. Sometimes they may be missed with the eye drawn more to the symmetric variants, or they may not have a true stability—at best they are constrained minima. They have intermediate surface energies, as shown in table 1.

There are also many more complex particles which were originally termed polyparticles. If we again assume a constraint that the twin boundaries cannot be eliminated there are many more ways to assemble structures which are local minima, not necessarily global minima. One of these is a Bi-Ic where five segments are shared between two Ic, see figure 19; a different example shown in figure 20 which was observed in very rapidly quenched gold nanoparticles [120]. These more complex particles were first described by Komoda [45] and then analyzed in some detail by Smith and Marks [47]. They can be described as larger scale analogues of the polytetrahedral structures first considered by Hoare and Pal [48, 121, 122]. They have been rediscovered in the literature many times.

We can generalize for when Ic and Dh are lower in surface energy than single crystals. From solid geometry the total surface energy can be written, (ignoring the twin boundary contribution) in terms of the parameter ϵ_W as:

$$\epsilon_W = \left[\frac{9}{\gamma_{111}} \{N_1 S_1 + N_2 S_2\} \right]^{1/3} \quad (18)$$

Where S_1 and S_2 are the integrated total surface free energies of the two regions R_1 and R_2 of the stereographic triangle in figure 21, and N_1 and N_2 the numbers of each of these regions in the different types of particles. For a single crystal and LTPs $N_1 = N_2 = 48$; for a Dh $N_1 = 60$, $N_2 = 40$ and for an

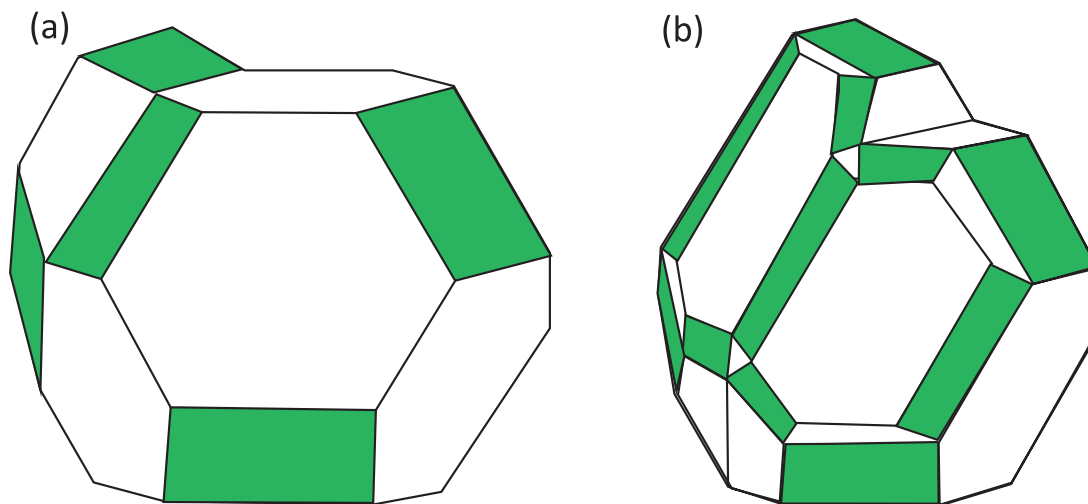


Figure 18. Asymmetric solutions, on the left in (a) for a LTP and on the right in (b) for a Dh.

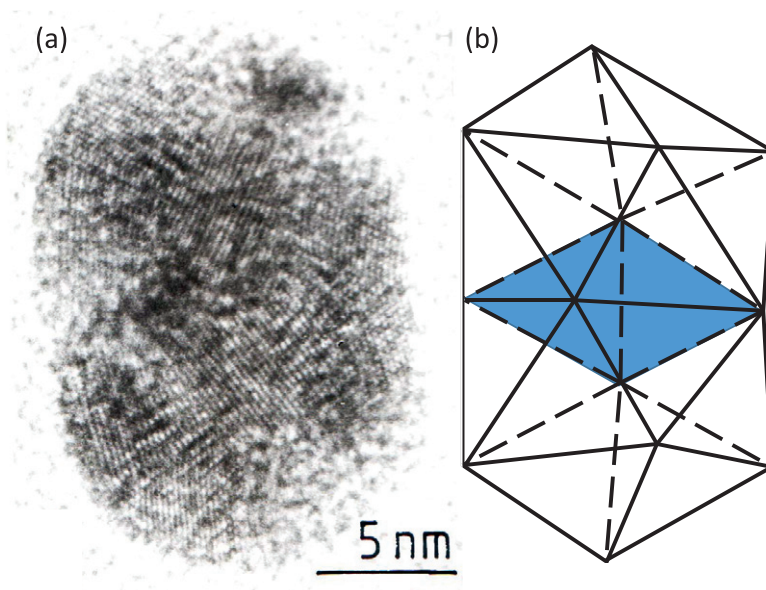


Figure 19. Somewhat old HREM images of a bi-icosahedron on the left in (a), with a model of the structure showing the shared decahedral unit in blue on the right in (b).

ic $N_1 = 120$, $N_2 = 0$. Hence so long as the average surface energy of region 1 is less than that of region 2, MTPs will have lower total surface energies. That MTPs are only stable when the $\{111\}$ surface energy is small is an urban myth—this is a sufficient but not necessary condition. For instance, if only $\{110\}$ faces are present the values of ϵ_W are almost the same for a single crystal (rhombic dodecahedron) and icosahedron (dodecahedron) at 5.345 and 5.312 respectively times the ratio $\gamma_{110}/\gamma_{111}$.

While the modified Wulff construction has proved to be successful in rationalizing some observations, most notably for the Dh with re-entrant surface in the thermodynamically lowest-energy shape, it does not explain everything. Perhaps the simplest shortcoming is a pentagonal biprism with only $\{111\}$ facets. While these were described in the original papers on MTPs [39–41] no thermodynamic argument will give their shape as a minimum-energy configuration—that they are a minimum-energy shape is a common misconception. Other shapes

cannot be explained, such as sharp bipyramids, which have been synthesized using various protocols [123–125] as well as truncated bitetrahedra, triangular platelets, and Dh rods, see for instance figure 2. In many papers these have been loosely attributed to ‘kinetics’; we will return to this in section 4.

3.4. Other variants

While the Wulff, Winterbottom and modified-Wulff are the three most common cases, there are some others which will be briefly described in this section.

3.4.1. Alloy wulff construction. The addition of a second element makes the structures of bimetallic nanoparticles more complex than their monometallic counterparts. The two elements can be phase separated as in core-shell structures [126–128], chemically ordered [129–131], have Janus [132, 133] structures, or the two species can be randomly

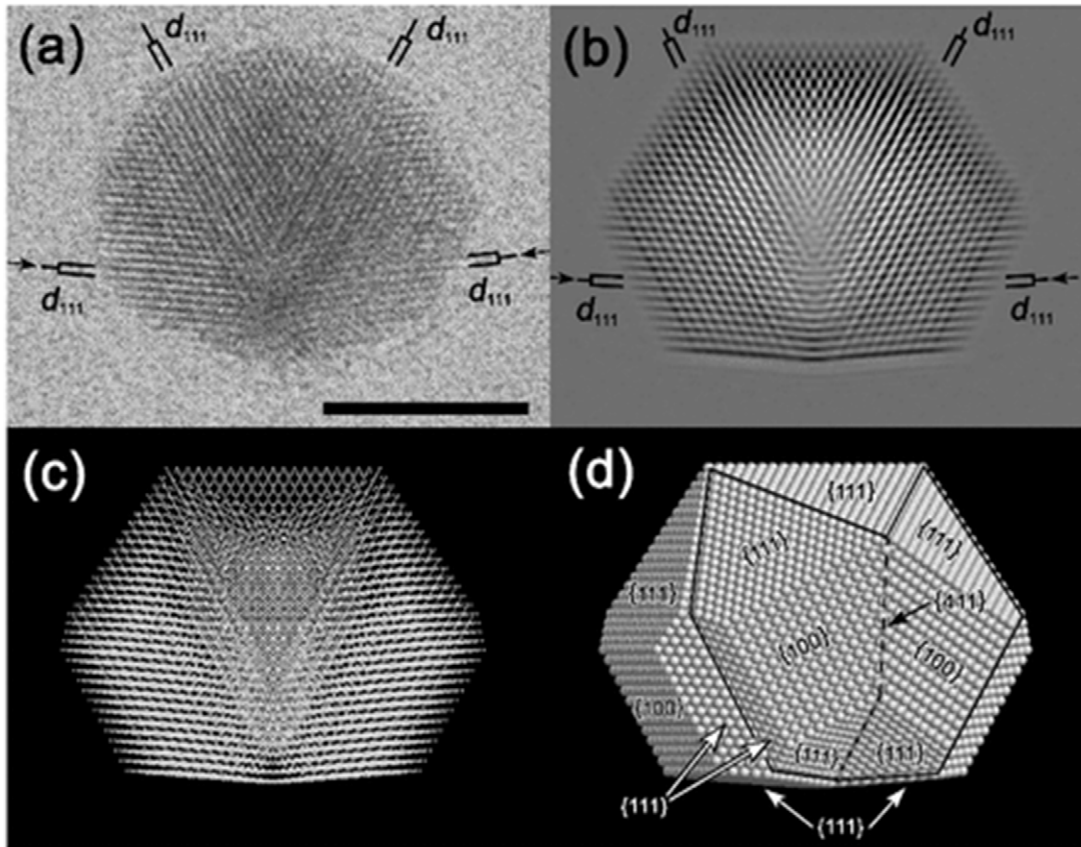


Figure 20. Bi-decahedral particle of gold, in (a) image, (b) simulated image, (c) positions of atoms in projection from the image and (d) a schematic model. Note that the particle has re-entrant notches similar to a Dh. Reproduced with permission from [120], copyright 2006 The American Physical Society.

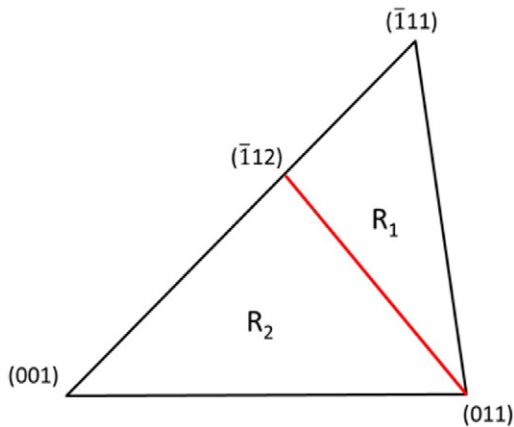


Figure 21. Stereographic triangle split into the two regions R_1 and R_2 . MTPs have more of region R_1 .

mixed with complex segregation [134–136]. For large sizes segregation of one species to the surface to reduce the surface free energy is straightforward, and has been extensively studied for flat surfaces. However, in a nanoparticle there is an additional contribution as removing atoms from the bulk to the surface changes the total energy contribution of the bulk. This cannot be ignored, especially when the number of bulk and surface atoms are comparable. This is also a constraint upon the composition, an additional Lagrangian variable in the formulation for the minimum energy of the nanoparticle.

This leads to a slightly different form of the solution, namely

$$\frac{\gamma(n, C_1^S, C_1^V, C_2^S, C_2^V, \dots)}{\{\Lambda - \Delta G\}} = h(n) \quad (19)$$

Where an additional term has been introduced to account for the bulk dealloying terms. This form is described in more detail in [137], and leads to a size dependence of both the segregation and the shape, see figure 22 where the ratio of the distances to $\{111\}$ and $\{100\}$ facets is plotted as a function of the overall gold concentration for three different particle sizes. While there is relatively little experimental and computational data as yet, overall it appears to be quite consistent with the predictions of this model [138].

It worth mentioning that the entropy of mixing plays a role in bimetallic/alloy systems—the free energy has contributions from both enthalpy and entropy. At low temperature, the contribution from entropy of mixing is minimal, so the enthalpy term dominates. However at high temperature, the entropy of mixing will dominate and will drive the particle towards homogeneity. Therefore, surface segregation is temperature dependent and is more significant at lower temperature. One caveat we note here is that experimental results often represent quenched structures and surface ligands are known to have effects on surface segregation [139].

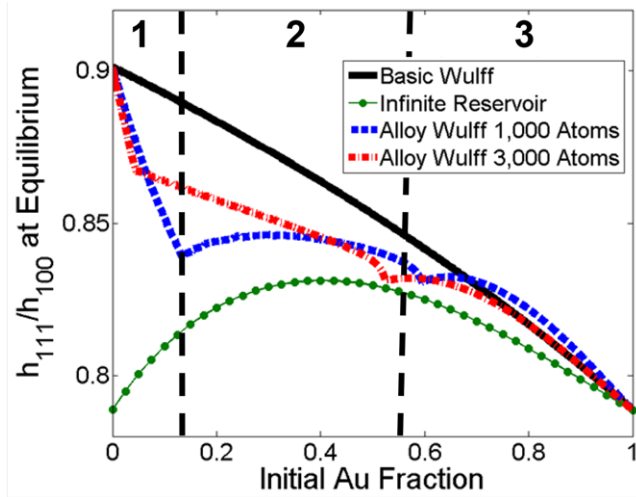


Figure 22. Variation in the relative distance to a $\{111\}$ versus a $\{100\}$ facet for CuAu alloy nanoparticles, as a function of size as well as with different approximations for the surface segregation. In region 1 there is not enough gold for full segregation to the surface, in 3 there is more than enough and in region 2 surface segregation and bulk desegregation compete.

3.4.2. Surface excess case. A second case is worth mentioning, what happens if there is a surface excess of a given species which does not alloy with the bulk. For instance, there is evidence that the surfaces of strontium titanate nanocuboids depend upon the synthesis conditions as shown earlier, and can be either strontium oxide terminated or have titanium dioxide rich double-layer surfaces [85]. The minimum energy shape involves an additional constraint that the excess of (for instance) TiO_2 integrated over the surface is a constant. Similar to the alloy Wulff case, this will lead to a slightly different solution and it is easy to show that it will take the form:

$$\gamma_n(C_1, C_2 \dots C_n) - \mu(C_1, C_2 \dots C_n) = h_{(n)}/\lambda \quad (20)$$

where the chemical potential is now generalized to be a function of surface compositions $C_1, C_2 \dots C_n$ and there is an implicit constraint on the total surface excess set in most cases by the growth conditions.

In many cases the chemical potential will be set by the external medium. An interesting possibility exist if there is equilibration between different faces, but they have different chemistries. To date this has not been measured to our knowledge at the nanoscale, but should be possible with modern transmission electron microscopes. We will predict that surface chemical differences are common, for instance in oxide supports used in heterogeneous catalysts.

3.4.3. The effect of size dependent strain. When the size of the nanoparticles is small enough, the additional terms that neglected earlier have to be included, which will lead to deviations from the Wulff construction (e.g. [140]). Exactly where this takes place has been debated for many years, and probably depends upon the material and the calculation method. As a caveat, in some cases the rigorous Gibbs equimolar partitioning of the nanoparticle has not been performed outside the surface, and this is needed to properly achieve the transition

from atomistic to continuum models [59, 60], so the magnitude of the deviations may be exaggerated.

The best known example of a size effect is the lattice contraction of small particles driven by the surface stress. Assuming for simplicity a homogeneous strain and an isotropic surface stress (which will be a good approximation for a cubic material), there is a fractional change in lattice parameter $\frac{\Delta a}{a}$ for a spherical particle given by

$$\frac{\Delta a}{a} = -\frac{4gK}{3R} \quad (21)$$

where K is the compressibility and R is the radius. This has been extensively analyzed in the literature (e.g. [141–163]), and is typically a few percent for particles of 5 nm radius and normally (but not always) a contraction. Shown in figure 23 is data for Ag_3Sn which shows a contraction [163] whereas anatase TiO_2 shows an expansion [161]. We note that sometimes the lattice contraction is considered with a surface free energy in the equation above rather than the surface stress; this is not correct.

The above is for the homogeneous strain, which will be the leading term, but there are inhomogeneous strains as the surface stress tensor will be crystal face dependent. There have been a few recent measurements of these spatially resolved details of the additional inhomogeneous strains, e.g. [83, 164–173], using coherent diffraction imaging methods. These are generally consistent with the conventional models of surface stress effects although they also see strain due to the substrate, see for instance figure 24. In this figure the inhomogeneous component for a lead particle has an expansion at the surface except along $[111]$, and there is a local compression at the interface to the silica support shown in blue. Whether the lattice parameter contracts or expands both globally and locally depends upon the material as well as chemisorption, the latter being particularly important. This area is still developing, and from the current literature it is not clear whether models and experiment are in complete agreement.

A second case is well known for epitaxial nanoparticles on a substrate. For the growth of semiconductors at a slightly larger scale (typically 50–500 nm particles) the literature is large and there is generally good agreement between models where the elastic deformation of the nanoparticles, the surface stresses and the misfit stresses at the interface are all included; see for instance [79, 81, 174–186] and references therein. The thermodynamic minimum energy shape minimizes not only the external surface energy but also the interface strain energy so will deviate from the Wulff shape [187–189], and it may also be important to include line energy terms for the vacuum/substrate/nanoparticle three-phase interface (e.g. [190–192]). An example of this is shown in figure 25 where the results indicate a size-dependent Wulff shape. The authors [190] attributed this to the triple-junction line tension having a role at very small sizes although it is not clear to us whether this might not be a consequence of misfit strain. For completeness, we should mention that it has been known since the early work on epitaxy that nanoparticles often nucleate at steps, so there can be further deviations away from the Wulff shape as recently pointed out by Gao *et al* [193].

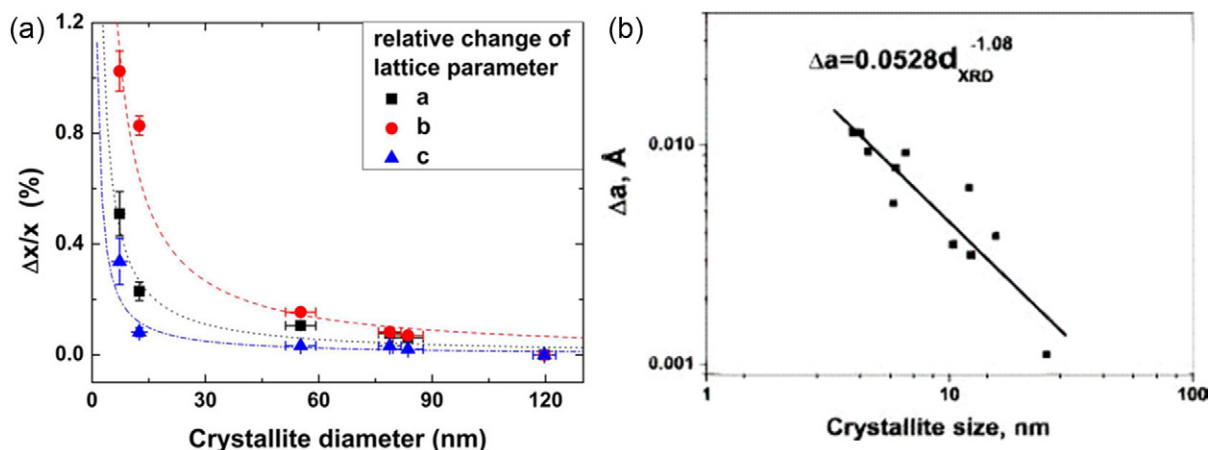


Figure 23. variation in lattice parameter with size, in (a) showing the relative decrease in lattice parameter at small size in Ag_3Sn reproduced with permission from [163], copyright (2015) American Chemical Society (sign reversed compared to common usage) and in (b) for anatase TiO_2 showing an expansion, reproduced with permission from expansion [161], copyright 2009 AIP Publishing LLC. As a rule the expansion/contraction depends upon material and chemisorption.

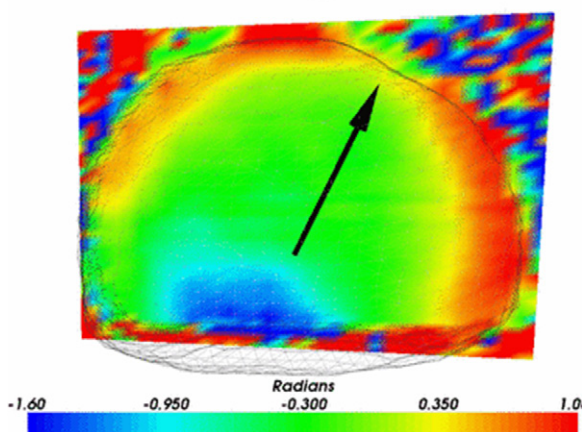


Figure 24. Map of phase changes in a lead nanoparticle on amorphous silica, the phase changes correlate to local displacements. In addition to a compression at the interface (blue), there is a local expansion at the surface (red) which is less along the [111] direction. Reproduced with permission from [165], copyright 2007 American Physical Society.

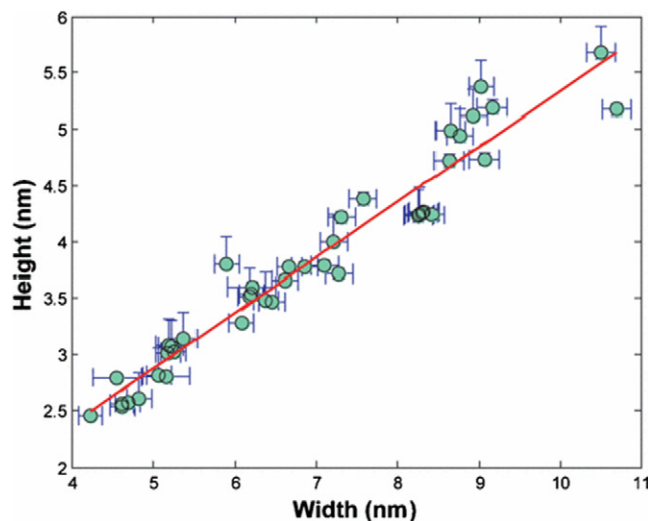


Figure 25. Plot of the nanoparticle height versus width for gold on rutile TiO_2 (1 1 0). For a Wulff shape the intercept should go through the origin, but it does not. Reproduced with permission from [190], copyright 2010 American Physical Society.

Overall the topic of coupling strain to the shape of nanoparticles is relatively mature with good predictive models and literature available.

4. Kinetic shapes

The various Wulff constructions yield the equilibrium shape. However, it is not clear that many experimental nanoparticles are synthesized or treated afterwards such that they reach equilibrium. Instead the shape is a consequence of kinetic growth. While there are similarities and the two are frequently confused they are fundamentally different. The fact that kinetics matter particularly for solution growth has been known for a long time, for instance in the early work of Berg [194] and the detailed review and analysis of different terms by Bircumshaw [195], both of which cite even earlier literature. There is also an extensive early literature for flat crystal

growth, for instance the work of Volmer [196] and Burton *et al* [197]. The kinetic models that will be described in the following sections are excellent for predicting nanoparticle shapes qualitatively and in principle quantitatively, although the necessary parameters for the later are not well measured in much of the current literature.

To aid in the analysis, it is useful to break down the processes taking place during growth by considering three regions as illustrated in figure 26. Far from the particle one has Region I with some concentration of the relevant materials, dictated by the environment. Around the particle is Region II which includes atoms that interact directly with the growing nanoparticle, both via being chemisorbed onto the surface and as part of complexes. Lastly there is Region III composed of terraces of steps on the surface of the nanoparticle which grow by the attachment of atoms from Region II. There will be a net flux of atoms from Region I \rightarrow Region II \rightarrow Region III.

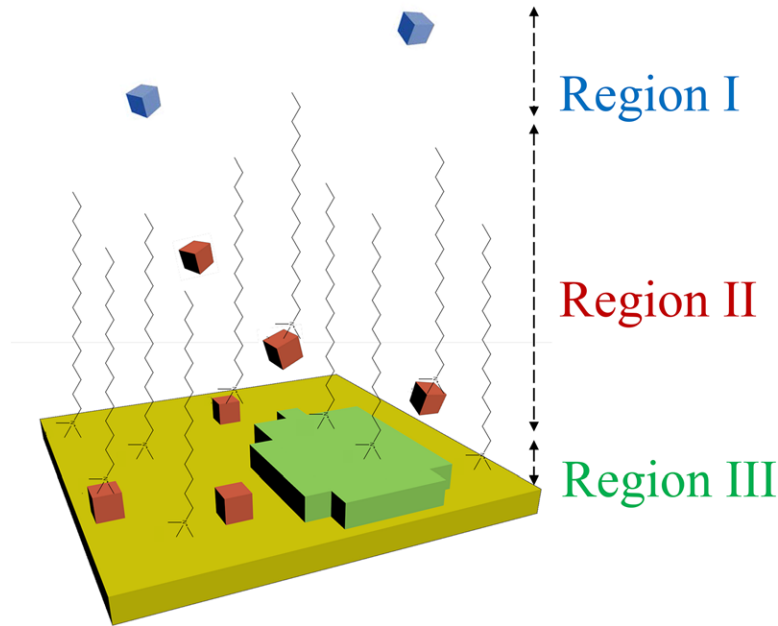


Figure 26. Schematic of the relevant regions for kinetic growth. Region III contains a nucleating terrace, Region II atoms that can diffuse to the terrace and Region I external atoms. Atoms are represented by cubes which are color coded by region, with the substrate yellow, and ligands near the surface are illustrated.

Diffusion limited growth occurs when the controlling term is diffusion in Region I to Region II, with atoms attaching very rapidly to Region III as they arrive. This limit typically leads to complex patterns such as snowflakes with dendritic or similar structures; the topic has been well described in the literature and will not be discussed further here.

Interface limited growth is more important for shape controlled nanoparticles, and is when atoms moving from Region II to Region III is rate limiting. If the size is small enough, as atoms are added the cluster will be flexible and the atomic arrangement can change. Above some size this will not be energetically possible, and the particle then acts as a seed for further growth. While there may still be some changes of the internal structure, this will be the exception.

The controlling terms are the nucleation of a small monatomic terrace on an existing flat facet, and the growth of this terrace across the facet, Region III. If nucleation is fast relative to the growth across this leads to rough surfaces. Flat surfaces occur when the nucleation is relatively slow. Making the simple approximation of a circular single atomic high terrace of radius R and introducing an edge energy γ_e per atom the total energy of the terrace can be written as

$$E = \pi R^2 \Delta\mu N_S + 2\pi R \gamma_e N_E \quad (22)$$

Where $\Delta\mu$ is the chemical potential change per atom (negative for growth) for addition to the nanoparticle versus being in Region II, N_S is the number of atoms per unit area of the terrace and N_E the number of atoms per unit length of step. Remembering that the chemical potential is negative, this has the classic form of a nucleation barrier as illustrated in figure 27. The height of the nucleation barrier depends upon the step energy and the chemical potential relative to the external media. From classical nucleation theory the rate of formation of a terrace above the critical size R_C is given by

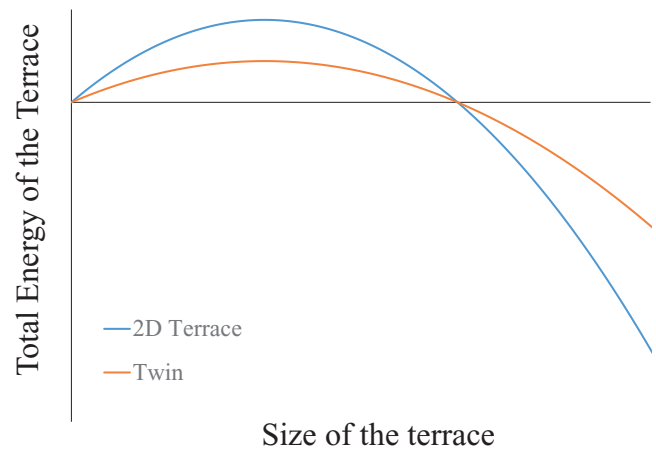


Figure 27. Energy versus size for a growing terrace, in blue a full 2D terrace as a disc and in brown for a half disc at a re-entrant twin boundary. As illustrated, the activation energy barrier will be substantially smaller for the latter.

$$\text{Rate} = f_0 \exp\left(\frac{-\Delta E}{k_B T}\right) \quad (23)$$

where f_0 is the attempt frequency of an atom to add to the terrace and ΔE is the nucleation barrier which for a 2D terrace gives a critical nucleus size of

$$R = -\gamma_e N_E / \Delta\mu N_S \quad (24)$$

and an activation energy barrier of

$$\Delta E = -\pi(N_E \gamma_e)^2 / N_S \Delta\mu \sim -\pi(\gamma_e)^2 / \Delta\mu \quad (25)$$

As an estimate, if we use a broken bond model and take the bulk cohesive energy as 4 eV per atom, for a $\{111\}$ surface

$\gamma_e \sim 2/3$ eV. If we are dealing with gas phase deposition the chemical potential of an adatom will be around (in eV)

$$\Delta\mu = -3 + k_B T \ln[c] \quad (26)$$

with $[c]$ the concentration of atoms in Region II that can add to the terrace. If the deposition rate is fast then the critical nucleus may be only 2–3 atoms, in which case there can be multiple terraces on any given facet and the growth will tend to lead to relatively rough surfaces. With slow deposition the concentration in Region II will be small, via the concentration, and the critical nucleus could be 1 nm in radius, in which case it is unlikely that multiple terraces will be present on any surface and the growth will be layer by layer.

For solution growth, the concentration in Region I is relatively high, typical solutions are in the mM regime. The concentration in Region II will depend upon surfactants as well as other factors such as chelation of neutral metal species. In quasi steady-state, the chemical potential change driving force of the metal in solution, Region I (which will be the same as that in Region II) will be small because only weak reductants such as citric acid are used. We should note that for many solvent syntheses of nanoparticles the typical size of 3D nuclei in the initial stage of the reaction is 1–2 nm (e.g. results from *in situ* scattering experiments and kinetic modelling [23, 198–214]); it is straightforward to show that this has to be about the same size as that of the critical radius for a terrace. For completeness, as the reaction proceeds the concentration of the metal in solution drops so the chemical potential driving force will become even smaller, a point we will return to in section 4.3.

Once nucleated, this layer will grow laterally with a rate which will also be influenced by the concentration in Region II. The net result is a velocity for the growth of any given facet v_i which is essentially independent of the particle size (except, perhaps, for very large particles). Fast growing facets will not appear in the final shape, only the slowest growing ones will be present.

This leads to a steady-state or Lyapunov stable solution for a single crystal as the shape S_K given by:

$$S_K = \{x : x \cdot \hat{n} \leq \lambda(t) \nu(\hat{n}) \text{ for all unit vectors } \hat{n}\} \quad (27)$$

I.e. the shape corresponds to the inner envelope of planes normal to

$$h_i(t) = \lambda(t) v_i \quad (28)$$

This is called the ‘kinetic Wulff construction’, and is deceptively similar to the Wulff shape with the difference that growth velocities (v) rather than the surface free-energies (γ) determine the shape. In some cases the shapes may be very similar or identical as indicated in figure 2, but there is no reason that they should be.

A clarification is appropriate on the meaning of the term ‘Lyapunov stable solution’ here. The growth shape of a single nanoparticle is determined by a set of differential equations for each face, plus local fluctuations in the reactants in solution or the arrival of gas phase atoms. This is analogous to water flowing downhill with some friction. While on average the water takes the fastest route downhill, there will be variations about this path. Similarly the kinetic Wulff shapes are the average shapes for many nanoparticles but there will be some

distribution of shapes, similar to the distribution of paths individual water molecules take. This distribution of shapes has a physical meaning in terms of the magnitude of, for instance, fluctuations in the local concentrations. For completeness, there does not have to be stable solutions to a set of differential equations, and one can have unstable solutions where there is no steady-state solution. We are using the term Lyapunov stable solution for the cases where there is a stable solution to which the shapes will tend to converge in the limit as the particles grow infinitely large. Furthermore there does not have to be just one such solution, there can and often are more than one not just for different seeds but even with a single seed type.

Shape control of nanoparticles in most cases occurs via changing the relative growth rates of different faces, a classic example being the formation of Dh rods by suppressing growth of $\{100\}$ facets [215]. While one expects a trend that higher chemisorption energies lead to reduced nucleation rates, it need not be quite that simple; how readily an atom detaches from a complexed state either in a surfactant around the nanoparticle or when on the surface may also be important. It is worth pointing out that surfactants may also change the edge energies, and this could be the rate limiting step; surface energies factor out of the activation energy. We believe that these possibilities merit more attention than they have been paid in the existing nanoparticle literature.

Every different thermodynamic Wulff construction mentioned in the previous section has a corresponding kinetic Wulff shape. However, before proceeding further one other term needs to be included.

4.1. Kinetic enhancement at certain sites

In addition to flat surface, many particles contain twins and the thermodynamic shape has re-entrant surfaces. This leads to an important additional term with enhanced growth at the twin, a well-established effect (e.g. [216–221]). As shown in figure 28, atoms adding to a re-entrant twin bridge across the twin boundary so have more bonds to the substrate. From density functional calculations it is easy to show that the edge energy for a line of atoms at a twin is essentially zero [67]. Reformulating the nucleation problem of equation (19) for a semicircle similar to Gamalski *et al* [222] yields

$$E = \frac{1}{2} \pi R^2 \Delta\mu N_S + \pi R \gamma_e N_E \quad (29)$$

which has the same critical radius and half the nucleation barrier as shown schematically in figure 27. This leads to an effective enhancement factor for the growth of facets which are re-entrant in the thermodynamic shape, so in general they will not appear. (The exception would be if there is preferential chemisorption of species at the twin boundary, which is distinctly possible.) The importance of twins in the growth of shape controlled nanoparticles was discussed in some depth by Lofton and Sigmung [221], although it appears that they were unaware of some of the earlier work on the thermodynamic shapes and the disclination strain field.

For the specific case of MTPs, there is also a disclination along the five-fold axis. It is well established that there can

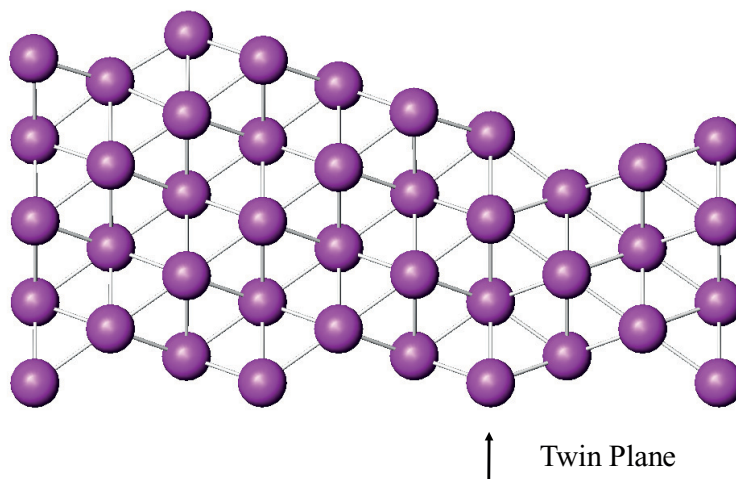


Figure 28. Explanation of enhanced growth at a re-entrant twin. The atoms in a terrace that terminates at the twin place can bond to those on the other side, so the effective line energy is almost zero.

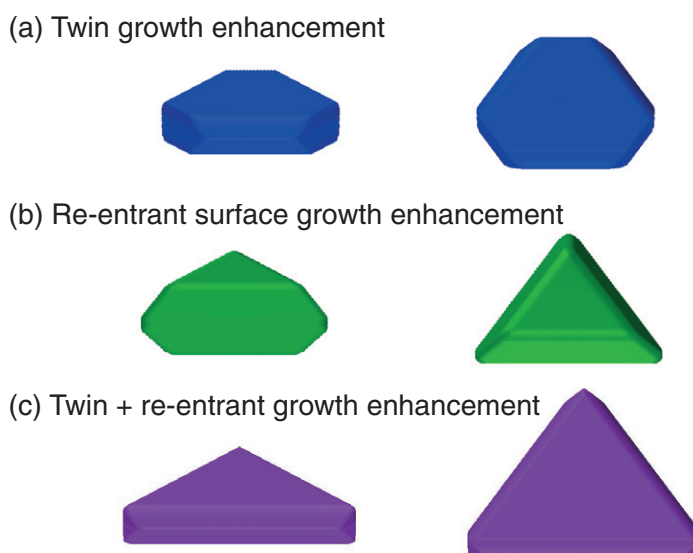


Figure 29. Kinetic shapes for a LTP. In (a) with just enhanced growth at the twin one has hexagonal platelets, in (b) with faster growth at the re-entrant surface truncated triangular bipyramids and in (c) with both triangular platelets. In all cases on the left is a side view, on the right a view down [111].

be faster growth at a screw dislocation; it is possible that the same occurs at the disclination although to our knowledge there are no specific calculations of this in the literature so this is currently just a reasonable hypothesis.

Every thermodynamic variant of the Wulff construction discussed in section 3 has a kinetic equivalent, including those for twinned particles. Both the thermodynamic and kinetic Wulff shapes as well as the Winterbottom kinetic form have been extensively studied in the literature for single crystals, e.g. [5, 66, 68, 102, 223–238]. In some cases software is available to calculate these shapes, for instance for an isolated nanoparticle or with a support [106]. Combining the kinetic enhancement with the modified Wulff construction for twins [239, 240] leads to a large family of shapes as a function of where the growth is enhanced which are illustrated for just {111} and {100} facets in figure 29 for an LTP with one twin boundary. In figure 29(a)

just twin enhancement will lead to hexagonal platelets; in (b) growth at the re-entrant surface triangular bipyramids and in (c) faster growth at both triangular platelets. Additional shapes are the regular icosahedron as well as the pentagonal bipyramid. While the icosahedron is also the thermodynamically stable shape, as first pointed out by Ino almost fifty years ago the pentagonal bipyramid is not. One of the major successes of this model is that it can correctly predict the formation of these commonly observed particles.

Note that similar to the thermodynamic constructions, these kinetic solutions are completely general. By analogy to the arguments in section 3.3 the growth rate of different types of particles will be determined by the relative growth rate of different angular regions of the stereographic triangle that their surfaces expose. A population of nanoparticles may be dominated by those which grow fastest, rather than by any

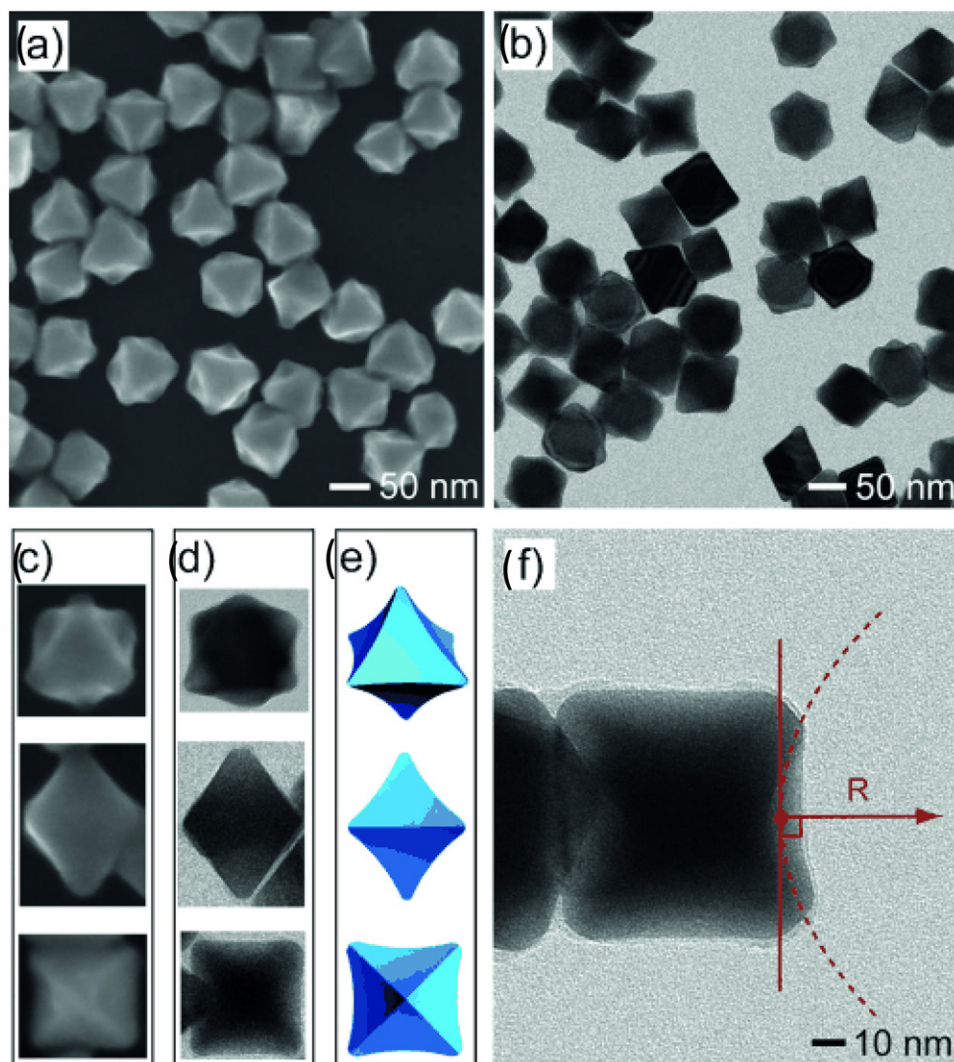


Figure 30. (a) SEM and (b) TEM images of Ag concave octahedrons prepared from Ag cubic seeds using a standard procedure. (c) SEM images, (d) TEM images, and (e) models of a concave octahedron orientated along $[111]$ (top panel) $[110]$, (middle panel), and $[100]$ (bottom panel) directions, respectively. (f) TEM image of a single concave octahedron orientated along $[100]$ direction at a higher magnification. The dash line suggests a concave face with a radius of curvature of R . Reproduced with permission from [241], copyright 2011 J Wiley and Sons.

thermodynamics. There is nothing that says that one type of particle should suddenly stop growing while others do—this would require exchange of atoms between the particles. The only way a particle is likely to change shape is if there is an injection of sufficient energy by some means such as heating or coalescence to provide the activation energy for a transformation. Without this very large MTPs are possible, and occur in practice well beyond any size when they are lower in energy than single crystals.

4.2. Convex shapes: the berg effect and the external solution

All the thermodynamic and kinetic Wulff constructions lead, for each single crystal subunit, to a convex shape, i.e. all the angles are less than 180 degrees. However, in experiment one can grow nanoparticles where part of the surface is concave, see for instance figure 30 [241] for concave silver octahedrons.

One explanation for this is the Berg Effect [194, 242]. In this the local concentration at the corners is higher than

at the center of a facet, which can lead to self-similar shapes that are not convex. There has been some recent more mathematical analysis of this which implies that it depends upon a relatively fragile balance of the different growth terms [243]. This is a little inconsistent with most experiments—although there may be cases where it will occur one would not expect it to be a stable solution and instead be unstable leading to diffusion controlled growth of more complex shapes.

There is another explanation which does not seem to have appeared in the literature for discrete nanoparticles although it has been analyzed in some detail for a slightly different case [236–238, 244]. In the kinetic Wulff shapes the external surface is dominated by the slowest growing surfaces, which are moving away from a common Wulff point. During coalescence of nanoparticles and voids there is growth in towards a Wulff point as illustrated in figure 31 [238]. The kinetic shape of the void is determined by the fastest growing facet, as the velocity is negative. The void is convex, the surface of the crystalline material is concave, and the Wulff point is outside the crystal.

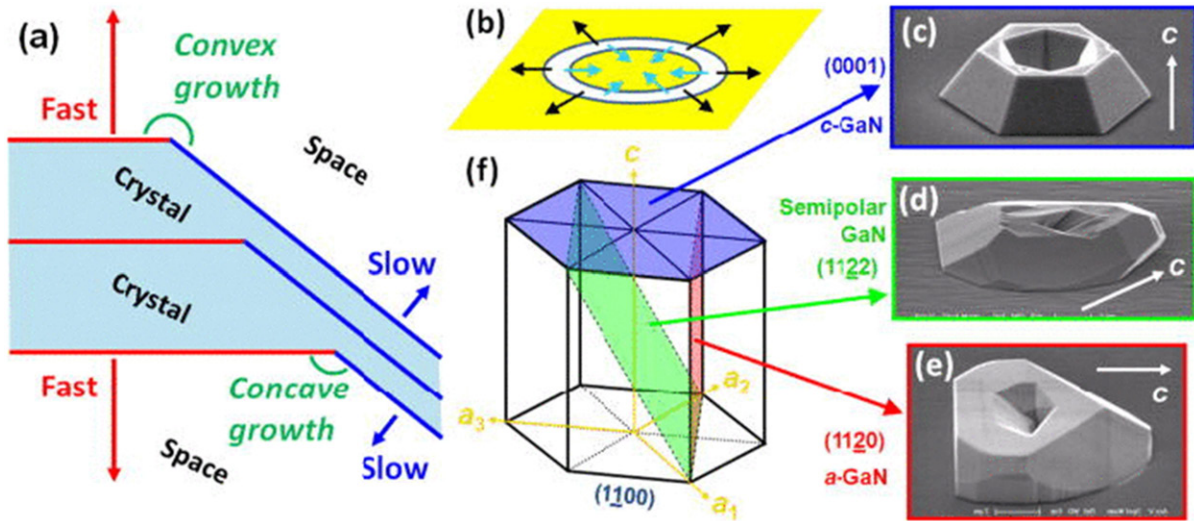


Figure 31. (a) Schematic diagram showing the principle of morphological evolution for convex (toward the upper right) and concave (toward the lower left) growth fronts. The convex growth front will be dominated by the slow-growing facets while the concave growth front by the fast-growing facets. (b) Schematic of an annular ring opening, which produces both inward concave and outward convex growth fronts. SEM images of GaN SAG mesas grown out of an annular ring opening on (c) *c*-plane (0001), (d) semipolar (112̄2), and (e) nonpolar *a*-plane (112̄0) GaN surfaces. (f) Schematic hexagonal lattice showing the *c*-plane (0001), nonpolar *a*-plane (112̄0), and semipolar (112̄2). Reproduced with permission from [238], copyright 2011 AIP Publishing LLC.

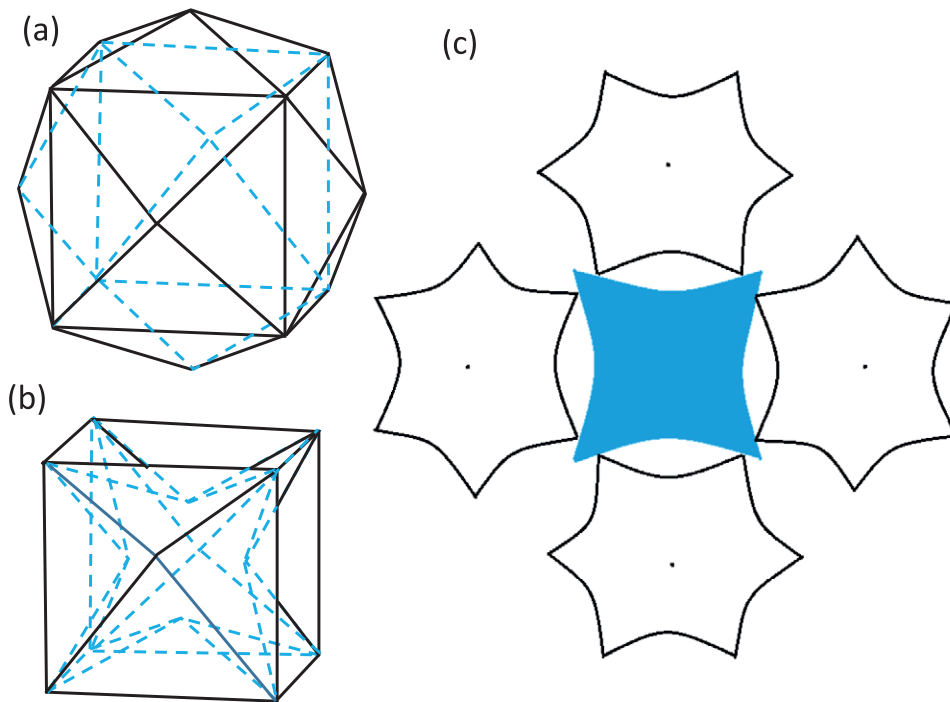


Figure 32. Illustration for a cubic material if {210} growth dominates, in (a) for the external kinetic Wulff, in (b) for the internal kinetic Wulff with also {210} facets in (c) the exterior Wulff centers for the structure shown for (b), a slice through the central plane.

It is possible that for some set of directions, instead of having the Wulff point inside the crystal it lies outside, and there are a set of such external Wulff points for all angles or some combination of external and internal Wulff points. One case illustrated in figure 32, which shows schematically in (a) the external (convex) Wulff solution for just {210} facets and in (b), the concave structure from six external Wulff points of which four are shown in (c). Note that similar to the re-entrant twin case, it will be easier to nucleate a new layer at

the concave vertex. Hence this shape may grow faster than the one with a convex external shape. There is evidence for this type of morphology both for single crystals as well as MTPs, see for instance figure 33 for Dh taken from [245] and also references [246–253]. We strongly suspect that many cases where the Berg Effect has been invoked to explain locally concave shapes may instead be this second class of solutions. For completeness, whether these are true locally stable solutions or just metastable ones requires more study, although

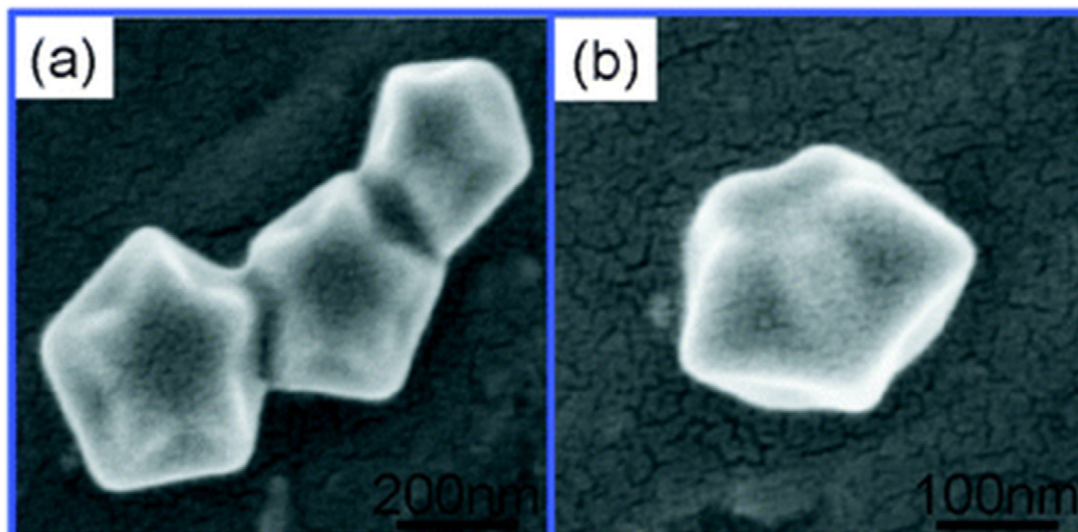


Figure 33. SEM images of Decahedral MTPs with slightly different concave surfaces rather than $\{111\}$ facets. Reproduced with permission from [245], copyright 2012 Royal Society of Chemistry.

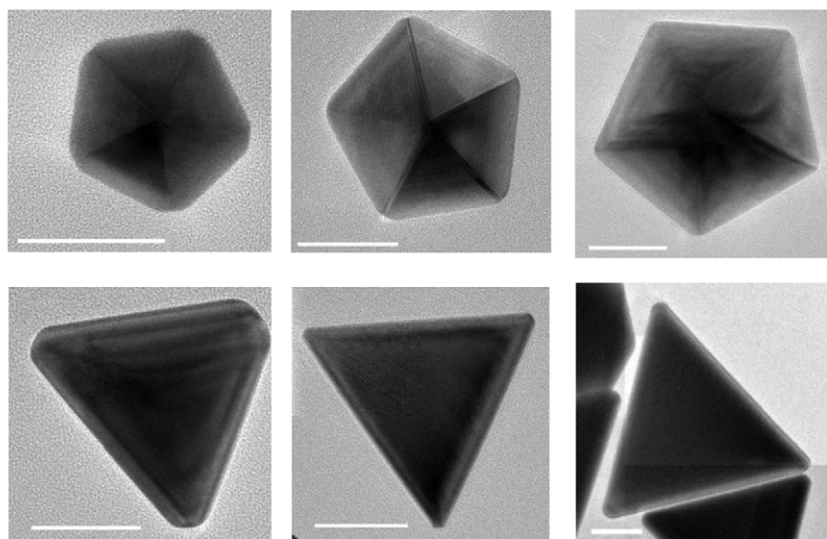


Figure 34. Top row, Dh with rounder corners and bottom row, truncated bipyramids. In all cases the scale bars are 50 nm. The radius of curvature is approximately independent of the nanoparticle size. Other images in this manuscript and the literature also show rounding, although very little attention has been paid to it so far.

we suspect that with enhanced growth at the re-entrant corner they will be locally stable.

4.3. Other cases: symmetry breaking, corner rounding and friends

The external and internal kinetic-Wulff solutions are both Lyapunov stable although the internal may transition to the external case. The full Wulff construction in all cases will have the crystallographic symmetry of the material of interest, but the nanoparticle does not have to—this is not a necessary condition for a stable solution. For instance, if one starts with a seed which has a tetrahedral shape it can continue to grow as a tetrahedron even for a crystal structure which has inversion symmetry. This rationalizes the observation of tetrahedral in

some syntheses, although we acknowledge that there are some subtle issues with the stability of such growth which merits further mathematical analysis.

A related issue arises at the edges and corners since, as mentioned in section 2 the chemical potential can be nominally singular. Experimental measurements indicate that corners are not necessarily sharp, and can be rounded with a local radius of curvature which is independent of the size of the nanoparticles except at very small sizes [67], see figure 34 as well as many of the other figures in this review and in the literature. The explanation of this is that for very sharp corners the local chemical potential would be greater than that of the atoms in the solution used to grow the nanoparticles, so they cannot occur. In addition, at very small sizes it will not be possible to nucleate a new ledge on a small facet as there

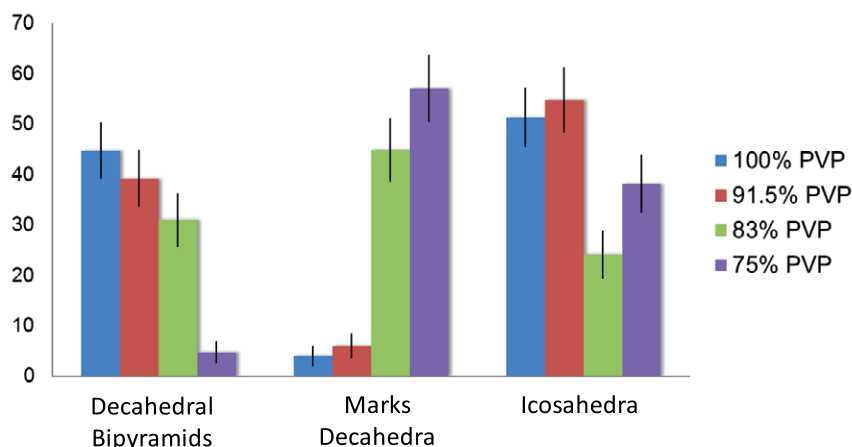


Figure 35. Relative populations of different MTPs indicating a transition from pentagonal bipyramids to Marks decahedra at lower PVP concentrations.

is insufficient area. Instead a steady-state solution will only be possible for a shape which already has steps where atoms can add, i.e. a locally rounded corner or edge with a radius of curvature which is about the same as that of a 3D critical nucleus. As mentioned at the beginning of section 4, towards the end of an aqueous synthesis the critical radius for a terrace and a 3D nucleus will be somewhat large, hence the rounding can be quite large as shown in figure 34. More attention to the experimental shapes of corners and edges in the future would be informative.

4.4. Mixed growth

The thermodynamic and kinetic Wulff constructions are the limits of very fast and very slow exchange of atoms between different surfaces respectively. Since the exchange of atoms depends upon the difference in the weighted mean curvature, in the presence of some exchange an approximate solution will be:

$$h_i(t) \approx \lambda(t)v_i + \zeta(t)wmc(h_i) \approx \lambda(t)v_i + \eta(t)\bar{\gamma}_i \quad (30)$$

Where the vector of weighted mean curvatures and weighted surface free energies have been defined earlier, and $\zeta(t)$ and $\eta(t)$ are scalar functions of the time. These shapes would then be a mixture of the two classes of Wulff constructions. One probable example of this is shown in figure 35 for Pd nanoparticles grown in PVP using citric acid as a reductant where there is a transition from sharp decahedral bipyramids (kinetic control) at higher concentrations of PVP to ones with re-entrant surfaces (thermodynamic control) at lower concentrations [254]. To what extent this is a general phenomenon is unclear since it is often hard to generate from nanoparticle synthesis parameters and reported experimental data the relative role of kinetics and thermodynamics—more work is needed. The same conclusions holds for hydrothermal growth which we suspect is often under mixed control rather than either alone.

5. Strain in MTPs

5.1. General character of the strain in MTPs

As illustrated in figure 36, MTPs are not space filling but have a 2D angular gap for the Dh and ten of these for the Ic. They have to be deformed by ~2% for the Dh and ~6% for the Ic to form space-filling structures. In the original paper by Ino it was proposed that this was an inhomogeneous strain although for simplicity a simple homogeneous strain was used in the first energy calculations [41]. Apparently unaware of this work, de Wit pointed out that the Dh was an example of a disclination [255] which was approximately extended to three dimensions by Yoffe (described in [64]) for an Ic. More complex analytical solutions have also been given by the group of Romanov and co-workers [4, 256–265] and numerical solutions using finite element methods have also appeared [266–268], as well as comparable inhomogeneous strains in larger scale molecular dynamics calculations [269] and earlier atomistic papers [59].

A brief digression is useful to explain the strain in these particles. The standard approach is to consider these via the displacements $u_x(r)$, $u_y(r)$, $u_z(r)$, along the x , y , z axes respectively, all functions of position r . The strain tensor $e_{ij}(r)$ then correspond to the derivatives of these with respect to x , y , z , i.e. the three normal strains

$$e_{xx}(r) = \left. \frac{\partial u_x(r)}{\partial x} \right|; e_{yy}(r) = \left. \frac{\partial u_y(r)}{\partial y} \right|; e_{zz}(r) = \left. \frac{\partial u_z(r)}{\partial z} \right| \quad (31)$$

and the three shear strains

$$\begin{aligned} e_{xy}(r) &= \left. \frac{\partial u_x(r)}{\partial y} \right| + \left. \frac{\partial u_y(r)}{\partial x} \right|; e_{yz}(r) = \left. \frac{\partial u_y(r)}{\partial z} \right| + \left. \frac{\partial u_z(r)}{\partial y} \right|; \\ e_{zx}(r) &= \left. \frac{\partial u_z(r)}{\partial x} \right| + \left. \frac{\partial u_x(r)}{\partial z} \right| \end{aligned} \quad (32)$$

Less commonly used are the rotations, which are defined as

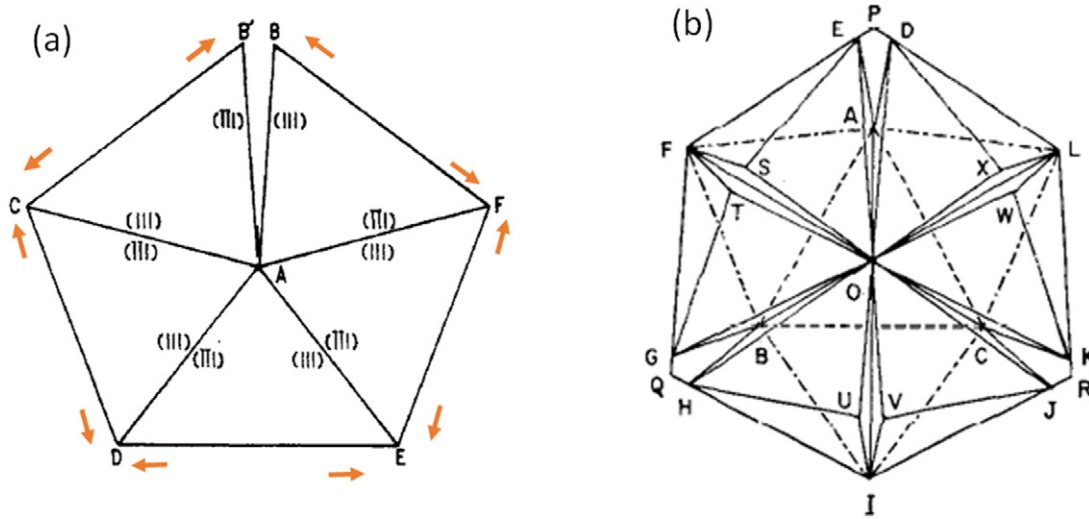


Figure 36. Illustration of the angular gaps in a Dh (a) and an Ic (b), adapted from the original work of Ino and Ogawa. Reproduced with permission from [40], copyright (1967), Vol.22, No.6, 1365–1374, Ino S and Ogawa S, Journal of Physical Society of Japan.

$$\begin{aligned} \omega_x(r) &= \frac{\partial u_y(r)}{\partial z} - \frac{\partial u_z(r)}{\partial y}; \quad \omega_y(r) = \frac{\partial u_z(r)}{\partial x} - \frac{\partial u_x(r)}{\partial z}; \\ \omega_z(r) &= \frac{\partial u_x(r)}{\partial y} - \frac{\partial u_y(r)}{\partial x} \end{aligned} \quad (33)$$

Ino analyzed the strain in a Dh and Ic using the normal and shear strains only and taking these as constants; he was aware that this was an approximation which gave results for the strain energy larger than the true energy. De Wit assumed that the Dh was cylindrical, then described the deformation in cylindrical polar co-ordinates ρ, ϕ, z using a rotation $\omega_z(r)$ and a radial normal strain $e_{\rho\rho}(r)$. This leads to the displacements

$$u_r(r) = \left[\frac{1 - 2\nu}{2(1 - \nu)} \right] \epsilon_D \rho \ln(\rho/R) - \epsilon_D \rho / 2 \quad (34)$$

$$u_\phi(r) = \rho \epsilon_D \quad (35)$$

and a cubic dilatation, the local volume change of

$$\Delta(r) = \left[\frac{1 - 2\nu}{2(1 - \nu)} \right] \epsilon_D (2 \ln(\rho/R) + 1) \quad (36)$$

with stresses

$$\sigma_{rr} = 2G\epsilon_D \ln(\rho/R) \quad (37)$$

$$\sigma_{\phi\phi} = \frac{G\epsilon_D}{(1 - \nu)} [\ln(\rho/R) + 1] \quad (38)$$

and G the shear modulus, R the particle radius and ν Poisson's ratio. At the outermost surface there is an expansion ($\Delta(r) > 0$), in the center a compression with no overall change in the volume. Compared to the simpler homogeneous strain approach, the energy to close the angular gaps is about a factor of two smaller. The same general conclusions apply to the Ic which can be considered as a number of disclinations, one for each five-fold axis, leading to a total strain energy which is about twenty times that of the Dh.

Both the homogeneous strain approach of Ino and the cylinder of de Wit are approximations. In general with a more complex shape there will be a combination of both rotational and other strains to remove the angular gaps.

Going beyond these simpler approaches by analytical methods for the more complex shapes found experimentally is somewhat intractable, but can be done numerically using finite element methods. An important point was made by Johnson *et al* [266] that one has to take account of elastic anisotropy, which is large in metals such as silver or gold. In addition to this simple approximations of a cylinder or a sphere for nanoparticles are pragmatic but not accurate. An example of more general results for the stresses [267] is shown in figure 37, with more accurate models for the external shape. The figure shows both the Von Mises stress, which is an indicator of how likely it is for dislocations to form as well as the strain energy density for a sharp Dh and one with $\{111\}$ notches, with regions where these are large indicated. For the sharper Dh there are higher stress and energy densities in the center of the segments whereas they are both much closer to constant when notches are introduced as this leads to a shape closer to a circle in projection and the de Wit disclination result. For the Ic with the simplest perfect icosahedron shape there are also noticeable local variations with stress concentration in the center of the segments as shown in figure 38.

There are also variations in the strain with the external shape of the particle. For instance as shown in figure 39 via the Airy stress function, with long rods in the center the strain converges towards the de Wit solution, differing at the ends. This could be experimentally measured, although we are not aware that it has been done as yet. Because of the change with shape there will also be energy differences and a coupling, at least in principle, of the thermodynamic shape and the strain as shown in figure 40. As a broad generalization, the strain energy density is smallest for the shapes with only $\{111\}$ facets, and is larger when the aspect ratio increases. In the spirit of predictive models, a brief explanation of this is relevant.

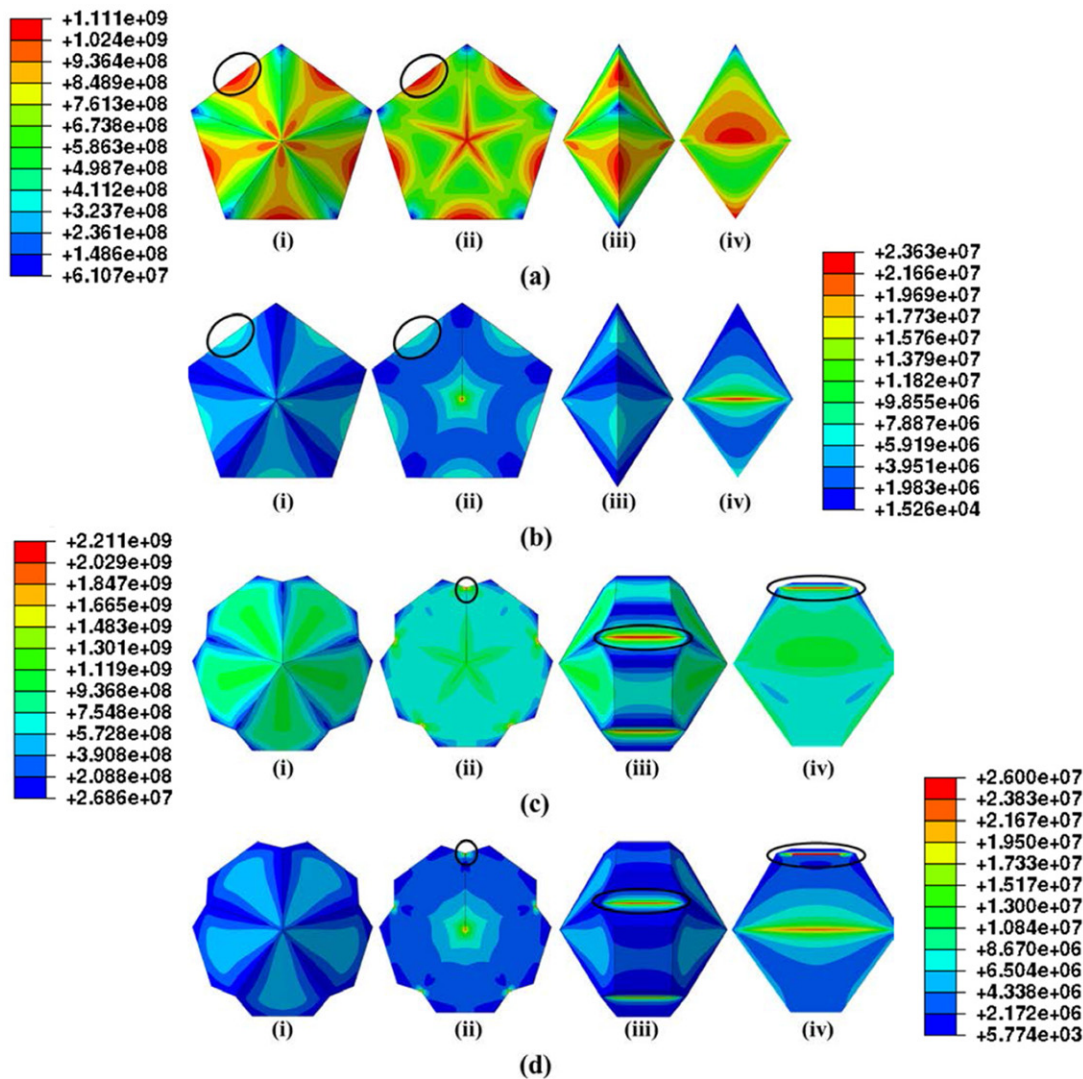


Figure 37. In (a) and (c) the Von Mises stresses and in (b) and (d) the strain energy density. In (a) and (b) a pentagonal bipyramid is used, in (c) and (d) the thermodynamic shape. Regions of high stress and strain energy density are indicated, and change with the 3D shape of the particles.

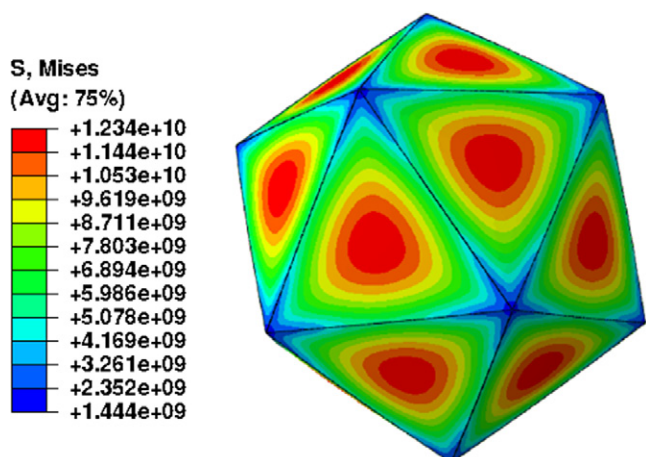


Figure 38. Plot of the Von Mises stresses at the surface of an Ic.

The total strain energy can be calculated via either an integral over the total volume, or by integrating the forces on the angular gaps needed to close them and the distance moved. Using

the later, the total energy will be smaller the larger the notches are, i.e. the smaller the total twin boundary area is.

There can also be a coupling between the strain and the surface structure; as shown in figure 41. In these experimental results the reconstruction on the (100) surface of a silicon Dh is slightly different due to the strain field as evidenced by direct *in situ* growth [270]. As a caveat, we do not expect this to dominate the growth of nanoparticles in general, but there might be special cases.

5.2. Alternatives to inhomogeneous strain

An alternative approach to an elastic strain which was first described by Bagley [271] and developed further by Yang *et al* [272] describes MTPs as body-centered orthorhombic (Dh) or rhombohedral (Ic) units. The later work was based upon analyses of electron diffraction patterns, an approach recently re-emerging in an x-ray diffraction analysis [269]. Unfortunately these analyses contains an error in interpretation that has propagated in the literature.

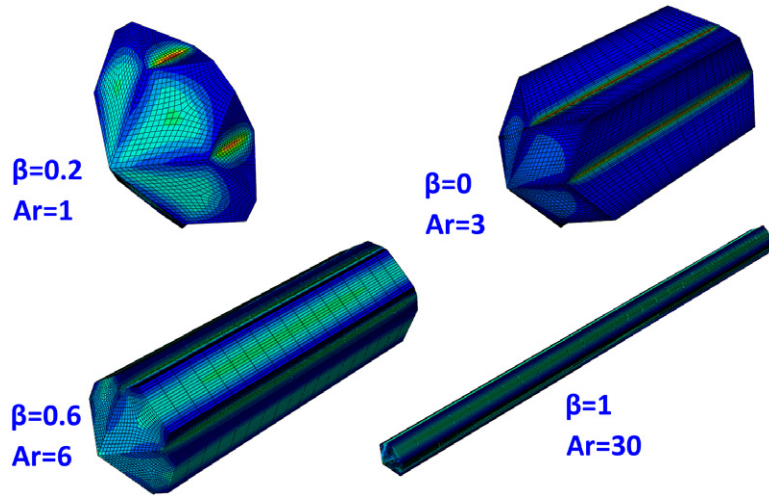


Figure 39. The Airy stress at the surface of a Dh for several different amounts of $\{100\}$ surface via the parameter β defined earlier for a number of different aspect ratios Ar.

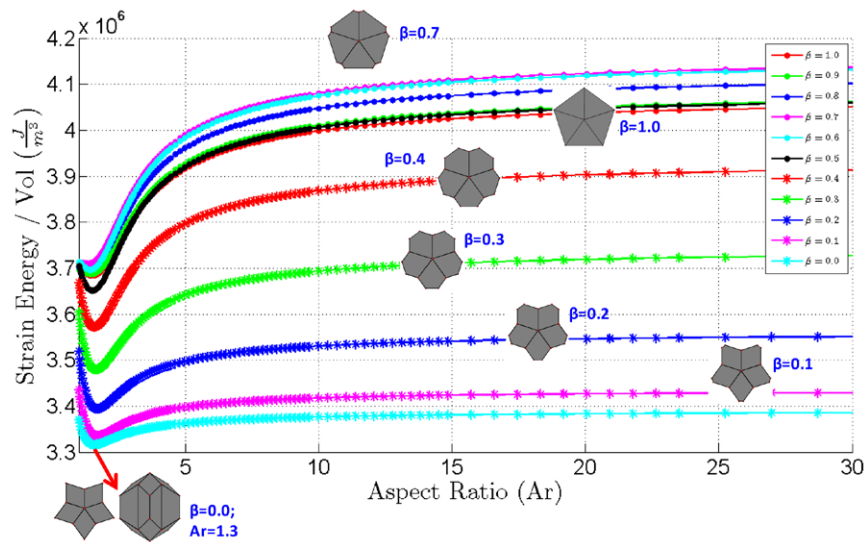


Figure 40. Plot of the strain energy density versus aspect ratio for different magnitudes of the amount of $\{100\}$ surface, the β parameter defined earlier in the text.

For any material with an inhomogeneous strain field, the strains and rotations as a function of position $e_{ij}(r)$ can be expanded as a Taylor series about any point as:

$$e_{ij}(r) = \bar{e}_{ij} + \mathbf{r} \cdot \nabla e_{ij}(r - r_0) + \dots \quad (39)$$

The first terms are the homogeneous strains and rotations, the next ones the inhomogeneous terms. Any diffraction experiment using electrons, x-rays or other radiation only measures the average value over the volume of the illuminated region (unless inversions of coherent diffraction is done as discussed in section 3.4.3 and shown in figure 24). In general the inhomogeneous components vary both in magnitude and sign from point to point, so the leading term is always the homogeneous component. Even with images using modern aberration-corrected electron microscopes the homogeneous term can dominate as there is an implicit integration along the beam direction. It is completely correct to state that the *average* structure is not fcc, but implying that this is more than the

average homogeneous distortion implies a phase transition to a new structure at small sizes. There is no evidence for such a phase transition in the simple fcc metals.

To test accurately the strain field requires use of local imaging methods to analyze the higher-order terms directly. Probably the most sensitive technique is dark-field imaging. If the strain is completely homogeneous, the contrast in the image depends only upon the thickness and the orientation of each single-crystalline region; if not it will vary with position. Even in the early dark field images it was apparent that the contrast varied strongly with position as discussed in [273]; to our knowledge every published dark-field image shows this, see for instance figure 42 from [15]. A similar test is to take local diffraction patterns using a small electron probe, which shows local changes in intensity also an indicator of inhomogeneous strains [274]. The strains can also be seen from careful examination of high-resolution electron microscope images (e.g. [266, 275–277].), or via x-ray diffraction methods [278].

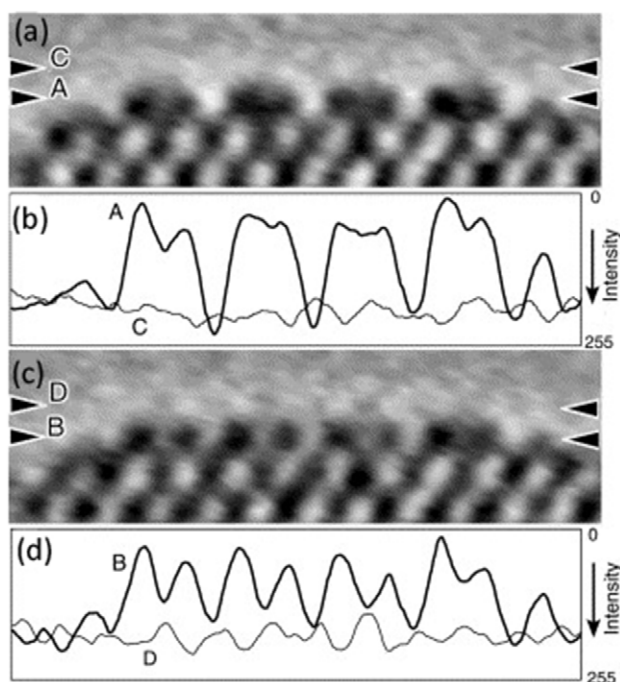


Figure 41. HREM images during growth on the (100) surface of a silicon Dh. The images (a) and (c) are at different times, with (b) and (d) corresponding line traces. There is a breaking of symmetry which it was suggested was due to the anisotropy of the stresses. Reproduced with permission from [270], copyright 2001 Elsevier.

With these caveats about the fine details, the overwhelming preponderance of experimental data supports inhomogeneous strains. Measurements for both smaller and larger particles are all close to what would be expected.

One additional item for discussion is the question of whether there is some accommodation of the strain at the twin boundaries. In some recent experimental work [266] there was evidence that the net rotational component of the strain field did not add up to the required 7.35 degrees, but was substantially less. Other measurements with a Marks decahedron gave different results [275] with the rotation larger than expected. Less than the full rotation was interpreted as an indication that some of the strains are accommodated at the twin boundaries. However, we believe this is an over interpretation. Similar to the discussion above about inhomogeneous versus homogeneous strain, the total strain field can be split into a non-rotational component and a rotational component. How large the rotational component is will depend upon the anisotropy of the elastic constants and also the external surface. The total angular gap per segment is 1.47 degrees, but as illustrated in figure 43, the rotational component for silver which has an anisotropy ratio of 3.0 ranges from 0.90–1.16 degrees total depending upon position, whereas for aluminum which is close to isotropic (anisotropy ratio of 1.22) the rotational is 1.3–1.47 degrees. It is worth mentioning that there is also an ambiguity in the exact lattice in the experiments which will lead to some uncertainties in the measurements—only the average of the center of the particles can be measured which is already a strained value. Furthermore the experiments mentioned above are projections along the beam direction, and as the earlier figures show there are 3D variations.

While there may well be a small component of strain accommodation at the boundaries, whether this exists and how well the elasticity models in three dimensions match experiment is a topic for future work. Transmission electron microscopes continue to improve, so picometer accurate measurements of positions in three dimensions may be possible in the not too distant future.

5.3. Stress relief mechanisms

The total strain energy in MTPs scales as the volume. When the particles become large enough the total energy stored in the strain will become sufficient to nucleate stress-relieving dislocations. For instance, the total energy for a low-angle grain boundary will scale as the volume to the two-thirds power, so this will be energetically favored at larger sizes.

The Dh particles are much easier to image, so more is known about them. Earlier results on stress relaxation can be found in [2], with a detailed experimental analysis by Iijima for larger silicon Dh [279]. A rather comprehensive analysis of the possible stress relaxation modes has been presented by Romanov and collaborators [4, 256–261, 263–265], with a recent example illustrating them shown in figure 44. There are many possibilities, and in a few cases there have been direct observations, for instance splitting of the disclination via the introduction of stacking faults [280] (figure 44(a)), via a tetrahedral stacking fault (reproduced with permission from [281] (figure 44(b)) or via formation of a grain boundary [279] (figure 44(c)). Not all the possibilities have been experimentally observed as yet, but overall the theoretical models appear to be reasonably well supported by experimental evidence. For the Ic particles while dislocations were observed some time ago [64, 274] more work is needed to unravel the stress-relief mechanism, which is not trivial as they are less accessible to electron microscope imaging due to overlap of the different segments along the beam direction.

An alternative to stress relief by dislocations or splitting of the disclination is via point defects or segregation in alloys—in an alloy there are additional degree of relaxation channels not present in a fixed composition material. A continuum based model of segregation indicates [282] that the problem can be mapped onto one of the distribution of impurities around a dislocation. The results indicate that while the change in free energy may be small, there will be a noticeable segregation of larger atoms to the external surface and smaller ones to the core of the disclinations as shown in figure 46. While there is some experimental evidence for this (see [282]), to date it is not fully conclusive and more work would be informative.

A somewhat similar process where there is stress relief in phase separated materials has recently been revealed in atomistic calculations for much smaller sizes by Ferrando [283, 284]. As illustrated in figure 49 [284], for small icosahedral clusters where the phase separation is not radially symmetric but can be off to one side. In effect the local expansion of the lattice for larger unit cell material can assist in closing the gaps.

A third mechanism that can occur in certain cases is anisotropy of ordering to partially relieve some of the stresses. This

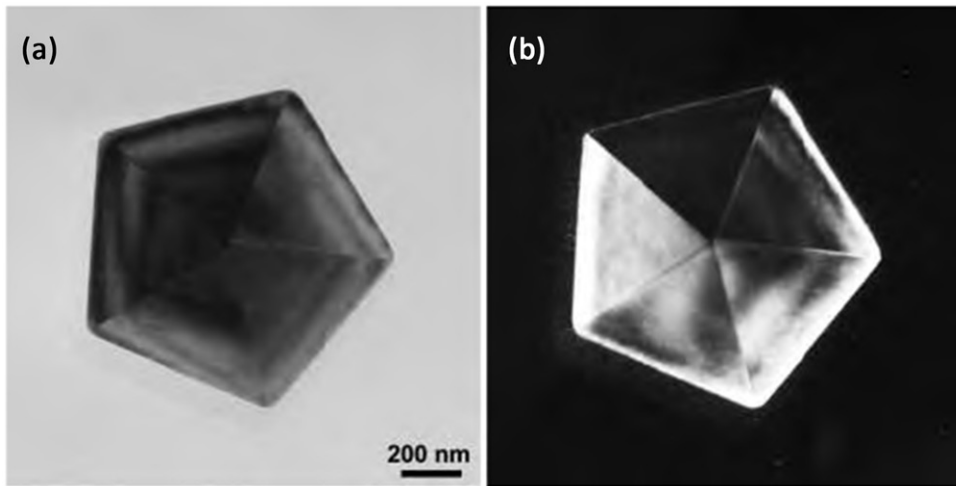


Figure 42. In (a) bright field and in (b) dark field image of a Dh, reproduced with permission from [15], copyright 2009 de Gruyter. The large intensity variations in (b) are a signature of inhomogeneous strains.

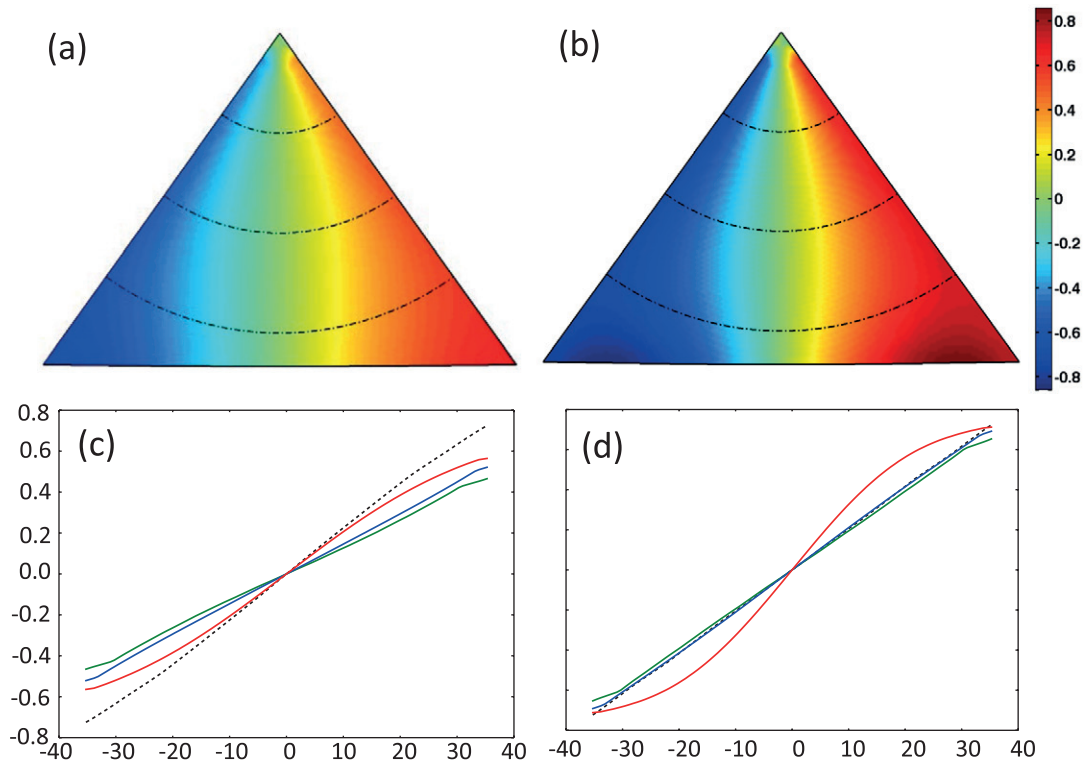


Figure 43. Plot of the rotation ω_z in the central plane of a pentagonal bipyramid for silver of the left and aluminum on the right. In (a) and (b) color coded values are shown, while in (c) and (d) plots at 0.3, 0.6 and 0.9 of the total distance along [001], i.e. vertical in the 2D plots with the angular displacement shown dashed. For silver there are jumps in the rotation due to elastic anisotropy whereas there are none for aluminum. In both cases as the external surface is approached the rotation also changes due to changes in the elastic strains at the surface.

has been observed for FePt nanoparticles [276, 285–287]. There is evidence in this work for Pt segregation to the surface, which we would expect as it is the larger atom. The same segregation of the larger atoms has been observed for CuAu [276], and theoretical analyses have similar conclusions [288].

We suspect that this may be a rather general phenomenon, and the topic of alloy stress relief is worth more experimental probing, and there may be additional mechanisms—although the broad details are in good agreement qualitative with expectations based upon the elastic models.

One different relaxation mechanism merits mention here, as it may be quite general at least for thermodynamic shapes. As analyzed independently by Ajayan *et al* [118, 289, 290] and Romanov *et al* [4, 256–261, 263–265], the strain energy of a decahedron approximated as a cylinder when the dislocation is not in the center by a fractional distance b scales as

$$E = E_{b=0}(1 - b^2)^2 \quad (40)$$

If the disclination moves away from the center, there will be a net gain in the strain energy, at the cost of a increased total

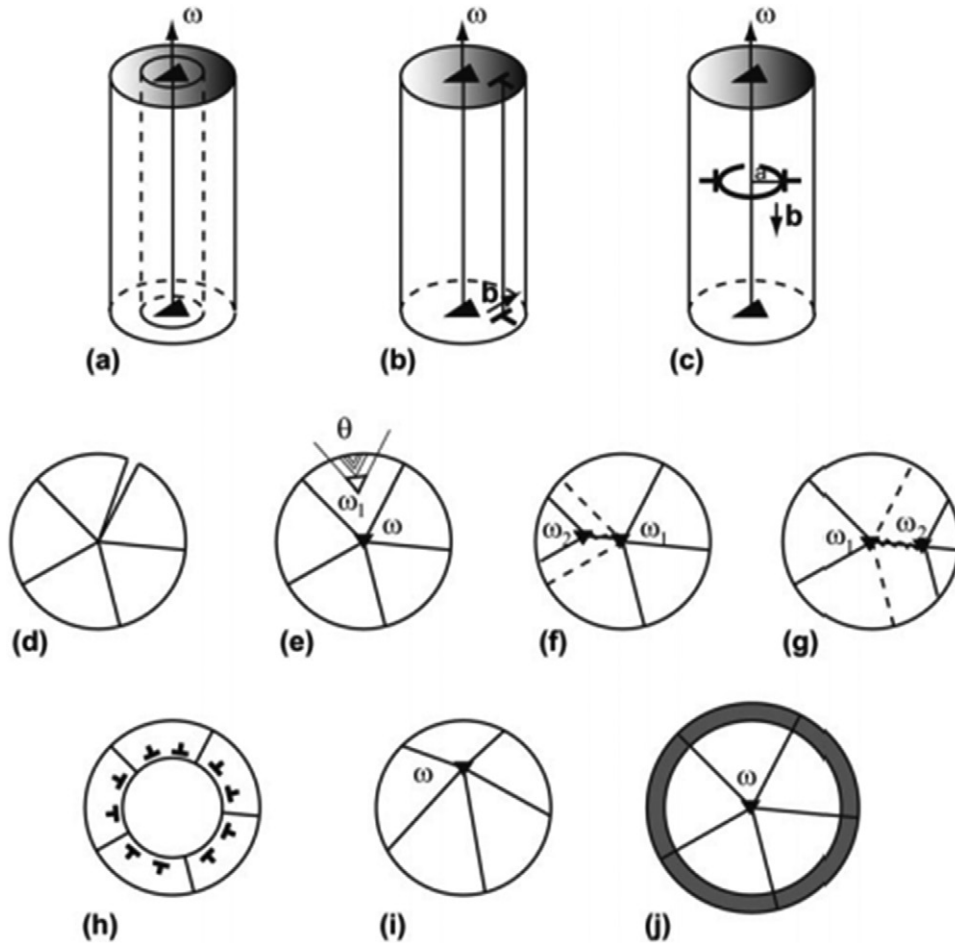


Figure 44. Plausible channels of stress relaxation (a) appearance of a hollow center; (b) formation of the straight-line dislocation; (c) formation of the vacancy-type dislocation loop; (d) formation of a low angle grain boundary (e) addition of a negative disclination with a system of stacking faults; (f, g) different ways of decomposing the disclination χ into two others linked by stacking faults; (h) formation of a region without a disclination; (i) shifting of the pentagonal axis towards the periphery; and (j) the formation of a surface misfit layer having a different orientation to the original crystal. Reproduced with permission from [263], copyright 2011 Cambridge University Press.

surface energy as the different segments are no longer simple modified Wulff shapes. This has been calculated at very small sizes [118, 289, 290], see figure 47. The calculations indicate that at smaller sizes there will be an activation energy barrier for the disclination to move out of the center because of the additional surface energy cost of moving away from the symmetric case. At larger sizes there will be no barrier since the strain energy will dominate. This can drive glide of edge dislocations in to the center as first hypothesized by de Wit, although this needs a fair amount of activation energy, so would only occur at higher temperatures. An alternative is that the growth becomes asymmetric with a smaller deviation from symmetry rather than substantial displacement of the disclination. We have recently obtained experimental evidence that this can occur with extensive evidence for asymmetric Dh in both Pd and Pd-Pt alloys, see figure 48 [254].

6. Energy versus size

The total energy of MTPs, as well as that of other nanoparticles can be written from earlier as

$$E = V \left(\frac{\mu^B}{v_0} + W_D \right) + V \frac{2}{3} (\gamma_{111} \varepsilon_W + \langle g_{ij} e_{ij} \rangle \varepsilon_g) + O(h) \quad (41)$$

When comparing nanoparticles with the same number of atoms the bulk chemical potential cancels out, as do small terms such as those due to changes in the lattice parameter via the surface stress. For simplicity all terms which scale linearly with the size will also be ignored, a safe assumption except at very small size provided Gibbsian definitions are used. It is then simplest to plot $E/V^{2/3}$ as illustrated in figure 50 versus $V^{1/3}$, in the figure for two different values of the surface stress. Note the large changes with the surface stress.

This energy balance yields the lowest enthalpy structures, but by itself is not a complete description of the system. For this one needs to use a statistical mechanics approach, writing the relative fraction of each type of particle in some form for a specific number of atoms such as

$$n_i = \frac{\exp\left(-\frac{\Delta G_i}{kT}\right)}{\sum \exp\left(-\frac{\Delta G_i}{kT}\right)} \quad (42)$$

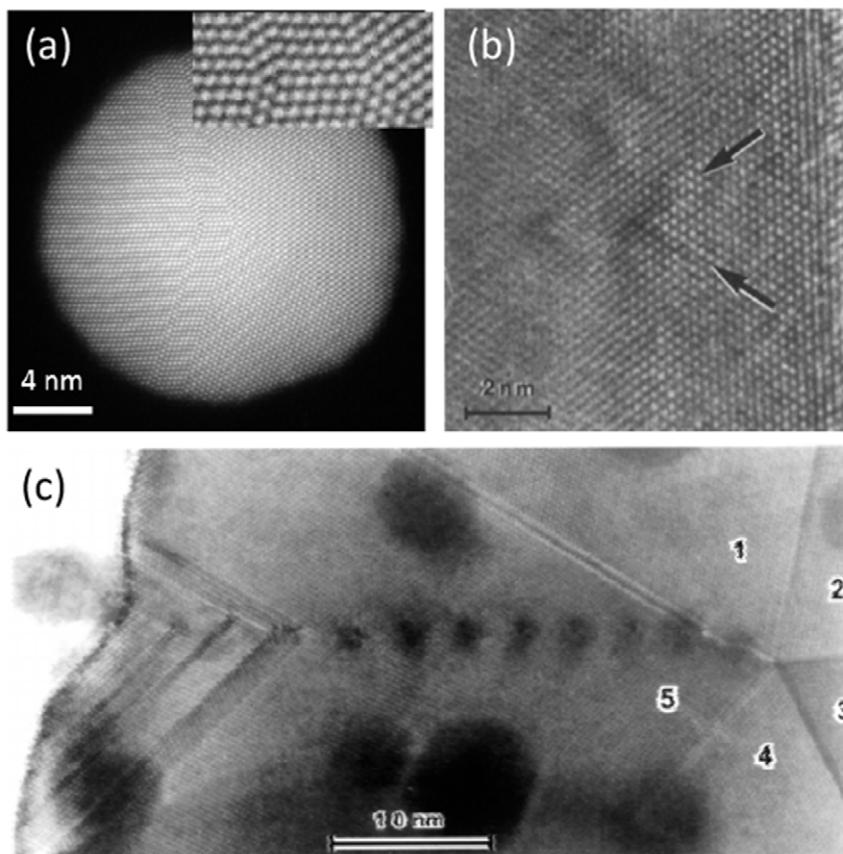


Figure 45. Collation of relaxation images, in (a) via additional disclinations and stacking faults showing a Dh with the split disclination in the center magnified (reproduced with permission from [280], copyright (2015) American Chemical Society, images courtesy of B. Sara and S. Van Tendeloo), in (b) via a tetrahedral stacking fault (reproduced with permission from [281]), and in (c) via formation of a grain boundary (reproduced with permission from [279]), copyright 1987 The Japan Society of Applied Physics.

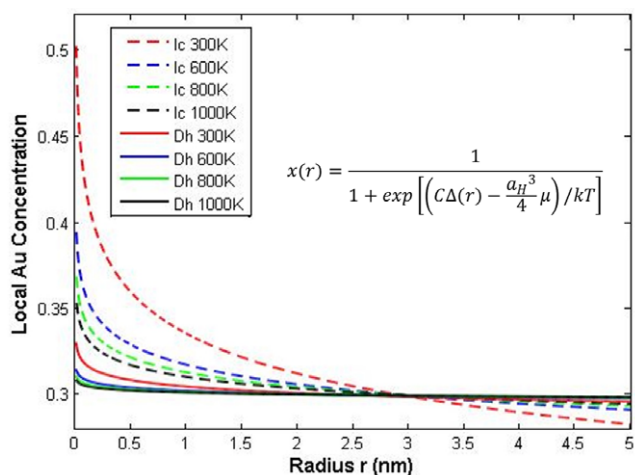


Figure 46. Strain induced segregation in Ag-Au Dh and Ic calculated for different temperatures.

This problem has been well studied (e.g. [8, 291–304].), and while the specific results can vary strongly with potential parameters [8] (see figure 51) the general results are now quite clear. At reasonable temperatures and when the size is small enough, there is no single shape rather a diverse population of shapes. The transitions between the different shapes can occur

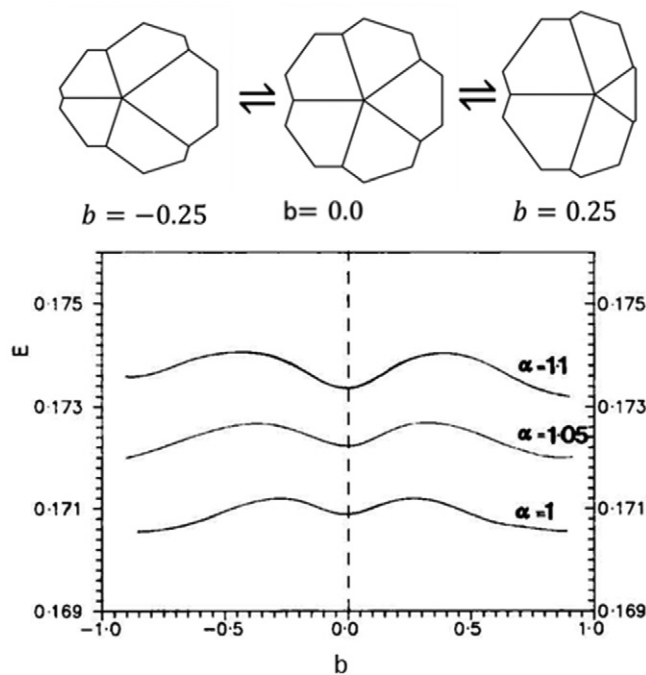


Figure 47. Plot of the energy versus the fractional asymmetry of the disclination including both the surface energy change and the internal strain energy change.

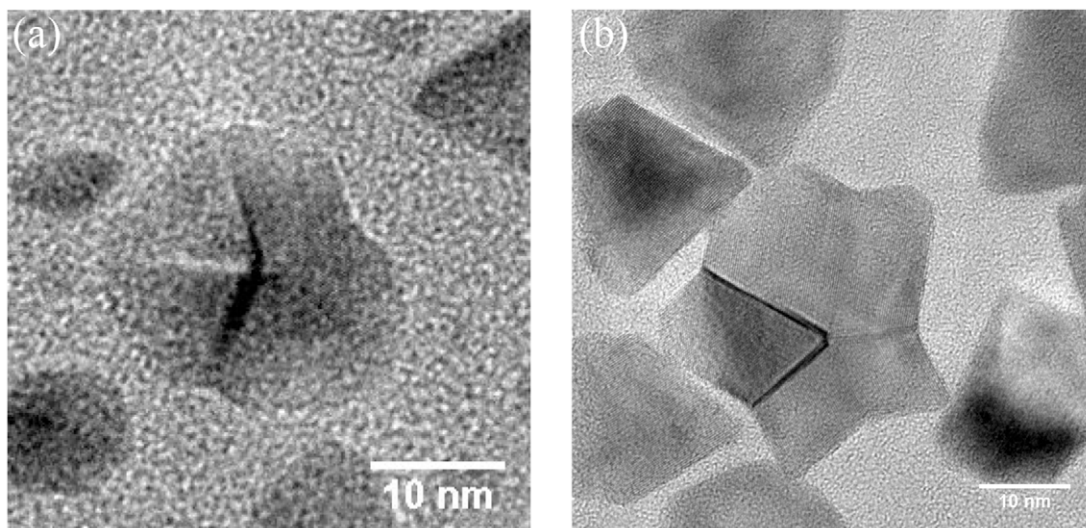


Figure 48. Asymmetric (a) Pd and (b) Pd-Pt alloy Dh nanoparticles [254], courtesy L Peng *et al.* Those shown have only two-fold symmetry.

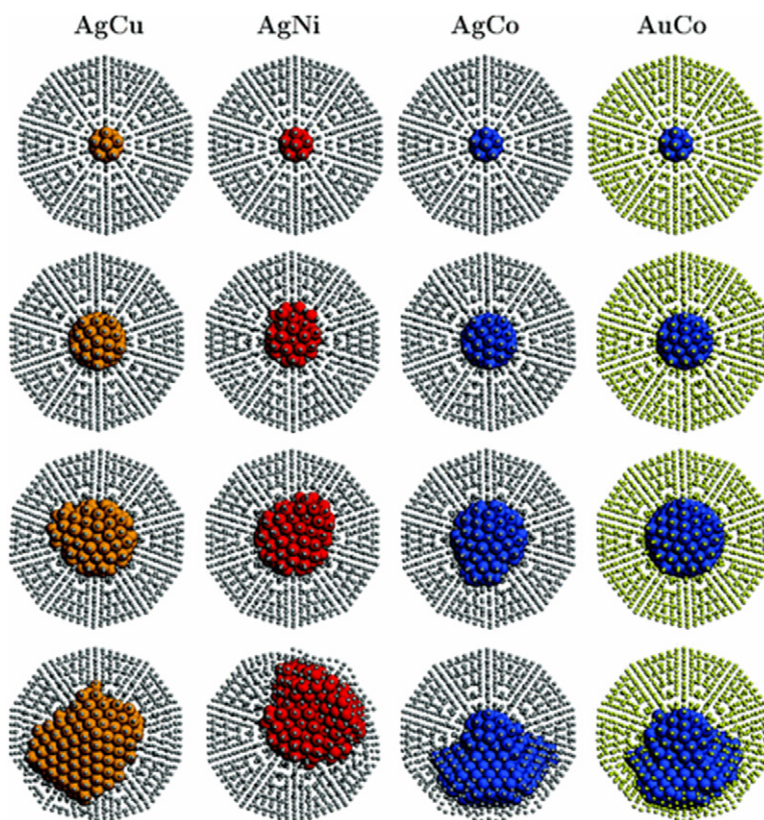


Figure 49. Lowest-energy configurations of icosahedral nanoparticles of fixed size (number of shells $n = 8$, total number of atoms $N = 1415$) for increasing size of the core. From top to bottom. Core of 13 atoms (number of shells $k = 2$), of 55 atoms ($k = 3$), of 147 atoms ($k = 4$), of 309 atoms ($k = 5$). S atoms are shown as small spheres so that C atoms (bigger spheres) are visible. Reproduced with permission from [284], copyright 2013 American Physical Society.

on the millisecond time scale or faster. Even at larger sizes it is possible for particles to transition between one structure and another, either as a consequence of heating, exposure to the electron beam or during growth [292, 305–314], see for instance figure 52 from [313] for an example of a single crystal changing to an Ic and then later to a Dh during an *in situ* heating experiment.

Beyond some size transitions between shapes will become improbably under most experimental conditions, so one has a frozen seed from which a larger particle will grow without changes in structure in most cases. Hence it is not uncommon to find MTPs in the micron size range [315] or in a few cases millimeter sized. Indeed, as pointed out by Hofmeister [34] very large MTPs called fivelings were known back in the

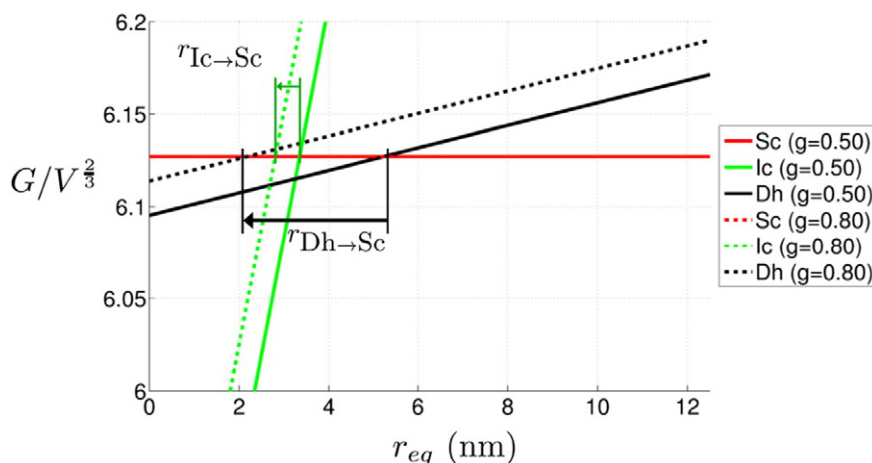


Figure 50. Plot of the free energy divided by the volume to the two-third power, versus the equivalent radius for the volume for two different values of an isotropic surface stress (g). In all cases Ic are stable at smaller sizes, but whether the Dh have an intermediate stability range depends upon the size of the surface stress.

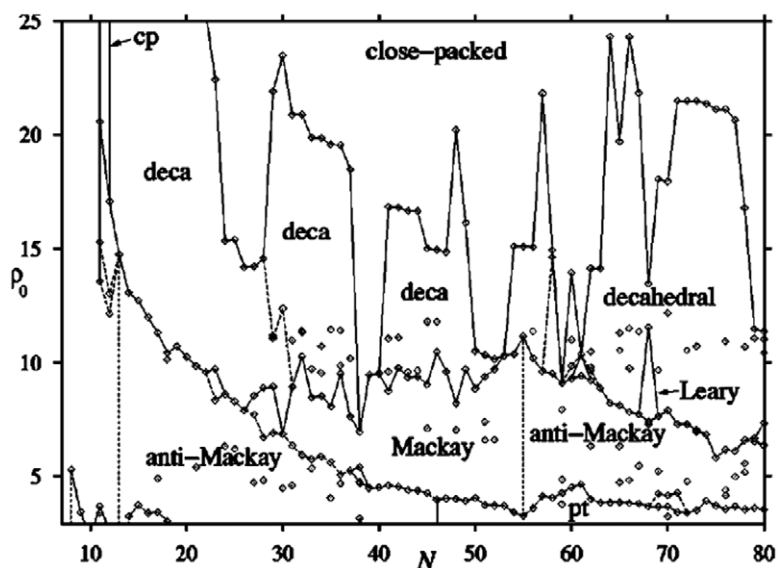


Figure 51. Plot of the lowest energy structures with a Morse potential as a function of parameter ρ_0 , where smaller values correspond to softer potentials which decay more slowly with distance. The large variations with potential are notable. Reproduced with permission from [8], copyright 2005 American Physical Society.

nineteenth century, including Dh with re-entrant surfaces at the twin boundaries. One Urban Myth should be mentioned here and hopefully laid to rest, namely the idea that MTPs occur through the assembly of individual tetrahedral units. This concept was discussed early by, for instance, Gillet [316] who pointed out that it was not reasonable and that layer-by-layer growth as discussed earlier was by far the most reasonable explanation. While there are papers where it has been argued that the experimental evidence supports this concept of sequential assembly of MTPs, a closer examination of all the images in the papers we can find indicates that they are all highly asymmetric Dh particles which we believe have been incorrectly interpreted.

Because the strain energy of the Ic is about twenty times that of the Dh, they only occur at very small sizes; observation of them at larger sizes is common and can only be because kinetics not thermodynamics are controlling. Specific ligands

can stabilize particular structures, and precise details of the atomic structures of a number of very small clusters have been recently determined by x-ray diffraction (e.g. [317–328].), for instance figure 53 shows the Marks decahedron core of $\text{Au}_{102}(\text{p-MBA})_{44}$ [317] and 52b shows the icosahedral structure of $\text{Au}_{144}(\text{SR})_{60}$ [320], both very similar to those found at much larger sizes.

As a function of size and temperature there will be a phase diagram for the thermodynamically most stable shapes as originally hypothesized by Ajayan and Marks [290]. The number of theoretical calculations where aspects of this have been studied is immense, and we will not attempt to review them here. Overall the experimental result [61, 278, 289, 305, 311, 313, 329–335] are qualitatively consistent with this general model. One example [311] is shown in figure 54 for the evolution of the shapes of Cu nanoparticles grown and studied *in situ* on strontium titanate as a function of temperature.

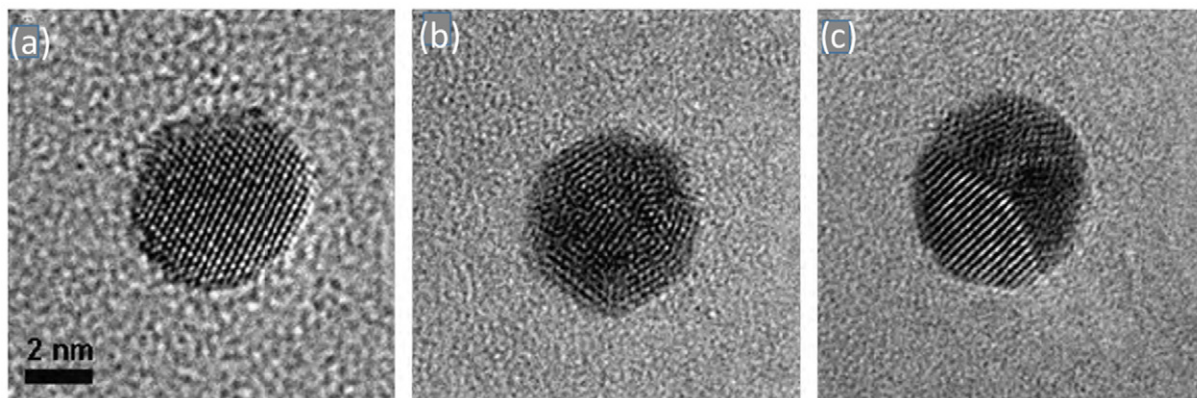


Figure 52. Controlled heating of a 5.5 nm gold particle. (a) The original single crystalline fcc structure, near to a $[110]$ orientation observed at room temperature. (b) At 300 C, the particle structure transforms to an icosahedral structure, oriented near to the $[112]$ projection. (c) Finally a decahedral structure close to $[110]$ is observed at 400 C. Reproduced with permission from [313], copyright 2010 Elsevier.

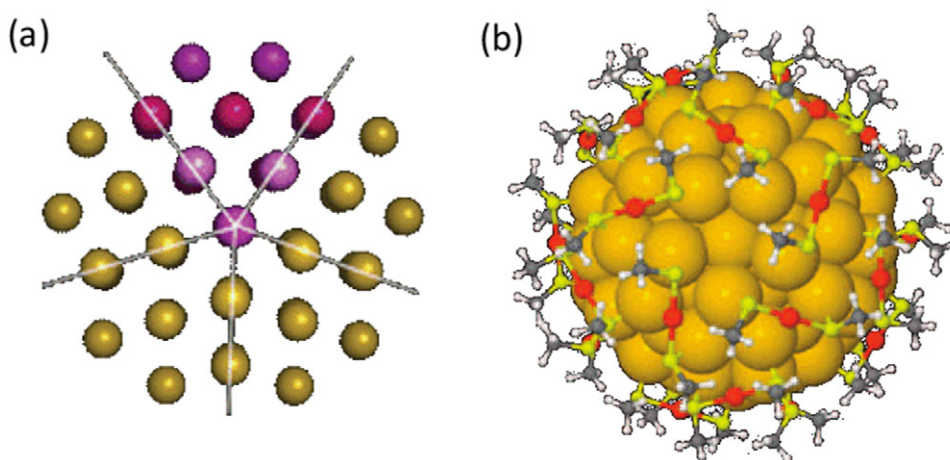


Figure 53. Structure of the Marks decahedron core of $\text{Au}_{102}(\text{p-MBA})_{44}$ in (a) (reproduced with permission from [317], copyright 2007 American Assoc. for the Advancement of Science) and the icosahedral structure of $\text{Au}_{144}(\text{SR})_{60}$ in (b) (reproduced with permission from [320], copyright (2009) American Chemical Society), both viewed down the five-fold axis.

A complication is the surface stress energy term, which has a large environmental dependence and is comparable in magnitude to the differences in the total surface free energies of different shapes. One strategy is to analyze the stability ranges and the cross-over between the different types of MTPs and single crystals with the surface stress and surface free energies allowed to vary as a parameter. This leads to the results shown in figure 55 [268]. A nice illustration of how important the environment can be is shown in figure 56 [336]. Only a few per cent of oxygen is enough to completely change the distribution of gold particles produced by sputtering. This relates to how in solution based syntheses of nanoparticles subtle and sometimes unintentional changes in the materials used can lead to large differences. While the critical role of impurities and chemisorbants has been known for some time [64], they are rarely well controlled in experiments. For future six-sigma nanoparticles more will need to be understood about the details as well as far tighter experimental control.

7. Shape and structure versus growth

As a final section, it is appropriate to make a few comments to link the different shapes and the different classes of structure

to how they will evolve during growth. While the largest number of current papers deal with solution based growth, there are many other methods of making nanoparticles such as inert gas evaporation (e.g. [49–55, 337].), atomic layer deposition (e.g. [338–349].), evaporation or sputtering (e.g. [39, 40, 43, 308, 350–354].) and hydrothermal methods (e.g. [27–32, 105, 248, 275].). In this short section the intent is to look at some of the commonalities rather than attempting a full description or a detailed literature review.

The initial step will always be nucleation, in most cases after some incubation period. The nucleation may be homogeneous, for instance small groups of atoms in the gas phase or in a solution with ligands around them, or it can be heterogeneous at steps on a substrate, the side walls of the container or at contaminants. Some nuclei will disperse back to single atoms, some will grow, it is a statistical process. Depending upon the chemical potential of single atoms (or equivalent species such as complexes involving single atoms) the critical nucleus can be only two atoms or it can be 1–2 nm, as mentioned in section 4. Note that experimentally detecting very small nuclei is not that easy, and often they can only be inferred from forensic data. The shape and structure of the nuclei will be system dependent, both the material as well as

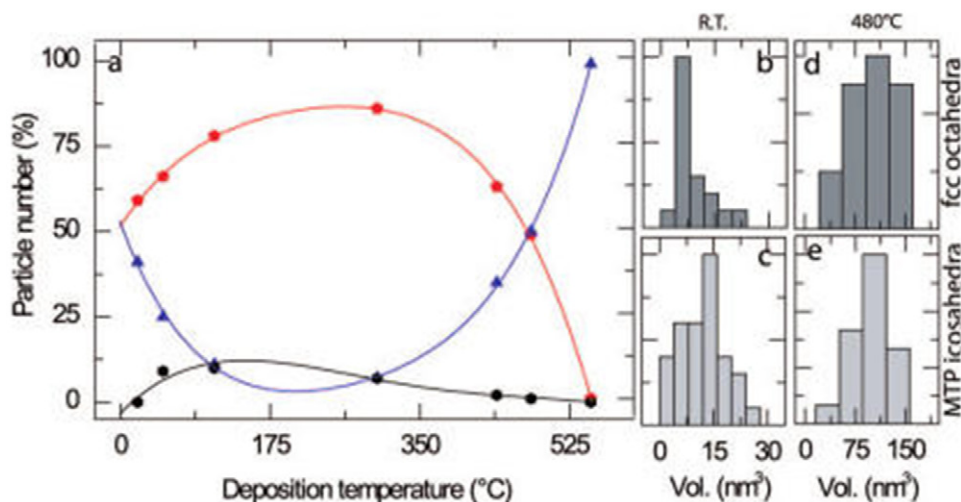


Figure 54. Evolution of the proportion of Cu nanocrystal shapes as a function of nucleation temperature. Red pentagon points represent the MTP icosahedral shapes, blue triangular points represent fcc nanocrystals, and black hexagonal points represent MTP Marks decahedron shapes. Best fit lines have been drawn through the data points. (b)–(e) Volume distributions of Cu nanocrystals nucleated at room temperature and at 480 °C for icosahedral shapes (c) and (e) and fcc nanocrystals (b) and (d), respectively. Reproduced with permission from [311], copyright (2009) American Chemical Society.

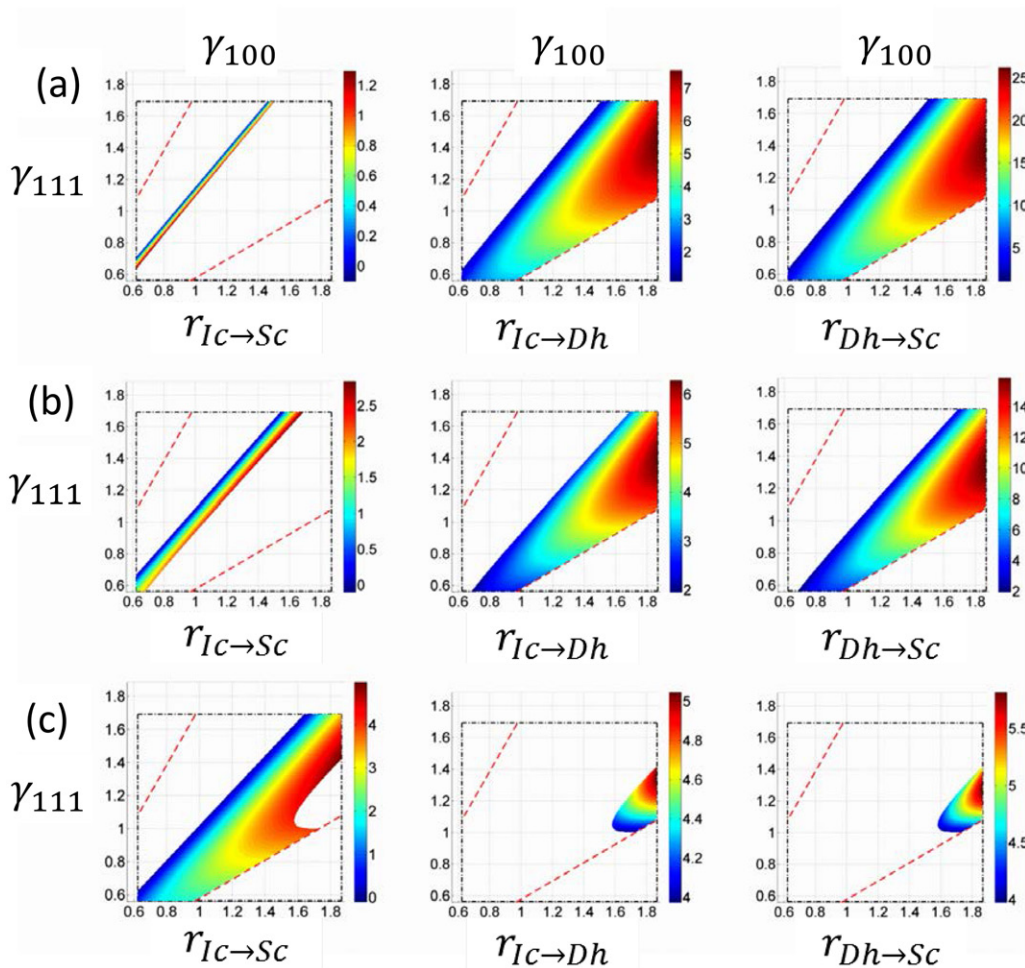


Figure 55. Plots of the transition radii for different values of the surface energies and also different values of the surface stress, in (a) -0.25 , in (b) 0.50 and in (c) 1.25 .

the external environment including any trace impurities such as oxygen leaks in a vacuum system or impurities in chemicals used in a solution based synthesis.

After nucleation there will be growth. Around each nanoparticle there will be a population of monomers and perhaps dimers and trimers, on the substrate and diffusing across for

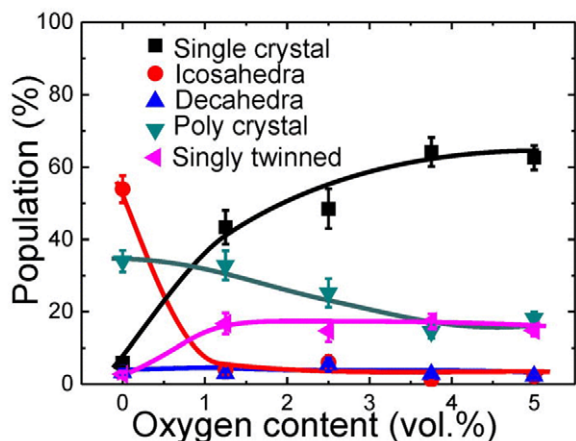


Figure 56. Plot of the relative fraction of different silver particles versus trace impurity levels of oxygen during formation; note the large changes. Reproduced with permission from [336], copyright 2012 American Institute of Physics.

deposition experiments; in the fluid phase for solution or argon-smoke based methods. Depending upon the rate of growth as well as the temperature the structures may change with the number of atoms or not. If we consider structural transformations as involving some form of vibration (phonon) the activation energy will scale approximately as the particle volume; if it is via migration of an internal boundary it will scale as the volume to the two-third power. Whichever is the mechanism, as the size increases transformations will become slower and eventually cease to be relevant for the time scales of the growth.

While often growth is by addition from an external fluid phase, it can also be via reaction of a solid phase such as an amorphous hydroxide particularly with hydrothermal growth methods (e.g. [27–32, 105, 248, 275]). In such cases as the nanoparticle grows there can be differential diffusion of species, which via the Kirkendall effect (e.g. [12, 355–360]), can lead to voids in the material—see for instance figure 10 earlier. The external shape and also the voids should still tend to conform to the thermodynamic and kinetic control issues described earlier; with time and temperature the voids will slowly collapse.

Depending upon conditions, the growth may involve local equilibration of the external surfaces via surface diffusion or not. In many cases chemisorbants, both small molecules and large surfactant molecules can play a large role in either accelerating or decelerating this. If surface diffusion is fast enough the shapes will tend to be the thermodynamic ones, either the global minima or the constrained minima; if it is slow then the kinetic routes will dominate [233, 361].

The surrounding cloud of monomers may slowly drop as the growth proceeds, for instance as chemicals are depleted in solution growth. There will always be some equilibrium concentration, as monomers can leave the nanoparticle and return to the surrounding medium. At high enough temperatures the concentration of these monomers can be high enough that there will be exchange between nanoparticles, Ostwald ripening where small particles shrink and larger ones grow (e.g. [362–368]). More rigorously, it will be those with higher

chemical potentials that shrink, either because of their internal structure or other contributions such as interfacial stresses.

There can also be growth via coalescence. In a fluid there is random Brownian motion of nanoparticles whereas on a substrate there can be net translation due to local fluctuations in the concentrations of monomers. With solution growth chemisorbed ligands can play an important role to prevent coalescence by acting as buffers. When two particles coalesce there will be a substantial release of energy due to reduction of exposed surfaces, which may be large enough to lead to a full restructuring. They may rotate relative to each other to form low-angle boundaries or adopt the same orientation (e.g. [369–376]), be frozen leading to polyparticles or other complex structures [47, 377] or transform to MTPs [308]; the general process will involve neck formation and is referred to as sintering (e.g. [378–385]).

One point that should be mentioned is that the kinetic shapes will eventually revert back to thermodynamic ones—as Homer Simpson knows you cannot beat thermodynamics. This is particularly important for heterogeneous catalysis where catalysts used in any commercial system will almost always contain nanoparticles with the thermodynamic structures for the particular set of conditions of gas and temperature used. However, this shape conversion does not have to be that fast. Just as there is an activation energy barrier to the formation of a new terrace during growth, there is an activation energy barrier to the formation of new regions on a nanoparticle during equilibration of the shape via surface diffusion. This has been fairly well discussed in the literature (e.g. [386–394], and references therein).

Every system is different. Small details will matter, for instance the precise form of the potential, and can in fact dominate the results. We are dealing with a complex kinetic and thermodynamic system which should be described as a large set of differential equations which may either have simple solutions or display more chaotic behavior (in the true sense of chaos theory). We have not gone into any details here, but it does not have to be that with kinetic Wulff shape growth a nanoparticle will simply converge to a specific form, it could oscillate about it or even spiral around an average, a complex problem in the mathematics of fixed-point problems.

In a very general sense the final result will tend to fall into one of three classes as illustrated in figure 57:

Survival of the Fittest: thermodynamic equilibria dominate, either global or constrained local minima with the nanoparticles tending to be close to spherical with facets and in some cases surface steps, small terraces and at higher temperatures roughened regions.

Survival of the Fastest: kinetics dominate, those which grow fastest will tend to dominate the population and the nanoparticles will tend to have sharp facets with rounded corners and edges, the rounding depending upon the chemical potentials during growth.

Survival of a Population: the stochastics of the evolution of the combination of different nanoparticles and different local concentrations of monomers will dominate, and there will be many slightly asymmetric shapes including polyparticles as well as the symmetric ones.

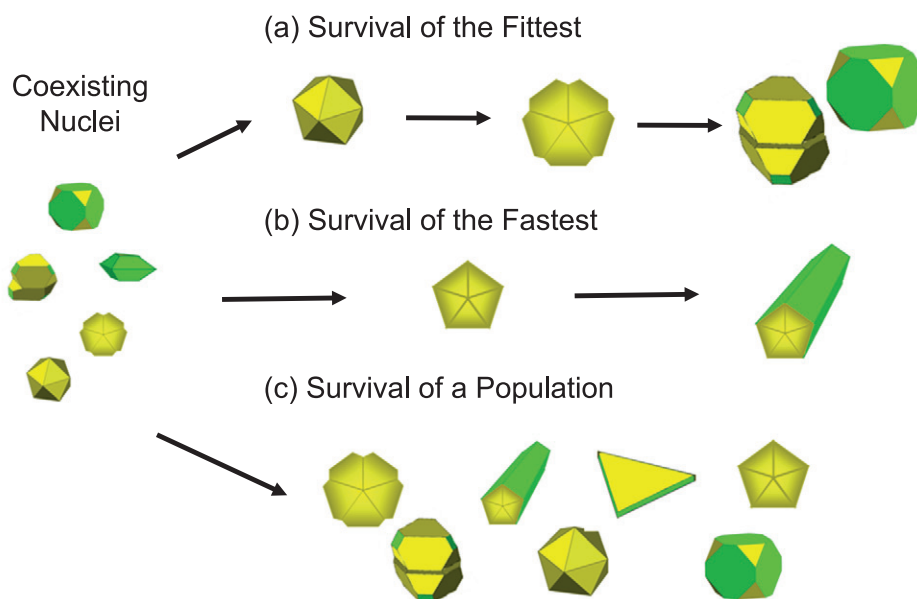


Figure 57. Three general routes for nanoparticle shape and structure as a function of growth. Starting from a diverse population of nuclei illustrated on the left, in (a) is shown Survival of the Fittest, i.e. the thermodynamic route from $Ic \rightarrow Dh \rightarrow$ Single crystals and LTP; in (b) Survival of the Fastest, here illustrated by rapidly growing Dh rods, and in (c) Survival of a Population where the initial nuclei all grow under kinetic control.

8. Discussion

In this review we have tried to create a snapshot of the current understanding. While there has been more focus on MTPs, the wider range of Wulff shapes both kinetic and thermodynamic apply across the board largely independent of the method of producing the nanoparticles. Comparing the field to when one of us reviewed it last [2] it has come a long way. The number of papers has exploded, there are many new and varied methods of producing shape controlled nanoparticles. Our understanding of fine details such as atom-by-atom analysis of experimental structures and high level atomistic modelling have come a long way. A number of new areas have opened up, for instance the additional complications when the nanoparticles are alloys and also the possibilities of chemical ordering in the bulk and at the surface where the field is still evolving; another is quantitative measurements of the strain fields.

Many aspects of nanoparticle shape and thermodynamics are quite clear, and there is an overwhelming amount of evidence both theoretically and experimentally. The older continuum based ideas dating back in many cases to the early 20th century have held up well. The large family of Wulff constructions now extended from the earlier thermodynamic cases to the kinetic cases describe the broad details. Most atomistic models are in good agreement with the continuum based approaches which have been the main focus here. There are fine details where they differ, partially because the continuum models require numbers for parameters that have to come from elsewhere, while atomistic calculations give slightly (or very) different results depending upon the potentials used. While density functional methods have become common, quite fast and can be moderately accurate, it is worth remembering that many functionals give inaccurate surface energies since they do not go to the correct jellium limit.

Given the size of the literature it is not possible to cover everything, but we have tried to be moderately comprehensive including not only our own results but also those of others. There are many areas such as the specifics of atomistic chemisorption and how this translates to different activation energy barriers which we have not attempted to cover, and are themselves worthy of review articles. Our focus has been more on the continuum model which we believe are powerful in their predictive power, albeit requiring input from atomistic models or experiment for values of terms such as the surface stress tensor.

There are still many unknowns, a brief mention of some of these is included here to hopefully inspire a little more research:

1. As mentioned in the introduction, many issues were raised in the early 20th century which have yet to be solved and are of fundamental importance. For instance, frequently high index surfaces occur in the Wulff shape particularly at higher temperatures. By definition, the unit area of any of these is large so there will not be space for them. While it is not hard to formulate models for this, for instance adding integer constraints for the size of facets, to what extent this is correct is unclear. Careful, detailed measurements of the Wulff shape as a function of size would be highly informative; there could be new phenomena here.
2. It has almost become *de rigueur* in nanoparticle papers to include a high resolution electron microscope image (or several) and some level of atomistic simulation such as a molecular dynamics calculation. However, it is not always clear that these advance the science. We are strong believers in the natural sciences philosophy, where experiments should inspire predictive theory which in turn is

verified or disproved by more experiments. More important than just showing qualitative agreement between theory and experiment is being able to predict, and we urge authors to consider going beyond just reporting results (and referees to allow predictive hypotheses to be included.)

3. There has been a revolution in the last decade in what can be done using transmission electron microscopes. However, just because a powerful aberration-corrected microscope is used does not make interpretation of the images easier. All images are equal, but some images are more equal than others. There is no such thing as a dynamical diffraction corrector, and user-correctors are often not used [395]. It is easy to be overwhelmed by information overload with images of hundreds of nanoparticles and miss the unexpected.
4. Computers are following Moore's law, so atomistic calculations are becoming faster and easier. This does not mean that they are always becoming more accurate. In other areas such as surface science it has been known for many years that while ab-initio methods such as density functional theory are very powerful because they have no inbuilt assumptions, because of approximations and inaccuracies in the functionals used they can be inaccurate with errors of 0.1 eV/atom (2.3 kcal/mole) or worse particularly for surface enthalpies. The field of functionals is moving quite rapidly, and there are much better new functionals available, e.g. [396–409]. There is already data that this can matter, for instance in the transition from 2D to 3D in gold clusters of a few atoms [410] where older methods do not agree with experimental data but more advanced functionals do. Information on not just structures but enthalpies with error estimates and the use of better functionals may reveal currently hidden errors or limitations in the literature.
5. It is still ambiguous how nanoparticles evolve *in detail* as a function of size and reaction conditions for solvent based methods. For instance, what is the population of the different shapes and how does this vary with the chemical potential of the different components in solution? Beyond just the averages, what are the variations about the mean? This has real physical significance in terms of understanding fluctuations in the growth conditions and the kinetic growth trajectories—the steady state solution is only an asymptotic limit. It is hard to find systematic studies with hard numbers for, for instance, the metal chemical potentials in solution which are the grist of theoretical models. Counting shapes is tedious, but important.
6. What, quantitatively are the full 3D atomic positions of the atoms in nanoparticles, and how does this vary as a function of conditions? Electron microscopes are approaching this (e.g. [280, 411–426].), but there is still much more work to be done particularly in terms of controlling the samples. We suspect that there will be no simple answer and the results will vary depending upon the exact preparation conditions as well as post preparation treatments.

There will also be the issues of the role of the surfaces which may determine everything, which is complicated as the gas ambient is rarely controlled in electron microscopes.

7. What is the surface structure of the nanoparticles under representative synthesis conditions? Forensic examination of nanoparticles including their surfaces has been possible at the atomic scale for more than thirty years (e.g. [427–432].), and what takes place on metals is fairly well understood. With oxides as well as many other systems very little is known, and it is clear that the surface structure and composition depends upon the synthesis conditions [85], with, for strontium titanate, the surface structure being consistent with the lowest energy structures for flat surfaces [86–101]. This needs to be better understood for all types of nanoparticles beyond simple metals, as theoretical models with incorrect assumptions about the surface will not be able to move the field forward.
8. The eye is often drawn to the more perfect shapes, for instance pentagonal bi-pyramids which can be quite beautiful. There is a large amount of science in the less than perfect nanoparticles. In particular, statistical fluctuations about the average may be a very important aspect to be analyzed further, and we have included in figures 35 and 48 some of our preliminary results in these directions. If we can understand and predict the fluctuations about the mean, not just the mean, the science of controlling nanoparticles will move a long way forward.

It would be nice to think that six-sigma control is just around the corner; maybe it is, but we suspect it will take a bit more time.

Acknowledgements

This work would have been impossible without contributions from many others over more than thirty years. LDM would like to particularly thank A Howie and D J Smith for their mentoring of a graduate student who liked to work nights, and E Yoffe and J Dundurs for solving some intractable elasticity problems. A number of graduate students have also contributed to many parts of this work, most notably P M. Ajayan, J Enterkin, Y Lin and E Ringe as well as a postdoc S Patala; thanks also to D Alpay, J E Bonevich, L. Crosby and D. Noraiswamy. Many others have freely contributed time and papers including unpublished work, most notably M Castell, S Iijima, A Kirkland, A Pimpinelli, N Tanaka, P Voorhees and M Yacaman. Parts of this work evolved via collaborative projects with other faculty at Northwestern University, K R Poepelmeier, P Stair and R Van Duyn. Writing of the paper and funding for LP was supported by the materials Research Center (MRSEC) at Northwestern University, on the grant MRSEC-1121262. The MRSEC is funded through the National Science Foundation; a number of other agencies supported the research which is mentioned in various parts of the paper.

References

- [1] Whewell W 1847 *The Philosophy of the Inductive Sciences, Founded Upon Their History* (London: John W. Parker)
- [2] Marks L D 1994 Experimental studies of small-particle structures *Rep. Prog. Phys.* **57** 603–49
- [3] Hofmeister H 1998 Forty years study of fivefold twinned structures in small particles and thin films *Cryst. Res. Technol.* **33** 3–25
- [4] Gryaznov V G, Heydenreich J, Kaprelov A M, Nepijko S A, Romanov A E and Urban J 1999 Pentagonal symmetry and disclinations in small particles *Cryst. Res. Technol.* **34** 1091–19
- [5] Winn D and Doherty M F 2000 Modeling crystal shapes of organic materials grown from solution *Aiche J.* **46** 1348–67
- [6] Yacaman M J, Ascencio J A, Liu H B and Gardea-Torresdey J 2001 Structure shape and stability of nanometric sized particles *J. Vac. Sci. Technol. B* **19** 1091–103
- [7] Astruc D, Lu F and Aranzaes J R 2005 Nanoparticles as recyclable catalysts: the frontier between homogeneous and heterogeneous catalysis *Angew. Chem. Int. Ed. Engl.* **44** 7852–72
- [8] Baletto F and Ferrando R 2005 Structural properties of nanoclusters: Energetic, thermodynamic, and kinetic effects *Rev. Mod. Phys.* **77** 371–423
- [9] Rosi N L and Mirkin C A 2005 Nanostructures in biodiagnostics *Chem. Rev.* **105** 1547–62
- [10] Hu M, Chen J, Li Z Y, Au L, Hartland G V, Li X, Marquez M 2006 and Xia Y 2006 Gold nanostructures: engineering their plasmonic properties for biomedical applications *Chem. Soc. Rev.* **35** 1084–94
- [11] Jun Y W, Choi J S and Cheon J 2006 Shape control of semiconductor and metal oxide nanocrystals through nonhydrolytic colloidal routes *Angew. Chem. Int. Ed. Engl.* **45** 3414–39
- [12] Fan H J, Gosele U and Zacharias M 2007 Formation of nanotubes and hollow nanoparticles based on Kirkendall and diffusion processes: a review *Small* **3** 1660–71
- [13] Anker J N, Hall W P, Lyandres O, Shah N C, Zhao J and Van Duyne R P 2008 Biosensing with plasmonic nanosensors *Nat. Mater.* **7** 442–53
- [14] Grzelczak M, Perez-Juste J, Mulvaney P and Liz-Marzan L M 2008 Shape control in gold nanoparticle synthesis *Chem. Soc. Rev.* **37** 1783–91
- [15] Hofmeister H 2009 Shape variations and anisotropic growth of multiply twinned nanoparticles *Z. Kristallogr.* **224** 528–38
- [16] Millstone J E, Hurst S J, Metraux G S, Cutler J I and Mirkin C A 2009 Colloidal gold and silver triangular nanoprisms *Small* **5** 646–64
- [17] Xia Y, Xiong Y, Lim B and Skrabalak S E 2009 Shape-controlled synthesis of metal nanocrystals: simple chemistry meets complex physics? *Angew. Chem. Int. Ed. Engl.* **48** 60–103
- [18] Mayoral A, Barron H, Estrada-Salas R, Vazquez-Duran A and Jose-Yacaman M 2010 Nanoparticle stability from the nano to the meso interval *Nanoscale* **2** 335–42
- [19] Cao Y L, Ding X L, Li H C, Yi Z G, Wang X F, Zhu J J and Kan C X 2011 Morphology-controllable noble metal nanoparticles: synthesis, optical property and growth mechanism *Acta Phys. Chim. Sin.* **27** 1273–86
- [20] Henry A I, Bingham J M, Ringe E, Marks L D, Schatz G C and Van Duyne R P 2011 Correlated structure and optical property studies of plasmonic nanoparticles *J. Phys. Chem. C* **115** 9291–305
- [21] Prabhu S and Poulouse E K 2012 Silver nanoparticles: mechanism of antimicrobial action, synthesis, medical applications, and toxicity effects *Int. Nano Lett.* **2** 32
- [22] Li N, Zhao P and Astruc D 2014 Anisotropic gold nanoparticles: synthesis, properties, applications, and toxicity *Angew. Chem. Int. Ed. Engl.* **53** 1756–89
- [23] Thanh N T, Maclean N and Mahiddine S 2014 Mechanisms of nucleation and growth of nanoparticles in solution *Chem. Rev.* **114** 7610–30
- [24] Ringe E 2014 Nanocrystalline materials: recent advances in crystallographic characterization techniques *IUCrJ* **1** 530–9
- [25] Alex S and Tiwari A 2015 Functionalized gold nanoparticles: synthesis, properties and applications—a review *J. Nanosci. Nanotechnol.* **15** 1869–94
- [26] Haider A and Kang I K 2015 Preparation of silver nanoparticles and their industrial and biomedical applications: a comprehensive review *Adv. Mater. Sci. Eng.* **2015** 165257
- [27] Rabenau A 1985 The role of hydrothermal synthesis in preparative chemistry *Angew. Chem. Int. Ed. Engl.* **24** 1026–40
- [28] Adschiri T, Hakuta Y and Arai K 2000 Hydrothermal synthesis of metal oxide fine particles at supercritical conditions *Ind. Eng. Chem. Res.* **39** 4901–7
- [29] Goh G K L, Haile S M, Levi C G and Lange F F 2002 Hydrothermal synthesis of perovskite and pyrochlore powders of potassium tantalate *J. Mater. Res.* **17** 3168–76
- [30] Suchanek W L and Riman R E 2006 Hydrothermal synthesis of advanced ceramic powders *Adv. Sci. Technol.* **45** 184–93
- [31] Modeshia D R and Walton R I 2010 Solvothermal synthesis of perovskites and pyrochlores: crystallisation of functional oxides under mild conditions *Chem. Soc. Rev.* **39** 4303–25
- [32] Zhu X H and Hang Q M 2013 Microscopical and physical characterization of microwave and microwave-hydrothermal synthesis products *Micron* **44** 21–44
- [33] Wulff G 1901 On the question of speed of growth and dissolution of crystal surfaces *Z. Kristallogr. Mineral.* **34** 449–530
- [34] Hofmeister H 2004 Fivefold twinned nanoparticles *Encyclopedia Nanosci. Nanotechnol.* **3** 431–52
- [35] Evans D M and Wilman H 1952 Crystal growth and orientation in deposits condensed from the vapour *Acta Crystallog.* **5** 731–8
- [36] Melmed A J and Hayward D O 1959 Occurrence of fivefold rotational symmetry in metal whiskers *J. Chem. Phys.* **31** 545–6
- [37] Ogburn F, Peiser H S and Paretzkin B 1964 Pseudopentagonal twins in electrodeposited copper dendrites *Acta Crystallogr.* **17** 774
- [38] Schwoebel R L 1966 Anomalous growth of gold from the vapor phase *J. Appl. Phys.* **37** 2515–6
- [39] Ino S 1966 Epitaxial growth of metals on rocksalt faces cleaved in vacuum.2. Orientation and structure of gold particles formed in ultrahigh vacuum *J. Phys. Soc. Japan* **21** 346–62
- [40] Ino S and Ogawa S 1967 Multiply twinned particles at earlier stages of gold film formation on alkali halide crystals *J. Phys. Soc. Japan* **42** 1365–74
- [41] Ino S 1969 Stability of multiply-twinned particles *J. Phys. Soc. Japan* **27** 941–53
- [42] Marks L D 1980 *The Structure of Small Silver Particles* (Cambridge: Cambridge University Press)
- [43] Allpress J G and Sanders J V 1967 Structure and orientation of crystals in deposits of metals on mica *Surf. Sci.* **7** 1–25
- [44] Volterra V 1907 Sur l'équilibre des corps élastiques multiplement connexes *Annu. Sci. d de l'Ecole Norm. Supér.* **24** 401–517
- [45] Komoda T 1968 Study on structure of evaporated gold particles by means of a high resolution electron microscope *Japan. J. Appl. Phys.* **7** 27–30

- [46] Marks L D and Smith D J 1981 High resolution studies of small particles of gold and silver: I. Multiply-twinned particles *J. Cryst. Growth* **54** 425–32
- [47] Smith D J and Marks L D 1981 High-resolution studies of small particles of gold and silver.2. Single-crystals, lamellar twins and polyparticles *J. Cryst. Growth* **54** 433–8
- [48] Hoare M R and Pal P 1972 Statistics and stability of small assemblies of atoms *J. Cryst. Growth* **17** 77–96
- [49] Kazuo K and Isao N 1967 An electron microscope and electron diffraction study of fine smoke particles prepared by evaporation in argon gas at low pressures (II) *Japan. J. Appl. Phys.* **6** 1047
- [50] Yatsuya S, Kasukabe S and Uyeda R 1973 Formation of ultrafine metal particles by gas evaporation technique.1. Aluminum in helium *Japan. J. Appl. Phys.* **12** 1675–84
- [51] Kasukabe S, Yatsuya S and Uyeda R 1974 Ultrafine metal particles formed by gas-evaporation technique.2. Crystal habits of magnesium, manganese, beryllium and tellurium *Japan. J. Appl. Phys.* **13** 1714–21
- [52] Ohno T, Yatsuya S and Uyeda R 1976 Formation of ultrafine metal particles by gas-evaporation technique.3. Al in He, Ar and Xe, and Mg in mixtures of inactive gas and air *Japan. J. Appl. Phys.* **15** 1213–7
- [53] Granqvist C G 1976 Ultrafine metal particles *J. Appl. Phys.* **47** 2200
- [54] Hayashi T, Ohno T, Yatsuya S and Uyeda R 1977 Formation of ultrafine metal particles by gas-evaporation technique.4. Crystal habits of iron and Fcc metals, Al, Co, Ni, Cu, Pd, Ag, In, Au and Pb *Japan. J. Appl. Phys.* **16** 705–17
- [55] Dmitrieva O, Rellinghaus B, Kästner J and Dumpich G 2007 Quantitative structure analysis of L10-ordered FePt nanoparticles by HRTEM *J. Cryst. Growth* **303** 645–50
- [56] Wales D J, Kirkland A I and Jefferson D A 1989 Structure and growth of colloidal metal particles *J. Chem. Phys.* **91** 603–11
- [57] Kirkland A I, Edwards P P, Jefferson D A and Duff D G 1990 The structure, characterization, and evolution of colloidal metals *Annu Rep. C* **87** 247
- [58] Martínez A 2001 *The Truth about Darwin's Finches, Einstein's Wife, and Other Myths* (Pittsburgh, PA: University of Pittsburgh Press)
- [59] Cleveland C L and Landman U 1991 The energetics and structure of nickel clusters—size dependence *J. Chem. Phys.* **94** 7376–96
- [60] Hamilton J C 2006 Edge energies: atomistic calculations of a continuum quantity *Phys. Rev. B* **73** 125447
- [61] Barnard A S, Young N P, Kirkland A I, van Huis M A and Xu H F 2009 Nanogold: a quantitative phase map *Acs Nano* **3** 1431–6
- [62] Barnard A S 2010 Modelling of nanoparticles: approaches to morphology and evolution *Rep. Prog. Phys.* **73** 086502
- [63] Marks L D 1983 Modified wulff constructions for twinned particles *J. Cryst. Growth* **61** 556–66
- [64] Howie A and Marks L D 1984 Elastic strains and the energy-balance for multiply twinned particles *Phil. Mag. A* **49** 95–109
- [65] Marks L D 1984 Surface-structure and energetics of multiply twinned particles *Phil. Mag. A* **49** 81–93
- [66] Taylor J E 1992 Mean-curvature and weighted mean-curvature.2 *Acta Metall. Et Mater.* **40** 1475–85
- [67] Alpay D, Peng L and Marks L D 2015 Are nanoparticle corners round? *J. Phys. Chem. C* **119** 21018–23
- [68] Cahn J W and Hoffman D W 1974 Vector thermodynamics for anisotropic surfaces.2. Curved and faceted surfaces *Acta Metall.* **22** 1205–14
- [69] Dicarolo A, Gurtin M E and Podioguidugli P 1992 A regularized equation for anisotropic motion-by-curvature *SIAM J. Appl. Math.* **52** 1111–9
- [70] Voorhees P W, Coriell S R, Mcfadden G B and Sekerka R F 1984 The effect of anisotropic crystal melt surface-tension on grain-boundary groove morphology *J. Cryst. Growth* **67** 425–40
- [71] Golovin A A, Davis S H and Nepomnyashchy A A 1998 A convective Cahn-Hilliard model for the formation of facets and corners in crystal growth *Physica D* **122** 202–30
- [72] Akaiwa N, Thornton K and Voorhees P W 2001 Large-scale simulations of microstructural evolution in elastically stressed solids *J. Comput. Phys.* **173** 61–86
- [73] Eggleston J J, McFadden G B and Voorhees P W 2001 A phase-field model for highly anisotropic interfacial energy *Physica D* **150** 91–103
- [74] Wise S, Kim J and Lowengrub J 2007 Solving the regularized, strongly anisotropic Cahn-Hilliard equation by an adaptive nonlinear multigrid method *J. Comput. Phys.* **226** 414–46
- [75] Torabi S, Lowengrub J, Voigt A and Wise S 2009 A new phase-field model for strongly anisotropic systems *Proc. R. Soc. A* **465** 1337–59
- [76] Mastroberardino A and Spencer B J 2010 3D equilibrium crystal shapes with corner energy regularization *IMA J. Appl. Math.* **75** 190–205
- [77] Drucker J 1993 Coherent islands and microstructural evolution *Phys. Rev. B* **48** 18203–6
- [78] Hammar M, LeGoues F K, Tersoff J, Reuter M C and Tromp R M 1996 *In situ* ultrahigh vacuum transmission electron microscopy studies of hetero-epitaxial growth.1. Si(001)/Ge *Surf. Sci.* **349** 129–44
- [79] Ross F M, Tersoff J and Tromp R M 1998 Coarsening of self-assembled Ge quantum dots on Si(001) *Phys. Rev. Lett.* **80** 984–7
- [80] Hamilton J C, Léonard F, Johnson E and Dahmen U 2007 Pb nanoprecipitates in Al: magic-shape effects due to elastic strain *Phys. Rev. Lett.* **98** 236102
- [81] Muller P and Saul A 2004 Elastic effects on surface physics *Surf. Sci. Rep.* **54** 157–258
- [82] Pimpinelli A and Villain J 1998 *Physics of Crystal Growth* (Cambridge: Cambridge University Press)
- [83] Watari M, McKendry R A, Vogtli M, Aeppli G, Soh Y A, Shi X, Xiong G, Huang X, Harder R and Robinson I K 2011 Differential stress induced by thiol adsorption on faceted nanocrystals *Nat. Mater.* **10** 862–6
- [84] Lin Y, Wu Z, Wen J, Poepelmeier K R and Marks L D 2014 Imaging the atomic surface structures of CeO₂ nanoparticles *Nano Lett.* **14** 191–6
- [85] Lin Y, Wen J, Hu L, Kennedy R M, Stair P C, Poepelmeier K R and Marks L D Synthesis-dependent atomic surface structures of oxide nanoparticles *Phys. Rev. Lett.* **111** 156101
- [86] Jiang Q D and Zegenhagen J 1999 c(6 × 2) and c(4 × 2) reconstruction of SrTiO₃(001) *Surf. Sci.* **425** 343–54
- [87] Castell M R 2002 Nanostructures on the SrTiO₃(001) surface studied by STM *Surf. Sci.* **516** 33–42
- [88] Castell M R 2002 Scanning tunneling microscopy of reconstructions on the SrTiO₃(001) surface *Surf. Sci.* **505** 1–13
- [89] Erdman N, Poepelmeier K R, Asta M, Warschkow O, Ellis D E and Marks L D 2002 The structure and chemistry of the TiO₂-rich surface of SrTiO₃(001) *Nature* **419** 55–8
- [90] Erdman N, Warschkow O, Asta M, Poepelmeier K R, Ellis D E and Marks L D 2003 Surface structures of SrTiO₃(001): a TiO₂-rich reconstruction with a c(4 × 2) unit cell *J. Am. Chem. Soc.* **125** 10050–6
- [91] Johnston K, Castell M R, Paxton A T and Finnis M W 2004 SrTiO₃(001)(2 × 1) reconstructions: first-principles calculations of surface energy and atomic structure compared with scanning tunneling microscopy images *Phys. Rev. B* **70** 085415
- [92] Warschkow O, Asta M, Erdman N, Poepelmeier K R, Ellis D E and Marks L D 2004 TiO₂-rich reconstructions of SrTiO₃(001): a theoretical study of structural patterns *Surf. Sci.* **573** 446–56

- [93] Silly F and Castell M R 2005 Self-assembled supported Co nanocrystals: The adhesion energy of face-centered-cubic Co on SrTiO₃(001)-(2 × 2) *Appl. Phys. Lett.* **87** 053106
- [94] Silly F, Newell D T and Castell M R 2006 SrTiO₃(001) reconstructions: the (2 × 2) to c(4 × 4) transition *Surf. Sci.* **600** L219–23
- [95] Newell D T 2007 The surface structure and reconstructions of SrTiO₃(001) *Materials* (Oxford: Oxford University Press) p 168
- [96] Herger R, Willmott P R, Bunk O, Schleputz C M, Patterson B D and Delley B 2007 Surface of strontium titanate *Phys. Rev. Lett.* **98** 076102
- [97] Kienzle D M, Becerra-Toledo A E and Marks L D 2011 Vacant-site octahedral tilings on SrTiO₃(001), the (root 13 × root 13)R33.7 degrees surface, and related structures *Phys. Rev. Lett.* **106** 176102
- [98] Zhu G Z, Radtke G and Botton G A 2012 Bonding and structure of a reconstructed (001) surface of SrTiO₃ from TEM *Nature* **490** 384–7
- [99] Kienzle D M and Marks L D 2012 Surface transmission electron diffraction for SrTiO₃ surfaces *CrystEngComm* **14** 7833–9
- [100] Marshall M J, Becerra-Toledo A, Marks L and Castell M 2015 Defects on strontium titanate *Defects at Oxide Surfaces* ed J Jupille and G Thornton (New York: Springer International Publishing) pp 327–49
- [101] Ciston J *et al* 2015 Surface determination through atomically resolved secondary-electron imaging *Nat. Commun.* **6** 7358
- [102] Hoffman D W and Cahn J W 1972 Vector thermodynamics for anisotropic surfaces. I. Fundamentals and application to plane surface junctions *Surf. Sci.* **31** 368–88
- [103] von Laue M 1943 Der Wulffsche satz fur die gleichgewichtsform von kristallen *Z. Kristallogr.* **105** 124–33
- [104] Dinghas A 1944 Uber einen geometrischen sat von Wulff fur die gleichgewichtsform von kristallen *Z. Kristallogr.* **105** 304–14
- [105] Crosby L, Enterkin J, Rabuffetti F, Poepelmeier K and Marks L 2015 Wulff shape of strontium titanate nanocuboids *Surf. Sci.* **632** L22–5
- [106] Zucker R, Chatain D, Dahmen U, Hagège S and Carter W C 2012 New software tools for the calculation and display of isolated and attached interfacial-energy minimizing particle shapes *J. Mater. Sci.* **47** 1–13
- [107] Tian N, Zhou Z Y and Sun S G 2008 Platinum metal catalysts of high-index surfaces: from single-crystal planes to electrochemically shape-controlled nanoparticles *J. Phys. Chem. C* **112** 19801–17
- [108] Winterbottom W L 1967 Equilibrium shape of a small particle in contact with a foreign substrate *Acta Metall.* **15** 303–10
- [109] Zia R K P, Avron J E and Taylor J E 1988 The summertop construction—crystals in a corner *J. Stat. Phys.* **50** 727–36
- [110] Lin Y, Wu Z, Wen J, Ding K, Yang X, Poepelmeier K R and Marks L D 2015 Adhesion and atomic structures of gold on ceria nanostructures: the role of surface structure and oxidation state of ceria supports *Nano Lett.* **15** 5375–81
- [111] Ajayan P M and Marks L D 1989 Evidence for sinking of small particles into substrates and implications for heterogeneous catalysis *Nature* **338** 139–141
- [112] Marks L D and Ajayan P M 1990 Equilibrium shape of a buoyant particle *J. Mater. Res.* **5** 1496–501
- [113] Gontard L C, Dunin-Borkowski R E, Gass M H, Bleloch A L and Ozkaya D 2009 3D shapes and structures of lamellar-twinned fcc nanoparticles using ADF STEM *J. Electron Microsc.* **58** 167–74
- [114] Ji W H, Qi W H, Tang S S, Huang B Y, Wang M P, Li Y, Jia Y L and Pang Y 2014 Synthesis of marks-decahedral pd nanoparticles in aqueous solutions *Part. Part. Syst. Charact.* **31** 851–6
- [115] Mariscal M M, Velazquez-Salazar J J and Yacaman M J 2012 Growth mechanism of nanoparticles: theoretical calculations and experimental results *CrystEngComm* **14** 544–9
- [116] Yacaman M J 2012 Private communication
- [117] Hubert H, Devouard B, Garvie L A J, O’Keeffe M, Buseck P R, Petuskey W T and McMillan P F 1998 Icosahedral packing of B-12 icosahedra in boron suboxide (B6O) *Nature* **391** 376–8
- [118] Dundurs J, Marks L D and Ajayan P M 1988 Structural fluctuations in small particles *Phil. Mag. A* **57** 605–20
- [119] Lim B, Wang J G, Camargo P H C, Cobley C M, Kim M J and Xia Y N 2009 Twin-induced growth of palladium-platinum alloy nanocrystals *Angew. Chem. Int. Ed.* **48** 6304–8
- [120] Koga K 2006 Novel bidecahedral morphology in gold nanoparticles frozen from liquid *Phys. Rev. Lett.* **96** 115501
- [121] Hoare M R and Pal P 1971 Physical cluster mechanics—statics and energy surfaces for monatomic systems *Adv. Phys.* **20** 161–96
- [122] Hoare M R and Pal P 1975 Physical cluster mechanics—statistical thermodynamics and nucleation theory for monatomic systems *Adv. Phys.* **24** 645–78
- [123] McEachran M and Kitaev V 2008 Direct structural transformation of silver platelets into right bipyramids and twinned cube nanoparticles: morphology governed by defects *Chem. Commun.* **44** 5737–9
- [124] Zhang J, Li S, Wu J, Schatz G C and Mirkin C A 2009 Plasmon-mediated synthesis of silver triangular bipyramids *Angew. Chem. Int. Ed. Engl.* **48** 7787–91
- [125] Wiley B J, Xiong Y, Li Z-Y, Yin Y and Xia Y 2006 Right bipyramids of silver: a new shape derived from single twinned seeds *Nano Lett.* **6** 765–8
- [126] Lu J, Low K B, Lei Y, Libera J A, Nicholls A, Stair P C and Elam J W 2014 Toward atomically-precise synthesis of supported bimetallic nanoparticles using atomic layer deposition *Nat. Commun.* **5** 3264
- [127] Serpell C J, Cookson J, Ozkaya D and Beer P D 2011 Core@shell bimetallic nanoparticle synthesis via anion coordination *Nat. Chem.* **3** 478–83
- [128] Chen H Y, Li Y, Zhang F B, Zhang G L and Fan X B 2011 Graphene supported Au-Pd bimetallic nanoparticles with core-shell structures and superior peroxidase-like activities *J. Mater. Chem.* **21** 17658–61
- [129] Li B, Wen X, Li R, Wang Z, Clem P G and Fan H 2014 Stress-induced phase transformation and optical coupling of silver nanoparticle superlattices into mechanically stable nanowires *Nat. Commun.* **5** 4179
- [130] Stappert S, Rellinghaus B, Acet M and Wassermann E F 2003 Gas-phase preparation of L10 ordered FePt nanoparticles *J. Cryst. Growth* **252** 440–50
- [131] Wang D L, Xin H L L, Hovden R, Wang H S, Yu Y C, Muller D A, DiSalvo F J and Abruna H D 2013 Structurally ordered intermetallic platinum-cobalt core-shell nanoparticles with enhanced activity and stability as oxygen reduction electrocatalysts *Nat. Mater.* **12** 81–7
- [132] Langlois C, Li Z L, Yuan J, Alloyeau D, Nelayah J, Bochicchio D, Ferrando R and Ricolleau C 2012 Transition from core-shell to Janus chemical configuration for bimetallic nanoparticles *Nanoscale* **4** 3381–8
- [133] Song Y, Liu K and Chen S 2012 AgAu bimetallic Janus nanoparticles and their electrocatalytic activity for oxygen reduction in alkaline media *Langmuir* **28** 17143–52
- [134] Herzing A A, Watanabe M, Edwards J K, Conte M, Tang Z R, Hutchings G J and Kiely C J 2008 Energy dispersive x-ray spectroscopy of bimetallic nanoparticles

- in an aberration corrected scanning transmission electron microscope *Faraday Dis.* **138** 337–51
- [135] Cui C H, Gan L, Heggen M, Rudi S and Strasser P 2013 Compositional segregation in shaped Pt alloy nanoparticles and their structural behaviour during electrocatalysis *Nat. Mater.* **12** 765–71
- [136] Chen S, Ferreira P J and Shao-Horn Y 2007 Surface segregation in Pt₃Co nanoparticles characterized by scanning transmission electron microscopy *Microsc. Microanal.* **13** 604–5
- [137] Ringe E, Van Duyne R P and Marks L D 2011 Wulff construction for alloy nanoparticles *Nano Lett.* **11** 3399–403
- [138] Peng L, Ringe E, Van Duyne R P and Marks L D 2015 Segregation in bimetallic nanoparticles *Phys. Chem. Chem. Phys.* **17** 27940–51
- [139] Suntivich J *et al* 2013 Surface composition tuning of Au-Pt bimetallic nanoparticles for enhanced carbon monoxide and methanol electro-oxidation *J. Am. Chem. Soc.* **135** 7985–91
- [140] Marks L D 1985 Particle-size effects on wulff constructions *Surf. Sci.* **150** 358–66
- [141] Finch G I and Fordham S 1936 The effect of crystal-size on lattice-dimensions *Proc. Phys. Soc.* **48** 85–94
- [142] Boswell F W C 1951 Precise determination of lattice constants by electron diffraction and variations in the lattice constants of very small crystallites *Proc. Phys. Soc. London A* **64** 465–76
- [143] Berry C R 192 Electron diffraction from small crystals *Phys. Rev.* **88** 596–9
- [144] Cimino A, Porta P and Valigi M 1966 Dependence of lattice parameter of magnesium oxide on crystallite size *J. Am. Ceram. Soc.* **49** 152–6
- [145] Vermaak J S, Mays C W and Kuhlmann-Wilsdorf D 1968 On surface stress and surface tension: I. Theoretical considerations *Surf. Sci.* **12** 128–33
- [146] Mays C W, Vermaak J S and Kuhlmann D 1968 On surface stress and surface tension.2. Determination of surface stress of gold *Surf. Sci.* **12** 134–40
- [147] Wasserma H J and Vermaak J S 1970 On determination of a lattice contraction in very small silver particles *Surf. Sci.* **22** 164–72
- [148] Wasserman H J and Vermaak J S 1997 On the determination of the surface stress of copper and platinum *Surf. Sci.* **32** 168–74
- [149] Khanna S N, Bucher J P, Buttet J and Cyrotlackmann F 1983 Stability and lattice contraction of small platinum particles *Surf. Sci.* **127** 165–74
- [150] Solliard C and Flueli M 1985 Surface stress and size effect on the lattice-parameter in small particles of gold and platinum *Surf. Sci.* **156** 487–94
- [151] Borel J P and Chatelain A 1985 Surface stress and surface-tension—equilibrium and pressure in small particles *Surf. Sci.* **156** 572–9
- [152] Scamarcio G, Lugara M and Manno D 1992 Size-dependent lattice contraction in CdS_{1-x}Se_x nanocrystals embedded in glass observed by Raman scattering *Phys. Rev. B* **45** 13792–5
- [153] Cammarata R C and Sieradzki K 1994 Surface and interface stresses *Ann. Rev. Mater. Sci.* **24** 215–34
- [154] Lamber R, Wetjen S and Jaeger N I 1995 Size dependence of the lattice parameter of small palladium particles *Phys. Rev. B* **51** 10968–71
- [155] Reimann K and Wurschum R 1997 Distribution of internal strains in nanocrystalline Pd studied by x-ray diffraction *J. Appl. Phys.* **81** 7186–92
- [156] Jiang Q, Liang L H and Zhao D S 2001 Lattice contraction and surface stress of fcc nanocrystals *J. Phys. Chem. B* **105** 6275–7
- [157] Qi W H, Wang M P and Su Y C 2002 Size effect on the lattice parameters of nanoparticles *J. Mater. Sci. Lett.* **21** 877–8
- [158] Li G S, Boerio-Goates J, Woodfield B F and Li L P 2004 Evidence of linear lattice expansion and covalency enhancement in rutile TiO₂ nanocrystals *Appl. Phys. Lett.* **85** 2059–61
- [159] Qi W H and Wang M P 2005 Size and shape dependent lattice parameters of metallic nanoparticles *J. Nanopart. Res.* **7** 51–7
- [160] Shreiber D and Jesser W A 2006 Size dependence of lattice parameter for SixGe_{1-x} nanoparticles *Surf. Sci.* **600** 4584–90
- [161] Ahmad M I and Bhattacharya S S 2009 Size effect on the lattice parameters of nanocrystalline anatase *Appl. Phys. Lett.* **95** 191906
- [162] Diehm P M, Agoston P and Albe K 2012 Size-dependent lattice expansion in nanoparticles: reality or anomaly? *Chemphyschem* **13** 2443–54
- [163] Oehl N, Knipper M, Parisi J, Plaggenborg T and Kolny-Olesiak J 2015 Size-dependent lattice distortion in epsilon-Ag₃Sn alloy nanoparticles *J. Phys. Chem. C* **119** 14450–4
- [164] Pfeifer M A, Williams G J, Vartanyants I A, Harder R and Robinson I K 2006 3D mapping of a deformation field inside a nanocrystal *Nature* **442** 63–6
- [165] Harder R, Pfeifer M A, Williams G J, Vartanyants I A and Robinson I K 2007 Orientation variation of surface strain *Phys. Rev. B* **76** 115425
- [166] Huang W J, Sun R, Tao J, Menard L D, Nuzzo R G and Zuo J M 2008 Coordination-dependent surface atomic contraction in nanocrystals revealed by coherent diffraction *Nat. Mater.* **7** 308–13
- [167] Robinson I and Harder R 2009 Coherent x-ray diffraction imaging of strain at the nanoscale *Nat. Mater.* **8** 291–8
- [168] Favre-Nicolin V *et al* 2010 Analysis of strain and stacking faults in single nanowires using Bragg coherent diffraction imaging *New J. Phys.* **12** 035013
- [169] Newton M C, Leake S J, Harder R and Robinson I K 2010 3D imaging of strain in a single ZnO nanorod *Nat. Mater.* **9** 120–4
- [170] Beutier G *et al* 2013 Strain inhomogeneity in copper islands probed by coherent x-ray diffraction *Thin Solid Films* **530** 120–4
- [171] Harder R and Robinson I K 2013 Coherent x-ray diffraction imaging of morphology and strain in nanomaterials *JOM* **65** 1202–7
- [172] Robinson I 2013 Nanoparticle structure by coherent x-ray diffraction *J. Phys. Soc. Japan* **82** 021012
- [173] Kim J W, Manna S, Dietze S H, Ulvestad A, Harder R, Fohtung E, Fullerton E E and Shpyrko O G 2014 Curvature-induced and thermal strain in polyhedral gold nanocrystals *Appl. Phys. Lett.* **105** 173108
- [174] Spencer B J, Voorhees P W and Davis S H 1991 Morphological instability in epitaxially strained dislocation-free solid films *Phys. Rev. Lett.* **67** 3696–9
- [175] Spencer B J, Voorhees P W and Davis S H 1993 Morphological instability in epitaxially strained dislocation-free solid films—linear-stability theory *J. Appl. Phys.* **73** 4955–70
- [176] Tersoff J and Tromp R M 1993 Shape transition in growth of strained islands: Spontaneous formation of quantum wires *Phys. Rev. Lett.* **70** 2782–5
- [177] Guyer J E and Voorhees P W 1995 Morphological stability of alloy thin films *Phys. Rev. Lett.* **74** 4031–4
- [178] Spencer B J and Tersoff J 1997 Equilibrium shapes and properties of epitaxially strained islands *Phys. Rev. Lett.* **79** 4858–61
- [179] Medeiros-Ribeiro G, Bratkovski A M, Kamins T I, Ohlberg D A A and Williams R S 1998 Shape transition of

- germanium nanocrystals on a silicon (001) surface from pyramids to domes *Science* **279** 353–5
- [180] Daruka I, Tersoff J and Barabasi A L 1999 Shape transition in growth of strained islands *Phys. Rev. Lett.* **82** 2753–6
- [181] Shchukin V A and Bimberg D 1999 Spontaneous ordering of nanostructures on crystal surfaces *Rev. Mod. Phys.* **71** 1125–71
- [182] Spencer B J 1999 Asymptotic derivation of the glued-wetting-layer model and contact-angle condition for Stranski-Krastanow islands *Phys. Rev. B* **59** 2011–7
- [183] Li A, Liu F and Lagally M G 2000 Equilibrium shape of 2D islands under stress *Phys. Rev. Lett.* **85** 1922–5
- [184] Cristini V and Lowengrub J 2002 3D crystal growth—I: linear analysis and self-similar evolution *J. Cryst. Growth* **240** 267–76
- [185] Aqua J N, Berbezier I, Favre L, Frisch T and Ronda A 2013 Growth and self-organization of SiGe nanostructures *Phys. Rep.* **522** 59–189
- [186] Feng L, Wang J, Wang S B, Li L A, Shen M, Wang Z Y, Chen Z F and Zhao Y 2015 Understanding the effects of strain on morphological instabilities of a nanoscale island during heteroepitaxial growth *J. Appl. Phys.* **118** 035304
- [187] Muller P and Kern R 2000 Equilibrium shape of epitaxially strained crystals (Volmer-Weber case) *J. Cryst. Growth* **193** 257–70
- [188] Muller P and Kern R 2000 Equilibrium nano-shape changes induced by epitaxial stress (generalised Wulf-Kaisheff theorem) *Surf. Sci.* **457** 229–53
- [189] Lazzari R and Jupille J 2012 Growth kinetics and size-dependent wetting of Ag/alpha-Al(2)O(3)(0001) nanoparticles studied via the plasmonic response *Nanotechnology* **23** 135707
- [190] Sivaramakrishnan S, Wen J G, Scarpelli M E, Pierce B J and Zuo J M 2010 Equilibrium shapes and triple line energy of epitaxial gold nanocrystals supported on TiO₂(110) *Phys. Rev. B* **82** 195421
- [191] Bettge M, MacLaren S, Burdin S, Abraham D, Petrov I, Yu M F and Sammann E 2011 Importance of line and interfacial energies during VLS growth of finely stranded silica nanowires *J. Mater. Res.* **26** 2247–53
- [192] Cosandey F 2013 Epitaxy, interfacial energy and atomic structure of Au/TiO₂ interfaces *Phil. Mag.* **93** 1197–218
- [193] Gao W P, Choi A S and Zuo J M 2014 Interaction of nanometer-sized gold nanocrystals with rutile (110) surface steps revealed at atomic resolution *Surf. Sci.* **625** 16–22
- [194] Berg W F 1938 Crystal growth from solutions *Proc. R. Soc. London A* **164** 0079–95
- [195] Bircumshaw L L and Riddiford A C 1952 Transport control in heterogeneous reactions *Q. Rev.* **6** 157–85
- [196] Volmer M 1939 Kinetics of phase formation *Die Chemische Reaktion* ed K F Bonhoeffer (Ann Arbor, Michigan: Edwards Brothers, Inc.)
- [197] Burton W K, Cabrera N and Frank F C 1951 The growth of crystals and the equilibrium structure of their surfaces *Phil. Trans. R. Soc. London A* **243** 299–358
- [198] Kumar S, Gandhi K S and Kumar R 2007 Modeling of formation of gold nanoparticles by citrate method *Ind. Eng. Chem. Res.* **46** 3128–36
- [199] Rodriguez-Gonzalez B, Mulvaney P and Liz-Marzan L M 2007 An electrochemical model for gold colloid formation via citrate reduction *Z. Phys. Chem.* **221** 415–26
- [200] Soni V, Sindal R S and Mehrotra R N 2007 Kinetics and mechanism of the oxidation of oxalic acid by tetrachloroaurate(III) ion *Inorg. Chim. Acta* **360** 3141–8
- [201] Finney E E and Finke R G 2008 Nanocluster nucleation and growth kinetic and mechanistic studies: a review emphasizing transition-metal nanoclusters *J. Colloid Interface Sci.* **317** 351–74
- [202] Harada M and Katagiri E 2010 Mechanism of silver particle formation during photoreduction using *in situ* time-resolved SAXS analysis *Langmuir* **26** 17896–905
- [203] Polte J, Ahner T T, Delissen F, Sokolov S, Emmerling F, Thunemann A F and Kraehnert R 2010 Mechanism of gold nanoparticle formation in the classical citrate synthesis method derived from coupled *in situ* XANES and SAXS evaluation *J. Am. Chem. Soc.* **132** 1296–301
- [204] Polte J, Erler R, Thunemann A F, Sokolov S, Ahner T T, Rademann K, Emmerling F and Kraehnert R 2010 Nucleation and growth of gold nanoparticles studied via *in situ* small angle x-ray scattering at millisecond time resolution *ACS Nano* **4** 1076–82
- [205] Yao T *et al* 2010 Insights into initial kinetic nucleation of gold nanocrystals *J. Am. Chem. Soc.* **132** 7696–701
- [206] Harada M, Tamura N and Takenaka M 2011 Nucleation and growth of metal nanoparticles during photoreduction using *in situ* time-resolved SAXS analysis *J. Phys. Chem. C* **115** 14081–92
- [207] Hudgens J W, Pettibone J M, Senftle T P and Bratton R N 2011 Reaction mechanism governing formation of 1,3-bis(diphenylphosphino)propane-protected gold nanoclusters *Inorg. Chem.* **50** 10178–89
- [208] Harada M and Kamigaito Y 2012 Nucleation and aggregative growth process of platinum nanoparticles studied by *in situ* quick XAFS spectroscopy *Langmuir* **28** 2415–28
- [209] Ojea-Jimenez I and Campanera J M 2012 Molecular modeling of the reduction mechanism in the citrate mediated synthesis of gold nanoparticles *J. Phys. Chem. C* **116** 23682–91
- [210] Streszewski B, Jaworski W, Paclawski K, Csapo E, Dekany I and Fitzner K 2012 Gold nanoparticles formation in the aqueous system of gold(III) chloride complex ions and hydrazine sulfate-kinetic studies *Colloids Surf. A Physicochem. Eng. Asp.* **397** 63–72
- [211] Wojnicki M, Rudnik E, Luty-Blocho M, Paclawski K and Fitzner K 2012 Kinetic studies of gold(III) chloride complex reduction and solid phase precipitation in acidic aqueous system using dimethylamine borane as reducing agent *Hydrometallurgy* **127** 43–53
- [212] Wuihschick M *et al* 2013 Size-controlled synthesis of colloidal silver nanoparticles based on mechanistic understanding *Chem. Mater.* **25** 4679–89
- [213] Perala S R and Kumar S 2014 On the two-step mechanism for synthesis of transition-metal nanoparticles *Langmuir* **30** 12703–11
- [214] Wuihschick M, Birnbaum A, Witte S, Sztucki M, Vainio U, Pinna N, Rademann K, Emmerling F, Kraehnert R and Polte J 2015 Turkevich in new robes: key questions answered for the most common gold nanoparticle synthesis *ACS Nano* **9** 7052–71
- [215] Sun Y G, Mayers B, Herricks T and Xia Y N 2003 Polyol synthesis of uniform silver nanowires: A plausible growth mechanism and the supporting evidence *Nano Lett.* **3** 955–60
- [216] Hamilton D R and Seidensticker R G 1960 Propagation mechanism of germanium dendrites *J. Appl. Phys.* **31** 1165–8
- [217] Wagner R S 1960 On the growth of germanium dendrites *Acta Metall.* **8** 57–60
- [218] Marks L D and Howie A 1979 Multiply-twinned particles in silver catalysts *Nature* **282** 196–8
- [219] vandeWaal B W 1996 Cross-twinning model of fcc crystal growth *J. Cryst. Growth* **158** 153–65
- [220] Kirkland A I, Jefferson D A, Duff D G, Edwards P P, Gameson I, Johnson B F G and Smith D J 1993 Structural studies of trigonal lamellar particles of gold and silver *Proc. R. Soc. London A* **440** 589–609

- [221] Lofton C and Sigmund W 2005 Mechanisms controlling crystal habits of gold and silver colloids *Adv. Funct. Mater.* **15** 1197–208
- [222] Gamalski A D, Voorhees P W, Ducati C, Sharma R and Hofmann S 2014 Twin plane re-entrant mechanism for catalytic nanowire growth *Nano Lett.* **14** 1288–92
- [223] Cahn J W and Taylor J E 1984 A contribution to the theory of surface-energy minimizing shapes *Scr. Metall.* **18** 1117–20
- [224] Cahn J W and Carter W C 1996 Crystal shapes and phase equilibria: a common mathematical basis *Metall. Mater. Trans. A* **27** 1431–40
- [225] Sekerka R F 2005 Equilibrium and growth shapes of crystals: how do they differ and why should we care? *Cryst. Res. Technol.* **40** 291–306
- [226] Herring C 1951 Some theorems on the free energies of crystal surfaces *Phys. Rev.* **82** 87–93
- [227] Coriell S R and Sekerka R F 1976 Effect of anisotropy of surface-tension and interface kinetics on morphological stability *J. Cryst. Growth* **34** 157–63
- [228] Uehara T and Sekerka R F 2003 Phase field simulations of faceted growth for strong anisotropy of kinetic coefficient *J. Cryst. Growth* **254** 251–61
- [229] Villain J 1991 Nonequilibrium systems—the shape of crystals to come *Nature* **350** 273–4
- [230] Taylor J E, Cahn J W and Handwerker C A 1992 Geometric models of crystal growth *Acta Metall. Et Mater.* **40** 1443–74
- [231] Almgren F, Taylor J E and Wang L 1993 Curvature-driven flows—a variational approach *SIAM J. Control Optim.* **31** 387–437
- [232] Cahn J W and Taylor J E 1994 Overview No-113—Surface motion by surface-diffusion *Acta Metall. Et Mater.* **42** 1045–63
- [233] Carter W C, Roosen A R, Cahn J W and Taylor J E 1995 Shape evolution by surface-diffusion end surface attachment limited kinetics on completely faceted surfaces *Acta Metall. Et Mater.* **43** 4309–23
- [234] Ambrosio L and Sonner H M 1996 Level set approach to mean curvature flow in arbitrary codimension *J. Differ. Geom.* **43** 693–737
- [235] Du D, Srolovitz D J, Coltrin M E and Mitchell C C 2005 Systematic prediction of kinetically limited crystal growth morphologies *Phys. Rev. Lett.* **95** 155503
- [236] Sun Q, Yerino C D, Ko T S, Cho Y S, Lee I H, Han J and Coltrin M E 2008 Understanding nonpolar GaN growth through kinetic Wulff plots *J. Appl. Phys.* **104** 093523
- [237] Leung B, Sun Q, Yerino C D, Han J and Coltrin M E 2012 Using the kinetic Wulff plot to design and control nonpolar and semipolar GaN heteroepitaxy *Semicond. Sci. Technol.* **27** 024005
- [238] Sun Q, Yerino C D, Leung B, Han J and Coltrin M E 2011 Understanding and controlling heteroepitaxy with the kinetic Wulff plot: a case study with GaN *J. Appl. Phys.* **110** 053517
- [239] Buhler J and Prior Y 2000 Study of morphological behavior of single diamond crystals *J. Cryst. Growth* **209** 779–88
- [240] Ringe E, Van Duyn R P and Marks L D 2013 Kinetic and thermodynamic modified wulff constructions for twinned nanoparticles *J. Phys. Chem. C* **117** 15859–70
- [241] Xia X, Zeng J, McDearmon B, Zheng Y, Li Q and Xia Y 2011 Silver nanocrystals with concave surfaces and their optical and surface-enhanced Raman scattering properties *Angew. Chem. Int. Ed. Engl.* **50** 12542–6
- [242] Royne A and Dysthe D K 2012 Rim formation on crystal faces growing in confinement *J. Cryst. Growth* **346** 89–100
- [243] Kubica A and Rybka P 2015 Fine singularity analysis of solutions to the Laplace equation: Berg's effect *Math. Methods Appl. Sci.* **38** 1734–45
- [244] Jindal V and Shahedipour-Sandvik F 2009 Theoretical prediction of GaN nanostructure equilibrium and nonequilibrium shapes *J. Appl. Phys.* **106** 083115
- [245] Zhang L F, Wang L, Zhong S L, Huang Y X and Xu A W 2012 Facile synthesis of concave decahedra enclosed by high-index facets and truncated decahedra with a large size *Dalton Trans.* **41** 4948–54
- [246] Siegfried M J and Choi K S 2005 Directing the architecture of cuprous oxide crystals during electrochemical growth *Angew. Chem. Int. Ed. Engl.* **44** 3218–23
- [247] Miao W F, Liu H R, Zhang Z M and Chen J F 2008 Large-scale growth and shape evolution of micrometer-sized Cu₂O cubes with concave planes via gamma-irradiation *Solid State Sci.* **10** 1322–6
- [248] Cordeiro M A L, Weng W H, Stroppa D G, Kiely C J and Leite E R 2013 High resolution electron microscopy study of nanocubes and polyhedral nanocrystals of cerium(IV) oxide *Chem. Mater.* **25** 2028–34
- [249] Zhang L, Niu W, Zhao J, Zhu S, Yuan Y, Hua L and Xu G 2013 Pd@Au core-shell nanocrystals with concave cubic shapes: kinetically controlled synthesis and electrocatalytic properties *Faraday Dis.* **164** 175–88
- [250] Liu M, Leng M, Liu D, Chen F, Li C and Wang C 2014 Local supersaturation dictated branching and faceting of submicrometer PbS particles with cubic growth habit *Inorg. Chem.* **53** 11484–91
- [251] You H, Yang S, Ding B and Yang H 2013 Synthesis of colloidal metal and metal alloy nanoparticles for electrochemical energy applications *Chem. Soc. Rev.* **42** 2880–904
- [252] Shah A B, Sivapalan S T, DeVetter B M, Yang T K, Wen J G, Bhargava R, Murphy C J and Zuo J M 2013 High-index facets in gold nanocrystals elucidated by coherent electron diffraction *Nano Lett.* **13** 1840–6
- [253] Xu X *et al* 2014 Synthesis of Pt-Ni alloy nanocrystals with high-index facets and enhanced electrocatalytic properties *Angew. Chem.* **126** 12730–5
- [254] Peng L, Jiang L, Lapedes D and Marks L D 2015 In preparation
- [255] De Wit R 1972 Partial Disclinations *J. Phys. C: Solid State* **5** 529–34
- [256] Gryaznov V G, Kaprelov A M, Romanov A E and Polonskii I A 1991 Channels of relaxation of elastic stresses in pentagonal nanoparticles *Phys. Status Solidi B* **167** 441–50
- [257] Polonsky I A, Romanov A E, Gryaznov V G and Kaprelov A M 1991 Disclination in an Elastic Sphere *Phil. Mag. A* **64** 281–7
- [258] Romanov A E 2002 Fundamentals of Disclination Theory: Development of Disclination-Dislocation Structures in Deformed Materials *Solid State Phenom.* **87** 47–56
- [259] Romanov A E 2003 Mechanics and physics of disclinations in solids *Eur. J. Mech. A* **22** 727–41
- [260] Romanov A E and Kolesnikova A L 2009 Application of disclination concept to solid structures *Prog. Mater. Sci.* **54** 740–69
- [261] Kolesnikova A L and Romanov A E 2010 Representations of elastic fields of circular dislocation and disclination loops in terms of spherical harmonics and their application to various problems of the theory of defects *Int. J. Solids Struct.* **47** 58–70
- [262] Gutkin M Y 2011 Elastic and plastic deformation in nanocrystalline metals *Nanostructured Metals and Alloys: Processing, Microstructure, Mechanical Properties and Applications* ed S H Whang (Cambridge: Woodhead) pp 329–74
- [263] Romanov A E, Vikarchuk A A, Kolesnikova A L, Dorogin L M, Kink I and Aifantis E C 2012 Structural transformations in nano- and microobjects triggered by disclinations *J. Mater. Res.* **27** 545–51

- [264] Dorogin L M, Vlassov S, Kolesnikova A L, Kink I, Lohmus R and Romanov A E 2010 Crystal mismatched layers in pentagonal nanorods and nanoparticles *Phys. Status Solidi B* **247** 288–98
- [265] Dorogin L M, Vlassov S, Kolesnikova A L, Kink I, Lohmus R and Romanov A E 2010 Pentagonal nanorods and nanoparticles with mismatched shell layers *J. Nanosci. Nanotechnol.* **10** 6136–43
- [266] Johnson C L, Snoeck E, Ezcurdia M, Rodriguez-Gonzalez B, Pastoriza-Santos I, Liz-Marzan L M and Hytch M J 2008 Effects of elastic anisotropy on strain distributions in decahedral gold nanoparticles *Nat. Mater.* **7** 120–4
- [267] Patala S, Marks L D and de la Cruz M O 2013 Elastic strain energy effects in faceted decahedral nanoparticles *J. Phys. Chem. C* **117** 1485–94
- [268] Patala S, Marks L D and de la Cruz M O 2013 Thermodynamic analysis of multiply twinned particles: surface stress effects *J. Phys. Chem. Lett.* **4** 3089–94
- [269] Zhou Y and Fichtorn K A 2014 Internal stress-induced orthorhombic phase in 5-fold-twinned noble metal nanowires *J. Phys. Chem. C* **118** 18746–55
- [270] Takeguchi M, Tanaka M, Yasuda H and Furuya K 2001 Real-time high-resolution transmission electron microscopy observation of the growth process of () surfaces on a nanometer-sized Si multiply twinned particle *Surf. Sci.* **493** 414–9
- [271] Bagley B G 1965 A dense packing of hard spheres with 5-fold symmetry *Nature* **208** 674–5
- [272] Yang C Y, Yacamán M J and Heineman K 1979 Crystallography of decahedral and icosahedral particles *J. Cryst. Growth* **47** 283–90
- [273] Marks L D 1985 Inhomogeneous strains in small particles *Surf. Sci.* **150** 302–18
- [274] Marks L D and Smith D J 1983 Hrem and stem of defects in multiply-twinned particles *J. Microsc. Oxford* **130** 249–61
- [275] Ji W H, Qi W H, Li X, Zhao S L, Tang S S, Peng H C and Li S Q 2015 Investigation of disclinations in marks decahedral Pd nanoparticles by aberration-corrected HRTEM *Mater. Lett.* **152** 283–6
- [276] Pohl D, Wiesenhutter U, Mohn E, Schultz L and Rellinghaus B 2014 Near-surface strain in icosahedra of binary metallic alloys: segregational versus intrinsic effects *Nano Lett* **14** 1776–84
- [277] Walsh M J, Yoshida K, Kuwabara A, Pay M L, Gai P L and Boyes E D 2012 On the structural origin of the catalytic properties of inherently strained ultrasmall decahedral gold nanoparticles *Nano Lett.* **12** 2027–31
- [278] Niekietel F, Bitzek E and Spiecker E 2014 Combining atomistic simulation and x-ray diffraction for the characterization of nanostructures: a case study on fivefold twinned nanowires *ACS Nano* **8** 1629–38
- [279] Iijima S 1987 Fine particles of silicon.2. Decahedral multiply-twinned particles *Japan. J. Appl. Phys. I* **26** 365–72
- [280] Goris B *et al* 2015 Measuring lattice strain in three dimensions through electron microscopy *Nano Lett.* **15** 26340328
- [281] Hofmeister H 1991 Lattice-defects in decahedral multiply twinned particles of palladium *Z. Phys. D* **19** 307–10
- [282] Peng L X, Van Duyne R P and Marks L D 2015 Strain-induced segregation in bimetallic multiply twinned particles *J. Phys. Chem. Lett.* **6** 1930–4
- [283] Ferrando R 2015 Symmetry breaking and morphological instabilities in core-shell metallic nanoparticles *J. Phys.: Condens. Matter* **27** 013003
- [284] Boichichio D and Ferrando R 2013 Morphological instability of core-shell metallic nanoparticles *Phys. Rev. B* **87** 165435
- [285] Li Z-A, Spasova M, Ramasse Q M, Gruner M E, Kisielowski C and Farle M 2014 Chemically ordered decahedral FePt nanocrystals observed by electron microscopy *Phys. Rev. B* **89** 161406
- [286] Wang R M, Zhang H Z, Farle M and Kisielowski C 2009 Structural stability of icosahedral FePt nanoparticles *Nanoscale* **1** 276–9
- [287] Wang R, Dmitrieva O, Farle M, Dumpich G, Ye H, Poppa H, Kilaas R and Kisielowski C 2008 Layer resolved structural relaxation at the surface of magnetic FePt icosahedral nanoparticles *Phys. Rev. Lett.* **100** 017205
- [288] Gruner M E and Entel P 2012 Competition between ordering, twinning, and segregation in binary magnetic 3d–5d nanoparticles: a supercomputing perspective *Int. J. Quantum Chem.* **112** 277–88
- [289] Ajayan P M and Marks L D 1988 Quasimelting and phases of small particles *Phys. Rev. Lett.* **60** 585–7
- [290] Ajayan P M and Marks L D 1990 Phase instabilities in small particles *Phase Trans.* **24–6** 229–58
- [291] Berry R S and Smirnov B M 2013 Configurational transitions in processes involving metal clusters *Phys. Rep.* **527** 205–50
- [292] Cheng B and Ngan A H 2013 Thermally induced solid-solid structural transition of copper nanoparticles through direct geometrical conversion *J. Chem. Phys.* **138** 164314
- [293] Goloven'ko Z V, Gafner Y Y, Gafner S L and Redel L V 2013 Thermal stability of structure in small gold clusters *Phys. Metals Metallography* **114** 1038–44
- [294] Berry R S and Smirnov B M 2009 Phase transitions in various kinds of clusters *Phys.-Usp.* **52** 137–64
- [295] Cox G, Berry R S and Johnston R L 2006 Characterizing potential surface topographies through the distribution of saddles and minima *J. Phys. Chem. A* **110** 11543–50
- [296] Doye J P and Wales D J 2001 Polytetrahedral clusters *Phys. Rev. Lett.* **86** 5719–22
- [297] Wales D J, Doye J P K, Miller M A, Mortenson P N and Walsh T R 2000 Energy landscapes: from clusters to biomolecules *Advances in Chemical Physics* ed I Prigogine and S A Rice (New York: J Wiley & Sons) vol 115 pp 1–111
- [298] Doye J P K, Wales D J and Miller M A 1998 Thermodynamics and the global optimization of Lennard-Jones clusters *J. Chem. Phys.* **109** 8143–53
- [299] Ball K D, Berry R S, Kunz R E, Li F-Y, Proykova A and Wales D J 1996 From topographies to dynamics on multidimensional potential energy surfaces of atomic clusters *Science* **271** 963–6
- [300] Uppenbrink J and Wales D J 1992 Structure and energetics of model metal-clusters *J. Chem. Phys.* **96** 8520–34
- [301] Berry R S 1990 Clusters, melting, freezing and phase-transitions—introductory lecture *J. Chem. Soc. Faraday Trans.* **86** 2343–9
- [302] Berry R S, Jellinek J and Natanson G 1984 Melting of clusters and melting *Phys. Rev. A* **30** 919–31
- [303] Wells D M, Rossi G, Ferrando R and Palmer R E 2015 Metastability of the atomic structures of size-selected gold nanoparticles *Nanoscale* **7** 6498–503
- [304] Baletto F, Mottet C and Ferrando R 2000 Reentrant morphology transition in the growth of free silver nanoclusters *Phys. Rev. Lett.* **84** 5544–7
- [305] Koga K, Ikeshoji T and Sugawara K 2004 Size- and temperature-dependent structural transitions in gold nanoparticles *Phys. Rev. Lett.* **92** 115507
- [306] Chen Q, Tanaka M and Furuya K Unusual crystallographic structure and its fluctuation of indium nanoparticles as-deposited and observed with HRTEM using the UHV-DC-TEM system *Surf. Sci.* **440** 398–406
- [307] Iijima S and Ichihashi T 1986 Structural instability of ultrafine particles of metals *Phys. Rev. Lett.* **56** 616–9

- [308] Yagi K, Takayanagi K, Kobayashi K and Honjo G 1975 *In situ* observations of growth processes of multiply twinned particles *J. Cryst. Growth* **28** 117–24
- [309] Buffat P A 2003 Dynamical behaviour of nanocrystals in transmission electron microscopy: size, temperature or irradiation effects *Philos. Trans. A Math. Phys. Eng. Sci.* **361** 291–5
- [310] Du X W, Wang B, Zhao N Q and Furuya K 2005 Structure evolution of silicon nanocrystals under electron irradiation *Scr. Mater.* **53** 899–903
- [311] Silly F and Castell M R 2009 Temperature-dependent stability of supported five-fold twinned copper nanocrystals *ACS Nano* **3** 901–6
- [312] van Huis M A, Young N P, Pandraud G, Creemer J F, Vanmaekelbergh D, Kirkland A I and Zandbergen H W 2009 Atomic imaging of phase transitions and morphology transformations in nanocrystals *Adv. Mater.* **21** 4992–5
- [313] Young N P, van Huis M A, Zandbergen H W, Xu H and Kirkland A I 2010 Transformations of gold nanoparticles investigated using variable temperature high-resolution transmission electron microscopy *Ultramicroscopy* **110** 506–16
- [314] Wang Z W and Palmer R E 2012 Determination of the ground-state atomic structures of size-selected Au nanoclusters by electron-beam-induced transformation *Phys. Rev. Lett.* **108** 245502
- [315] Wei B Q, Vajtai R, Jung Y J, Banhart F, Ramanath G and Ajayan P M 2002 Massive icosahedral boron carbide crystals *J. Phys. Chem. B* **106** 5807–9
- [316] Gillet M 1977 Structure of small metallic particles *Surf. Sci.* **67** 139–57
- [317] Jadzinsky P D, Calero G, Ackerson C J, Bushnell D A and Kornberg R D 2007 Structure of a thiol monolayer-protected gold nanoparticle at 1.1 Å resolution *Science* **318** 430–3
- [318] Akola J, Walter M, Whetten R L, Hakkinen H and Gronbeck H 2008 On the structure of thiolate-protected Au₂₅ *J. Am. Chem. Soc.* **130** 3756–7
- [319] Heaven M W, Dass A, White P S, Holt K M and Murray R W 2008 Crystal structure of the gold nanoparticle [N(C₈H₁₇)₄][Au₂₅(SCH₂CH₂Ph)₁₈] *J. Am. Chem. Soc.* **130** 3754–5
- [320] Lopez-Acevedo O, Akola J, Whetten R L, Gronbeck H and Hakkinen H 2009 Structure and bonding in the ubiquitous icosahedral metallic gold cluster Au-144(SR)₍₆₀₎ *J. Phys. Chem. C* **113** 5035–8
- [321] Qian H, Eckenhoff W T, Zhu Y, Pintauer T and Jin R 2010 Total structure determination of thiolate-protected Au₃₈ nanoparticles *J. Am. Chem. Soc.* **132** 8280–1
- [322] Zeng C, Li T, Das A, Rosi N L and Jin R 2013 Chiral structure of thiolate-protected 28-gold-atom nanocluster determined by x-ray crystallography *J. Am. Chem. Soc.* **135** 10011–3
- [323] Crasto D, Barcaro G, Stener M, Sementa L, Fortunelli A and Dass A 2014 Au₂(4)(SAdm)₁(6) nanomolecules: x-ray crystal structure, theoretical analysis, adaptability of adamantane ligands to form Au₂(3)(SAdm)₁(6) and Au₂(5)(SAdm)₁(6), and its relation to Au₂(5)(SR)₁(8) *J. Am. Chem. Soc.* **136** 14933–40
- [324] Crasto D, Malola S, Brososky G, Dass A and Hakkinen H 2014 Single crystal XRD structure and theoretical analysis of the chiral Au₃₀(S-t-Bu)₁₈ cluster *J. Am. Chem. Soc.* **136** 5000–5
- [325] Das A, Liu C, Byun H Y, Nobusada K, Zhao S, Rosi N and Jin R 2015 Structure determination of [Au₁₈(SR)₁₄] *Angew. Chem. Int. Ed. Engl.* **54** 3140–4
- [326] Dass A, Theivendran S, Nimmala P R, Kumara C, Jupally V R, Fortunelli A, Sementa L, Barcaro G, Zuo X and Noll B C 2015 Au₁₃₃(SPh-tBu)₅₂ nanomolecules: x-ray crystallography, optical, electrochemical, and theoretical analysis *J. Am. Chem. Soc.* **137** 4610–3
- [327] Jin R 2015 Atomically precise metal nanoclusters: stable sizes and optical properties *Nanoscale* **7** 1549–65
- [328] Xu W W and Gao Y 2015 Unraveling the atomic structures of the Au-68(SR)₍₃₄₎ nanoparticles *J. Phys. Chem. C* **119** 14224–9
- [329] Reinhard D, Hall B D, Ugarte D and Monot R 1997 Size-independent fcc-to-icosahedral structural transition in unsupported silver clusters: an electron diffraction study of clusters produced by inert-gas aggregation *Phys. Rev. B* **55** 7868–81
- [330] Reinhard D, Hall B D, Berthoud P, Valkealahti S and Monot R 1998 Unsupported nanometer-sized copper clusters studied by electron diffraction and molecular dynamics *Phys. Rev. B* **58** 4917–26
- [331] Ajayan P M and Marks L D 1989 Experimental evidence for quasimelting in small particles *Phys. Rev. Lett.* **63** 279–82
- [332] Dai Z R, Sun S H and Wang Z L 2002 Shapes, multiple twins and surface structures of monodisperse FePt magnetic nanocrystals *Surf. Sci.* **505** 325–35
- [333] Koga K and Sugawara K 2003 Population statistics of gold nanoparticle morphologies: direct determination by HREM observations *Surf. Sci.* **529** 23–35
- [334] MacArthur K E, Young N P, Critchell J W and Kirkland A I 2011 ‘*Ex situ*’ annealing and structural transformations in gold nanoparticles *Electron Microscopy and Analysis Group Conf. 2011* vol **371**
- [335] Volk A, Thaler P, Koch M, Fisslthaler E, Grogger W and Ernst W E 2013 High resolution electron microscopy of Ag-clusters in crystalline and non-crystalline morphologies grown inside superfluid helium nanodroplets *J. Chem. Phys.* **138** 214312
- [336] Pohl D, Surrey A, Schultz L and Rellinghaus B 2012 The impact of oxygen on the morphology of gas-phase prepared Au nanoparticles *Appl. Phys. Lett.* **101** 263105
- [337] Hayashi T, Ohno T, Yatsuya S and Uyeda R 1997 Formation of ultrafine metal particles by gas-evaporation technique. 4. Crystal habits of iron and fcc metals, Al, Co, Ni, Cu, Pd, Ag, In, Au and Pb *Japan. J. Appl. Phys.* **16** 705–17
- [338] Enterkin J A, Poepplmeier K R and Marks L D 2011 Oriented catalytic platinum nanoparticles on high surface area strontium titanate nanocuboids *Nano Lett.* **11** 993–7
- [339] Ray N A, Van Duyne R P and Stair P C 2012 Synthesis strategy for protected metal nanoparticles *J. Phys. Chem. C* **116** 7748–56
- [340] Masango S S, Peng L X, Marks L D, Van Duyne R P and Stair P C 2014 Nucleation and growth of silver nanoparticles by AB and ABC-type atomic layer deposition *J. Phys. Chem. C* **118** 17655–61
- [341] Keranen J, Auroux A, Ek S and Niinisto L 2002 Preparation, characterization and activity testing of vanadia catalysts deposited onto silica and alumina supports by atomic layer deposition *Appl. Catal. A* **228** 213–25
- [342] Aaltonen T, Ritala M, Sajavaara T, Keinonen J and Leskela M 2003 Atomic layer deposition of platinum thin films *Chem. Mater.* **15** 1924–8
- [343] Knez M, Niesch K and Niinisto L 2007 Synthesis and surface engineering of complex nanostructures by atomic layer deposition *Adv. Mater.* **19** 3425–38
- [344] Christensen S T *et al* 2009 Controlled growth of platinum nanoparticles on strontium titanate nanocubes by atomic layer deposition *Small* **5** 750–7
- [345] Christensen S T, Feng H, Libera J L, Guo N, Miller J T, Stair P C and Elam J W 2010 Supported Ru-Pt bimetallic nanoparticle catalysts prepared by atomic layer deposition *Nano Lett.* **10** 3047–51
- [346] George S M 2010 Atomic layer deposition: an overview *Chem. Rev.* **110** 111–31

- [347] Cho S, Kim D-H, Lee B-S, Jung J, Yu W-R, Hong S-H and Lee S 2012 Ethanol sensors based on ZnO nanotubes with controllable wall thickness via atomic layer deposition, an O₂ plasma process and an annealing process *Sensors Actuators B* **162** 300–6
- [348] Erkens I, Blauw M, Verheijen M, Roozeboom F and Kessels W M M 2013 Room temperature sensing of O₂ and CO by atomic layer deposition prepared ZnO films coated with Pt nanoparticles *ECS Trans.* **58** 203–14
- [349] Miikkulainen V, Nilsen O, Laitinen M, Sajavaara T and Fjellvåg H 2013 Atomic layer deposition of Li_xTi_yO_z thin films *RSC Adv.* **3** 7537–42
- [350] Wender H, de Oliveira L F, Migowski P, Feil A F, Lissner E, Prechtl M H G, Teixeira S R and Dupont J 2010 Ionic liquid surface composition controls the size of gold nanoparticles prepared by sputtering deposition *J. Phys. Chem. C* **114** 11764–8
- [351] Pashley D W and Stowell M J 1963 Electron microscopy and diffraction of twinned structures in evaporated films of gold *Phil. Mag.* **8** 1605–32
- [352] Fukaya K, Ino S and Ogawa S 1978 Orientation and structure of palladium particles formed by evaporation on alkali-halide crystals *Trans. Japan Inst. Metals* **19** 445–53
- [353] Shah P and Gavrin A 2006 Synthesis of nanoparticles using high-pressure sputtering for magnetic domain imaging *J. Magn. Magn. Mater.* **301** 118–23
- [354] Penuelas J, Andreazza P, Andreazza-Vignolle C, Mottet C, De Santis M and Tolentino H C N 2009 Real-time icosahedral to fcc structure transition during CoPt nanoparticles formation *Eur. Phys. J. Spec. Top.* **167** 19–25
- [355] Smigelskas A D and Kirkendall E O 1974 Zinc diffusion in alpha-brass *Trans. Am. Inst. Min. Metall. Eng.* **171** 130–42
- [356] Yin Y, Rioux R M, Erdonmez C K, Hughes S, Somorjai G A and Alivisatos A P 2004 Formation of hollow nanocrystals through the nanoscale Kirkendall effect *Science* **304** 711–4
- [357] Lou X W, Wang Y, Yuan C L, Lee J Y and Archer L A 2006 Template-free synthesis of SnO₂ hollow nanostructures with high lithium storage capacity *Adv. Mater.* **18** 2325–9
- [358] Lou X W, Archer L A and Yang Z C 2008 Hollow micro-/nanostructures: synthesis and applications *Adv. Mater.* **20** 3987–4019
- [359] Watanabe Y, Mowbray R W, Rice K P and Stoykovich M P 2014 Kinetic description of metal nanocrystal oxidation: a combined theoretical and experimental approach for determining morphology and diffusion parameters in hollow nanoparticles by the nanoscale Kirkendall effect *Phil. Mag.* **94** 3487–506
- [360] Yang Z, Yang N and Pileni M-P 2015 Nano kirkendall effect related to nanocrystallinity of metal nanocrystals: influence of the outward and inward atomic diffusion on the final nanoparticle structure *J. Phys. Chem. C* **119** 22249–60
- [361] Xia X, Xie S, Liu M, Peng H C, Lu N, Wang J, Kim M J and Xia Y 2013 On the role of surface diffusion in determining the shape or morphology of noble-metal nanocrystals *Proc. Natl. Acad. Sci. USA* **110** 6669–73
- [362] Ostwald W 1900 On the assumed isomerism of red and yellow mercury oxide and the surface-tension of solid bodies *Z. Phys. Chem.* **34** 495–503
- [363] Greenwood G W 1956 The growth of dispersed precipitates in solutions *Acta Metall.* **4** 243–8
- [364] Voorhees P W 1985 The theory of ostwald ripening *J. Stat. Phys.* **38** 231–52
- [365] Voorhees P W 1992 Ostwald ripening of 2-phase mixtures *Ann. Rev. Mater. Sci.* **22** 197–215
- [366] Zinkeallmang M, Feldman L C and Grabow M H 1992 Clustering on surfaces *Surf. Sci. Rep.* **16** 377–463
- [367] Zhang Z and Lagally M G 1997 Atomistic processes in the early stages of thin-film growth *Science* **276** 377–83
- [368] Brune H 1998 Microscopic view of epitaxial metal growth: nucleation and aggregation *Surf. Sci. Rep.* **31** 121–229
- [369] Chan S W and Balluffi R W 1985 Study of energy versus misorientation for grain-boundaries in gold by crystallite rotation method.1. [00 1] twist boundaries *Acta Metall.* **33** 1113–9
- [370] Chan S W and Balluffi R W 1986 Study of energy versus misorientation for grain-boundaries in gold by crystallite rotation method.2. Tilt boundaries and mixed boundaries *Acta Metall.* **34** 2191–9
- [371] Bonevich J E and Marks L D 1992 The sintering behavior of ultrafine alumina particles *J. Mater. Res.* **7** 1489–500
- [372] Yeadon M, Ghaly M, Yang J C, Averbach R S and Gibson J M ‘Contact epitaxy’ observed in supported nanoparticles *Appl. Phys. Lett.* **73** 3208–10
- [373] Cahn J W and Taylor J E 2004 A unified approach to motion of grain boundaries, relative tangential translation along grain boundaries, and grain rotation *Acta Mater.* **52** 4887–98
- [374] Jose-Yacamán M, Gutierrez-Wing C, Miki M, Yang D Q, Piyakis K N and Sacher E 2005 Surface diffusion and coalescence of mobile metal nanoparticles *J Phys Chem B* **109** 9703–11
- [375] Niederberger M and Colfen H 2006 Oriented attachment and mesocrystals: non-classical crystallization mechanisms based on nanoparticle assembly *Phys. Chem. Chem. Phys.* **8** 3271–87
- [376] Theissmann R, Fendrich M, Zinetullin R, Guenther G, Schierning G and Wolf D E 2008 Crystallographic reorientation and nanoparticle coalescence *Phys. Rev. B* **78** 205413
- [377] Yin Z, Zhang Y, Chen K, Li J, Li W, Tang P, Zhao H, Zhu Q, Bao X and Ma D 2014 Monodispersed bimetallic PdAg nanoparticles with twinned structures: formation and enhancement for the methanol oxidation *Sci. Rep.* **4** 4288
- [378] Nichols F A 1966 Coalescence of 2 Spheres by surface diffusion *J. Appl. Phys.* **37** 2805–8
- [379] Rankin J and Sheldon B W 1995 *In situ* TEM sintering of nano-sized ZrO₂ particles *Mater. Sci. Eng. A Struct. Mater.* **204** 48–53
- [380] Shao Y Q, Tang D and Xiong W H 2007 *In situ* TEM study on microstructural evolution of nanostructured TiO₂ *J. Wuhan Univ. Technol. Mat. Sci. Ed.* **22** 209–13
- [381] Lim T H, McCarthy D, Hendy S C, Stevens K J, Brown S A and Tilley R D 2009 Real-time TEM and kinetic Monte Carlo studies of the coalescence of decahedral gold nanoparticles *ACS Nano* **3** 3809–13
- [382] Holland T B, Thron A M, Bonifacio C S, Mukherjee A K and van Benthem K 2010 Field assisted sintering of nickel nanoparticles during *in situ* transmission electron microscopy *Appl. Phys. Lett.* **96** 243106
- [383] Klinger L and Rabkin E 2010 Sintering of fully faceted crystalline particles *Int. J. Mater. Res.* **101** 75–83
- [384] Ingham B, Lim T H, Dotzler C J, Henning A, Toney M F and Tilley R D 2011 How nanoparticles coalesce: an *in situ* study of au nanoparticle aggregation and grain growth *Chem. Mater.* **23** 3312–7
- [385] Niu K Y, Liao H G and Zheng H 2014 Visualization of the coalescence of bismuth nanoparticles *Microsc. Microanal.* **20** 416–24
- [386] Combe N, Jensen P and Pimpinelli A 2000 Changing shapes in the nanoworld *Phys. Rev. Lett.* **85** 110–3
- [387] Combe N and Larralde H 2000 Low-temperature shape relaxation of 2D islands by edge diffusion *Phys. Rev. B* **62** 16074–84
- [388] Mullins W W and Rohrer G S 2000 Nucleation barrier for volume-conserving shape changes of faceted crystals *J. Am. Ceram. Soc.* **83** 214–6

- [389] Rohrer G S, Rohrer C L and Mullins W W 2002 Coarsening of faceted crystals *J. Am. Ceram. Soc.* **85** 675–82
- [390] Sheldon B W and Rankin J 2002 Step-energy barriers and particle shape changes during coarsening *J. Am. Ceram. Soc.* **85** 683–90
- [391] Hendy S, Brown S A and Hyslop M 2003 Coalescence of nanoscale metal clusters: Molecular-dynamics study *Phys. Rev. B* **68** 241403
- [392] Thurmer K, Reutt-Robey J E and Williams E D 2003 Nucleation limited crystal shape transformations *Surf. Sci.* **537** 123–33
- [393] Degawa M and Williams E D 2005 Barriers to shape evolution of supported nano-crystallites *Surf. Sci.* **595** 87–96
- [394] Degawa M, Thurmer K and Williams E D 2006 Constrained evolution of nanocrystallites *Phys. Rev. B* **74** 155432
- [395] Marks L and Voyles P 2014 When is Z-contrast D-contrast? *Microsc. Today* **22** 65
- [396] Perdew J P, Ruzsinszky A, Csonka G I, Vydrov O A, Scuseria G E, Constantin L A, Zhou X and Burke K 2008 Restoring the density-gradient expansion for exchange in solids and surfaces *Phys. Rev. Lett.* **100** 136406
- [397] Stroppa A and Kresse G 2008 The shortcomings of semi-local and hybrid functionals: what we can learn from surface science studies *New J. Phys.* **10** 063020
- [398] Zhao Y and Truhlar D G 2008 Exploring the limit of accuracy of the global hybrid meta density functional for main-group thermochemistry, kinetics, and noncovalent interactions *J. Chem. Theory Comput.* **4** 1849–68
- [399] Cramer C J and Truhlar D G 2009 Density functional theory for transition metals and transition metal chemistry *Phys. Chem. Chem. Phys.* **11** 10757–816
- [400] Haas P, Tran F and Blaha P 2009 Calculation of the lattice constant of solids with semilocal functionals *Phys. Rev. B* **79** 085104
- [401] Perdew J P, Ruzsinszky A, Csonka G I, Constantin L A and Sun J 2009 Workhorse semilocal density functional for condensed matter physics and quantum chemistry *Phys. Rev. Lett.* **103** 026403
- [402] Schimka L, Harl J, Stroppa A, Gruneis A, Marsman M, Mittendorfer F and Kresse G 2010 Accurate surface and adsorption energies from many-body perturbation theory *Nat. Mater.* **9** 741–4
- [403] Goerigk L and Grimme S 2011 A thorough benchmark of density functional methods for general main group thermochemistry, kinetics, and noncovalent interactions *Phys. Chem. Chem. Phys.* **13** 6670–88
- [404] Klimes J, Bowler D R and Michaelides A 2011 Van der Waals density functionals applied to solids *Phys. Rev. B* **83** 195131
- [405] Cohen A J, Mori-Sanchez P and Yang W 2012 Challenges for density functional theory *Chem. Rev.* **112** 289–320
- [406] Sun J W, Xiao B, Fang Y, Haunschild R, Hao P, Ruzsinszky A, Csonka G I, Scuseria G E and Perdew J P 2013 Density functionals that recognize covalent, metallic, and weak bonds *Phys. Rev. Lett.* **111** 106401
- [407] Becke A D 2014 Perspective: Fifty years of density-functional theory in chemical physics *J. Chem. Phys.* **140** 18A301
- [408] Perdew J P, Ruzsinszky A, Sun J and Burke K 2014 Gedanken densities and exact constraints in density functional theory *J. Chem. Phys.* **140** 18A533
- [409] Sun J, Ruzsinszky A and Perdew J P 2015 Strongly constrained and appropriately normed semilocal density functional *Phys. Rev. Lett.* **115** 036402
- [410] Johansson M P, Lechtken A, Schooss D, Kappes M M and Furche F 2008 2D–3D transition of gold cluster anions resolved *Phys. Rev. A* **77** 053202
- [411] Li Z Y, Young N P, Di Vece M, Palomba S, Palmer R E, Bleloch A L, Curley B C, Johnston R L, Jiang J and Yuan J 2008 3D atomic-scale structure of size-selected gold nanoclusters *Nature* **451** 46–U42
- [412] Goris B, Bals S, Van den Broek W, Carbo-Argibay E, Gomez-Grana S, Liz-Marzan L M and Van Tendeloo G 2012 Atomic-scale determination of surface facets in gold nanorods *Nat. Mater.* **11** 930–5
- [413] Bals S, Van Aert S and Van Tendeloo G 2013 High resolution electron tomography *Curr. Opin. Solid State Mater. Sc.* **17** 107–14
- [414] Goris B, De Backer A, Van Aert S, Gomez-Grana S, Liz-Marzan L M, Van Tendeloo G and Bals S 2013 3D elemental mapping at the atomic scale in bimetallic nanocrystals *Nano Lett.* **13** 4236–41
- [415] Van Aert S, De Backer A, Martinez G T, Goris B, Bals S, Van Tendeloo G and Rosenauer A 2013 Procedure to count atoms with trustworthy single-atom sensitivity *Phys. Rev. B* **87** 064107
- [416] Chen C-C, Zhu C, White E R, Chiu C-Y, Scott M C, Regan B C, Marks L D, Huang Y and Miao J 2013 3D imaging of dislocations in a nanoparticle at atomic resolution *Nature* **496** 74–7
- [417] Bals S, Goris B, Altantzis T, Heidari H, Van Aert S and Van Tendeloo G 2014 Seeing and measuring in 3D with electrons *C. R. Phys.* **15** 140–50
- [418] Bals S, Goris B, Liz-Marzan L M and Van Tendeloo G 2014 3D Characterization of noble-metal nanoparticles and their assemblies by electron tomography *Angew. Chem. Int. Ed.* **53** 10600–10
- [419] Zhu C, Chen C C, Du J C, Sawaya M R, Scott M C, Ercius P, Ciston J and Miao J W 2013 Towards 3D structural determination of amorphous materials at atomic resolution *Phys. Rev. B* **88** 100201
- [420] Zhang B and Su D S 2013 Electron tomography: 3D imaging of real crystal structures at atomic resolution *Angew. Chem. Int. Ed. Engl.* **52** 8504–6
- [421] Leary R, Saghi Z, Midgley P A and Holland D J 2013 Compressed sensing electron tomography *Ultramicroscopy* **131** 70–91
- [422] Goris B, Turner S, Bals S and Van Tendeloo G 2014 3D valency mapping in ceria nanocrystals *ACS Nano* **8** 10878–84
- [423] Midgley P A and Thomas J M 2014 Multi-dimensional electron microscopy *Angew. Chem. Int. Ed. Engl.* **53** 8614–7
- [424] Van den Broek W, Rosenauer A, Van Aert S, Sijbers J and Van Dyck D 2014 A memory efficient method for fully 3D object reconstruction with HAADF STEM *Ultramicroscopy* **141** 22–31
- [425] Willhammar T, Mayoral A and Zou X 2014 3D reconstruction of atomic structures from high angle annular dark field (HAADF) STEM images and its application on zeolite silicalite-1 *Dalton Trans.* **43** 14158–63
- [426] Xu R *et al* 2015 3D coordinates of individual atoms in materials revealed by electron tomography *Nat. Mater.* **14** 1099–103
- [427] Marks L D 1983 Direct imaging of carbon-covered and clean gold (1 1 0) surfaces *Phys. Rev. Lett.* **51** 1000–2
- [428] Marks L D and Smith D J 1983 Direct surface imaging in small metal particles *Nature* **303** 316–7
- [429] Marks L D 1984 High-resolution surface imaging *Acta Crystallogr. A* **40** C390
- [430] Marks L D 1984 Direct atomic imaging of solid-surfaces. 1. Image simulation and interpretation *Surf. Sci.* **139** 281–98
- [431] Marks L D, Heine V and Smith D J 1984 Direct observation of elastic and plastic-deformations at Au(1 1 1) surfaces *Phys. Rev. Lett.* **52** 656–8
- [432] Marks L D and Smith D J 1984 Direct atomic imaging of solid-surfaces.2. Gold (1 1 1) surfaces during and after *in situ* carbon etching *Surf. Sci.* **143** 495–508